GEOLOGICA ULTRAIECTINA

Mededelingen van de
Faculteit Aardwetenschappen der
Rijksuniversiteit te Utrecht

No. 88

S-WAVE VELOCITY BELOW EUROPE FROM DELAY-TIME AND WAVEFORM INVERSIONS

ALET ZIELHUIS

GEOLOGICA ULTRAIECTINA

Mededelingen van de
Faculteit Aardwetenschappen der
Rijksuniversiteit te Utrecht

No. 88

S-WAVE VELOCITY BELOW EUROPE FROM DELAY-TIME AND WAVEFORM INVERSIONS

CIP-DATA, KONINKLIJKE BIBLIOTHEEK, DEN HAAG

Zielhuis, Aletta.
S-wave velocity below Europe from delay-time and waveform inversions/ Aletta Zielhuis - [Utrecht : Faculteit Aardwetenschappen der Rijksuniversiteit Utrecht]. -
(Geologica Ultraiectina . ISSN 0072-1026 ; no. 88)
Thesis Rijksuniversiteit Utrecht. - With ref. -
With summary in Dutch.
ISBN: 90-71577-41-4
Subject headings: S-wave velocity

S-WAVE VELOCITY BELOW EUROPE

FROM

DELAY-TIME AND WAVEFORM INVERSIONS

VOORTPLANTINGSSNELHEID VAN S-GOLVEN ONDER EUROPA

BEPAALD DOOR

INVERSIE VAN LOOPTIJDGEGEVENS EN GOLFVORMEN

(met een samenvatting in het Nederlands)

PROEFSCHRIFT

TER VERKRIJGING VAN DE GRAAD VAN DOCTOR AAN DE
RIJKSUNIVERSITEIT TE UTRECHT OP GEZAG VAN DE
RECTOR MAGNIFICUS PROF. DR. J.A. VAN GINKEL
INGEVOLGE HET BESLUIT VAN HET COLLEGE VAN DEKANEN
IN HET OPENBAAR TE VERDEDIGEN OP MAANDAG
1 JUNI 1992 DES NAMIDDAGS TE 12.45 UUR

DOOR

ALETTA ZIELHUIS

GEBOREN OP 27 JULI 1960, TE HEERDE

PROMOTOR: PROF. DR A.M.H. NOLET

The research described in this thesis was carried out at the:

Department of Theoretical Geophysics,
Institute of Earth Sciences,
University of Utrecht,
Budapestlaan 4, P.O. Box 80.021,
3508 TA Utrecht,
The Netherlands.

Voor mijn ouders

Contents

Chapter 4

3-D structure from Rayleigh-wave phase velocity data

Chapter 5

Partitioned waveform inversion: theory

Chapter 6

Partitioned waveform inversion: the non-linear waveform inversion

Chapter 7

Partitioned waveform inversion: Results for Europe

Chapter 8

Discussion and comparison with results of other geophysical investigations

Chapter 1

Introduction and summary

1.1 Introduction and scientific objectives

The upper mantle of Europe has been the subject of many tomographic studies of variations in P-wave velocity (e.g., Romanowicz 1980; Hovland et al., 1981; Spakman, 1988, 1991; and Spakman et al., in preparation). In particular the studies of Spakman (1988, 1991) and Spakman et al. (in preparation) provided detailed images of the upper mantle. However, these images leave us with questions as to how reliable they are, or, more specifically, in which regions they are reliable. Moreover, they do not provide sufficient information to determine the causes of the velocity heterogeneities. Our knowledge about the variations in composition and temperature in the upper mantle is limited. The availability of accurate measurements of both the P- and S-wave velocity would enable us to answer the question whether the velocity variations are caused by temperature variations, differences in composition, or both (Yan et al., 1989; Furlong et al., 1992).

As mentioned above, high-resolution P-wave models are available from seismic tomography, although the amplitudes of the velocity variations are not well determined. Several authors have studied the S wave velocity in the upper 200 km of the mantle with phase velocity measurements of surface waves (e.g., Berry and Knopoff, 1967; Panza et al., 1980; Souriau, 1981; Mariller and Mueller, 1985). Snieder (1988) inverted waveforms of fundamental mode Rayleigh waves for a three-dimensional (3-D) model of the S velocity in the upper 200km of the mantle. From modelling broadband waveforms of S body waves

Paulssen (1987) determined a set of 1-D velocity models to 670 km depth for different paths crossing central and western Europe. However, these studies provided only limited information about the variations of the S wave velocity in the upper mantle on the length scale of anomalies in the 3-D P-wave velocity models. Therefore, the objective of the research described in this thesis is to find a model for variations in S wave velocity in which structure is resolved on length scales comparable to those in the 3-D P-wave velocity models. We discuss three different methods: body wave tomography with S-wave travel-time residuals published by the International Seismological Centre (ISC) (chapters 2 and 3); the inversion of phase velocities of surface waves (chapter 4); and the method of partitioned inversion (Nolet, 1990) of waveforms of both body- and surface waves (chapters 5,6, and 7).

We applied the method of delay time tomography (Aki et al., 1977; Nolet, 1985; Spakman and Nolet, 1988) because it was readily available and has proved to be successful in producing high-resolution images of variations in P wave velocity. With regard to the derivation of a S velocity model there are specific problems, such as larger errors in the data. A general shortcoming of the method of delay time tomography is that only structures in regions with a high density of stations and earthquakes can be resolved well. Compared to other geographical regions, Europe has a high density of stations. In contrast, earthquakes in Europe are unevenly distributed, and very few earthquakes occur outside of the African-Eurasian-Arabian collision zone in southern Europe. This particular distribution of sources and stations limits the resolution in the images of tomography obtained with (direct) body waves in western, northern and eastern Europe. Consequently, P-wave velocity models have contributed significantly to a better understanding of the Neogene tectonics of the seismically active regions in southern Europe, but not much to the understanding of the accretion history of the (now stable) intraplate regions of western and central Europe. The European Geotraverse (EGT) project has resulted in relevant information about the crust in these regions, but has provided little insight in deeper structures.

From the Dutch contribution to the EGT project, the Network of Autonomously Recording Seismometers (NARS), we know that surface waves can resolve lateral variations in lithospheric structure below stable intraplate regions (Snieder, 1988). Surface waves give information about the S wave velocity, which is of interest because of the reasons mentioned above. We inverted the available phase velocity data of fundamental mode Rayleigh waves. However, the regional sampling of the available data is limited, and these data are practically insensitive to structures below 200 km depth. With long-period surface wave data deeper structures in the upper mantle in stable intraplate regions can be resolved. The fast growing number of digitally recording stations has resulted in several studies in which these data are used for 3-D imaging of the Earth's interior. Due to the efforts of organizations such as the NEIC (National Earthquake Information Center), ORFEUS (Observatories and Research Facilities for European Seismology), and IRIS (Incorporation of Research Institutes for Seismology) digital data are now easy to obtain

(on CD-ROM, magnetic tapes, or by electronic mail) and to manipulate so that a large number of digital records can be used in a single study. Several 3-D S-wave velocity models on regional or global scale have been obtained using group or phase velocities or full waveforms of long-period surface waves (e.g., Woodhouse and Dziewonski, 1984; Nataf et al., 1986; Montagner, 1986; Zhang and Tanimoto, 1992). The major disadvantage of those methods with regard to the objective of our study is that the lateral resolution in these models is substantially less than obtained in the most successful applications of body wave tomography.

By inversion of waveforms of both body waves and surface waves many of the above mentioned shortcomings can be overcome. With the method of Partitioned Waveform Inversion (PWI; Nolet, 1990) it is possible to invert a large set of waveform data of body and surface waves for a 2-D or 3-D S-velocity model. Nolet (1990) used the method to obtain a 2-D velocity model of upper mantle below the NARS array in western Europe. By 1990 there were enough digital data available to apply the method to obtain a 3-D S velocity model for the upper mantle below Europe. The description of the application and the results of the PWI forms the main part of this thesis.

1.2 Outline and summary of thesis

The first part of this thesis focusses on the inversion of S delays reported by the ISC for a 3-D S wave velocity model of the upper mantle below Europe. In chapter 2, a 1-D reference model for the subsequent 3-D inversion was derived from the average value of S delays as a function of epicentral distance for Europe. The errors in the ISC S delays are large: the standard deviation of errors due to inaccurate readings, misidentifications, and, to a certain extent hypocenter mislocations, are estimated to be about 5 s for epicentral distances smaller than 28° and about 3 s at larger distances. Comparison of delay times for different tectonic regions in Europe demonstrates, however, that there is structural signal in this data set. In chapter 3, we applied the method of delay time tomography as developed by Spakman and Nolet (1988). The preferred model was obtained by inversion of travel time residuals with a maximum absolute value of 6 s. We used this rather low acceptance level because inclusion of delays with a larger absolute value resulted in models in which the average value of the velocity anomalies deviates systematically from zero over certain depth ranges. This might indicate that a linearized inversion with a 1-D reference model is not justified for these delay time data. Linearization about a 1-D reference model brings about that we cannot use all valid data. To include, for instance, delays that are associated to rays that arrive at epicentral distances between 13° and 20° and that bottom within the high velocity lid of the Baltic Shield, a laterally heterogeneous reference model is needed. In view of the large data errors, which can contaminate the solution and possible inaccuracies caused by linearization of the inversion problem with a 1-D reference model we were not satisfied with the result.

In chapter 4 we inverted the available phase velocity measurements of fundamental mode Rayleigh waves. The model resulting from this inversion has a strong low velocity

anomaly between Corsica and central Italy, between 0 and 55 km depth. Between 90 and 200km depth there is a low velocity anomaly below the Rhine graben and the Rhone Valley.

The main part of this thesis deals with the derivation of a 3-D S-wave velocity model with the method of Partitioned Waveform Inversion. The basic assumption underlying the method, as applied in this thesis, is that waveforms are only influenced by the properties of the Earth in the vertical plane through the source and receiver minor arc. Thus, effects of out-of-plane propagation are ignored. Under this assumption waveforms are inverted in two steps. In the first step, the time window of a seismogram containing the S wave up to the fundamental mode of the Rayleigh wave is inverted for a 1-D average velocity model for the path between source and receiver. This is a non-linear inversion and it results in linear constraints on the 1-D average model. This step is repeated for many criss-crossing wave paths. In the second step, the linear constraints are inverted for a 3-D model of the S velocity. This is the first application of the method PWI to obtain a 3-D velocity model. Important questions with regard to the method are for which frequencies observed waveforms can be fitted with the derived 3-D model, and what resolution can be obtained. In chapter 5 the theory of the method is summarized. In chapter 6 the application of the first step of this method is described: the non-linear inversion of waveforms for a 1-D average velocity model for the path between source and receiver. We show examples of fits and indicate how we tried to ensure, in practice, the validity of essential assumptions concerning the starting model for the non-linear inversion and the accuracy of the focal parameters. For many wave paths we were able to fit to body waves for frequencies as high as 60mHz with a 1-D model. The fundamental mode was low passed at 25mHz in order to avoid that effects of scattering of seismic waves contaminate the linear constraints. In total we inverted 217 seismograms, assembled from the NARS array, the long-period GDSN stations in Europe, the UKNET- and IRIS networks. This resulted in 920 linear constraints on the S wave velocity. In the second step, discussed in chapter 7, these linear constraints are combined in a linear inversion for a 3-D model.

In general, the waveforms predicted by the 3-D model - also S body-waves for frequencies as high as 60 mHz - match the observations well. In the region where the density of wave paths is highest, below Greece, the lateral resolution approximates the resolution that is obtained with P delay-time tomography. This indicates that the PWI has the potential to yield high resolution images, provided that enough data are available. For future applications of the method it should be investigated if the effect of varying crustal thickness on the retrieved velocity perturbations has to be incorporated in the non-linear inversion procedure.

The most spectacular feature in the result is a sharp lateral transition from low velocities below western and central Europe to high velocities below the Baltic Shield and Russian Platform. The transition is located below the Tornquist-Teisseyre Zone (TTZ) and exists to a depth of at least 140 km. Although there are many agreements between the model resulting from the waveform inversion and the model resulting from the inversion of

ISC S delays, there are also discrepancies, even for regions where sensitivity tests indicate that the resolution is good. Some of the discrepancies can be explained by a lack of vertical resolution in both data sets or by the fact that the inversion of ISC S delays is linearized with respect to a 1-D reference model, which can result in mapping of anomalies at wrong depths. Other differences, for example the absence of a velocity contrast below the TTZ in the result of the delay time inversion, are probably caused by a contamination of the latter result by errors in the data.

In chapter 8 we discuss in more detail the results of the PWI near the TTZ and below southeastern Europe. We selected the first region because the PWI provides new information about the mantle structure below this tectonic lineament, which is located in a stable intraplate region. The latter because this is the region with the highest resolution. The velocity contrast imaged across the TTZ is largest between the Pannonian Basin and the Russian Platform and may be about 12% and 9% at 80 km and 140 km depth, respectively. The lowest velocity contrast is observed between southern Sweden and Denmark/northern Germany where it is approximately 5% and 4.5% at 80 and 140 km depth, respectively. Assuming the reference values of Yan et al. (1989) for V_s and T at 150 km depth (4.506 km/s and 1300 °, respectively) the high velocity below the Russian Platform can be interpreted in terms of a thermal anomaly of a few hundred degrees. This would be consistent with the temperature to be expected at 150 km depth on the basis of the geotherm for a region with surface heat flow of 40 mW/m^2 at 150 km depth, which is a typical value for the Russian Platform. However, a compositional difference, or a combination of both, is also possible. Partial melting is a probable cause for the low velocities below the Carpathians and the northern Aegean Sea/Western Turkey. In southeastern Europe, the S wave velocity variations of our model correlate well with the P wave velocity model of Spakman et al. (in preparation) with respect to the sign of the anomalies, but the amplitudes of the S velocity anomalies are larger.

Chapter 2

Preliminary analysis of ISC S delays: general trends

2.1 Introduction

For several years geophysicists have applied tomographic techniques to image velocity structures on global or regional scale or very detailed structures in exploration seismics. In studies of large areas they often made use of the delay time data provided by the International Seismological Centre. Many results have been obtained using P delays. For instance, Spakman (1986) used 500,000 ISC P delays to derive a tomographic model of the upper mantle structures beneath the Mediterranean where the African and Eurasian plates converge. Less effort has been paid to tomographic imaging of shear velocity structures using ISC S delays. A tomographic S velocity model in addition to a P model could be of great importance for the interpretation of P anomalies in terms of mineral or temperature

This chapter has been composed of the papers:
Zielhuis, A., A shear velocity model for Europe from ISC delay times, Proceedings of the 4th workshop on the European Geotraverse project, pp. 57-62, European Science Foundation, Strasbourg, 1988.
and
Zielhuis, A., Spakman, W. and G. Nolet, A reference model for tomographic imaging of the shear velocity structure beneath Europe, in: Digital seismology and fine modelling of the lithosphere, Cassinis, R. Panza, G. and G. Nolet (Eds), Plenum Press, London, 333-340, 1989.

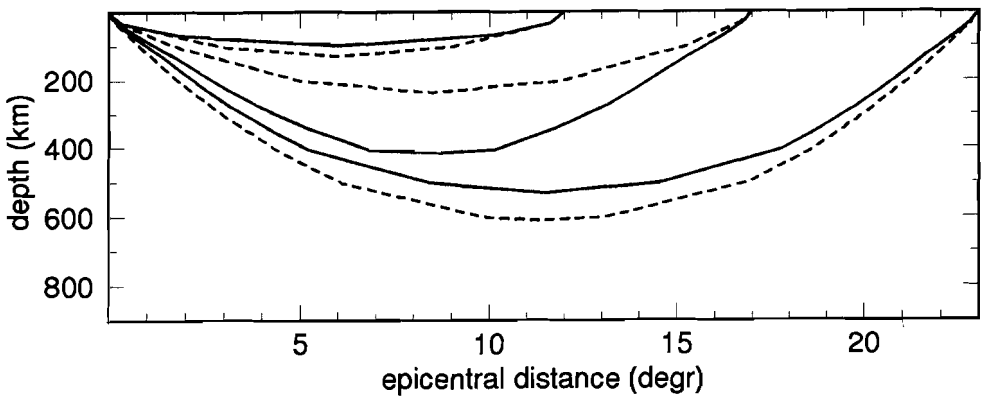

Figure 2.1. Ray paths calculated for the J-B model and a more realistic upper mantle model.

causes. With the use of S delays instead of P delays some extra problems are to be expected. Fewer S data are available from the ISC and S delays are subject to larger errors due to identification problems and inaccuracies in the readings of the exact onsets. The choice of the starting or reference model to be used for tomographic inversions should be considered carefully. An important approximation in delay time tomography is that the delay time of a certain arrival, i.e. the difference between observed travel time and travel time according to a theoretical reference model, is due to velocity anomalies located on the ray path in the reference model. This assumption is based on Fermat's principle that states that a wave follows a ray path that is stationary with respect to travel time, so that a small perturbation of the ray path has only a second order effect on the travel time. Systematic differences in the velocity structures of the true Earth and the reference model may cause large differences in ray geometry. In those cases the linear approximation is not justified. Moreover, even small differences in ray geometry may have unwanted effects on the solution if the inverse problem is ill-posed (Nolet, 1987a).

ISC delays are delay times relative to Jeffreys-Bullen travel times. Therefore, the use of uncorrected ISC delays implies that the Jeffreys-Bullen model is the reference model. The Jeffreys-Bullen model is a very smooth model without a Low Velocity Zone (LVZ) or discontinuities in the upper mantle. Currently several regional models are available that give a better description of the local velocity structure of the upper mantle. Most of these models show a LVZ between 100 and 200 km and a "400 km" and a "670 km" discontinuity. Since these features are absent in the Jeffreys-Bullen model it is doubtful if this model is adequate as a reference model for tomography. Figure 2.1 illustrates the problem. Three ray paths are calculated for the Jeffreys-Bullen model and a more realistic model with a LVZ and a 400 km discontinuity. Figure 2.1 shows that at some points the distance between rays in the two models arriving at 12° is about 50 km. For rays arriving at

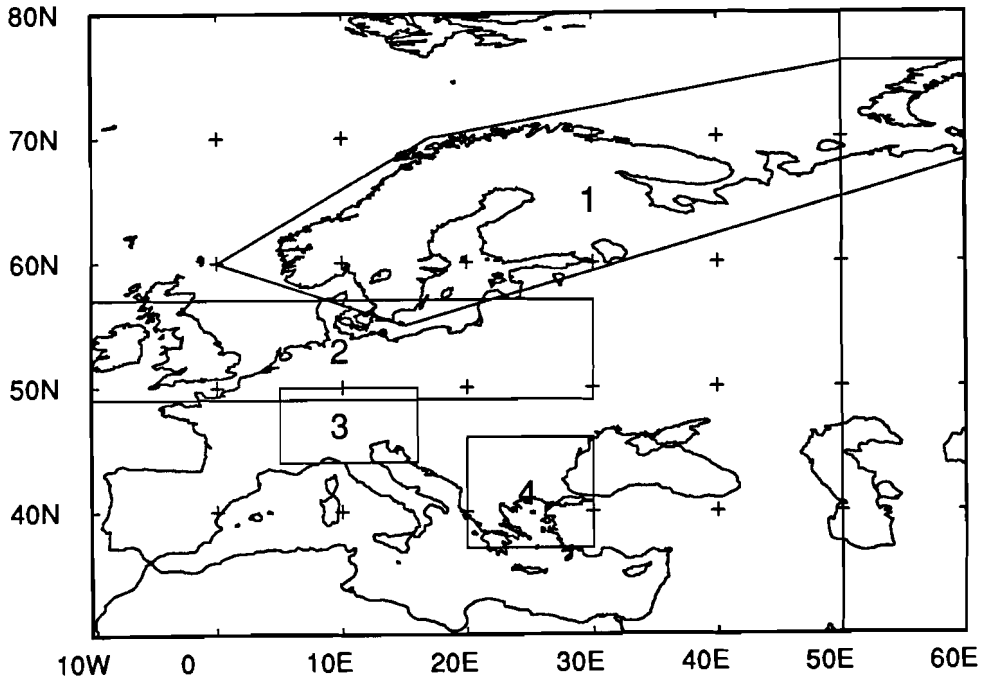

Figure 2.2. Map of the regions under study. The regions marked with numbers are discussed at the end of this chapter.

17° and 23° the difference in depth of the turning point is 200 km and 120 km, respectively. These distances are too large compared to the expected resolution. Spakman (1986) for instance used cells of 1° × 1°, with thickness varying from 33 km in the upper layers to 130 km at 600 km depth.

This study focuses on the question whether the Jeffreys-Bullen shear velocity model is appropriate as a reference model for tomographic imaging of the lithosphere and upper mantle beneath Europe. The study region extends from 10W to 50E and 30N to 80N (see figure 2.2). It is also investigated if there is structural signal in the S delays reported by the ISC.

2.2 Analysis of ISC S delays

S delays were read from ISC magnetic tapes containing all recordings of events that occurred in the period 1972 - 1982. Only arrivals were selected of which the turning point of the ray path is located under the study region. Figure 2.3 shows the relation between the 83,000 selected delay times and epicentral distance. If the average velocity structure beneath Europe would be similar to the J-B model, delays would be distributed around the line of zero delay. Obviously, this is not the case, since from 5° to 27° delays deviate

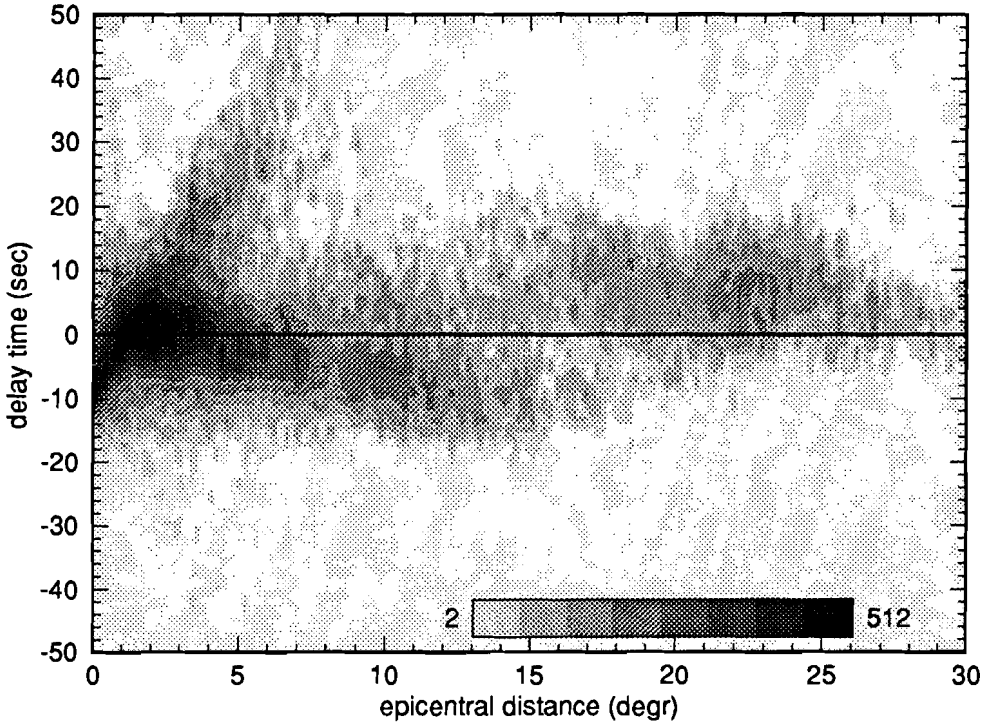

Figure 2.3. ISC S delays against epicentral distance. The number of delays per square area of 0.2° x 2 s is contoured with intervals shown in the legend.

significantly from 0. Moreover, different branches can be distinguished in the diagram. There is a clear branch between 0° and 15° with delays around 0 s at short distances, turning negative with increasing distance to an average of approximately -10 s at 15°. From 15° to 30° delays are mainly positive. Histograms of delay times at three different intervals, shown in figure 2.4, indicate the gradual transition from negative to positive delays. Between 8° and 10° the histogram shows a peak around -6 s, between 15° and 17° the negative and positive branch are both important, between 19° and 21° the maximum is at 7 s and the negative branch has disappeared. Waves arriving at short epicentral distances (< 13 °) have negative delays, which indicates that they travelled through Earth structure with higher velocity than predicted by the J-B model. Positive delays at greater distances indicate that the "time gain" is lost at greater depth. This can be explained by the presence of a low velocity layer. Thus, the negative delays at short epicentral distances belong to waves that bottomed within the high velocity lid and the more positive delays at larger distances belong to waves that bottomed below the LVZ. There is, however, no clear gap in the registrations. This is surprising since ray theory predicts a shadow zone in the travel time curve if a low velocity layer is present in the Earth. This subject is addressed in the

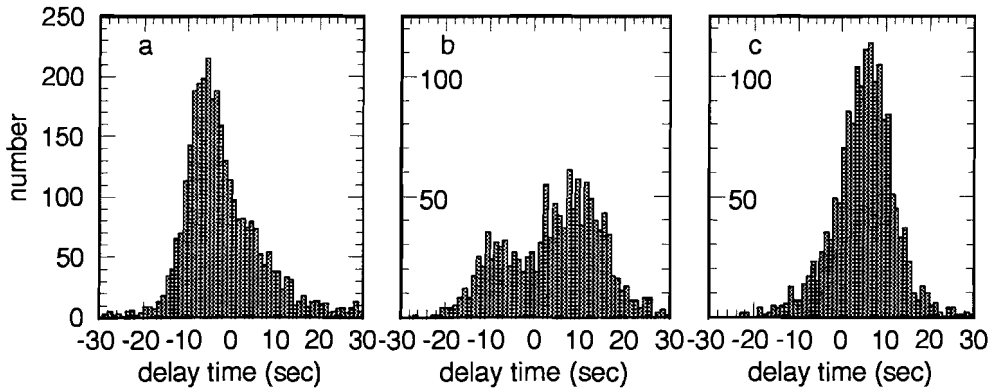

Figure 2.4. Histograms of delay times at three different intervals: 8°-10° (a), 15°-17° (b) and 19°-21° (c).

last section, where we analyse the ISC S delays for smaller regions within Europe.

A third branch is present between 0° and 7° with values of delays ranging from -10 s to 30 s. A large number of arrivals belonging to this branch are S_g waves but spurious arrivals like $S_M S$ may have been misinterpreted as first arrivals and thus appear in this branch.

The delay density plot indicates there is a significant systematic deviation of observed travel times from J-B travel times. This means that the J-B model differs significantly from the average shear velocity structure beneath Europe and, consequently, the J-B model is inadequate as the reference model for tomographic imaging of this area. In the following a reference model is derived that makes the systematic deviation of observed from theoretical (=reference model) travel times as small as possible. First a delay time curve is derived from the ISC data shown in figure 2.3. J-B travel times are added to this curve and the resulting travel times are inverted into a new S velocity model for Europe.

2.3 The travel time curve

Derivation of a delay time curve representative for the average velocity structure beneath Europe from the delay time data shown in figure 2.3 was not a straightforward procedure. As figure 2.3 and the histograms in figure 2.4 indicate different branches overlap and the data set is contaminated by a considerable amount of large residuals. Moreover, it is not clear what the extent of the shadow zone corresponding to the average velocity structure should be. Fitting one curve to the total data set would never result in a proper separation of the negative and positive branch. In order to estimate the location of the two branches, histograms of delays were made for every degree epicentral distance, each smoothed over two degrees (so the histogram for 10° contains all data at the interval 9°-11°). For most intervals the histogram resembles a superposition of two Gaussian-like distributions with different "amplitude". Therefore, first a distribution consisting of two

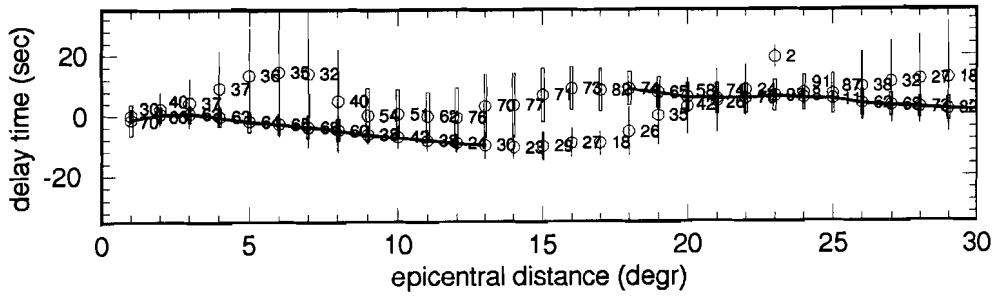

Figure 2.5. Parameters of the Gaussian distributions. Circles represent the means, the bars the corresponding standard deviations. An open bar indicates that most data belong to this distribution. The percentage of data belonging to each distribution is placed next to the symbols.

Gaussian distributions was fit to the histograms. A χ^2–test was performed to see if such a distribution is an adequate description. It turned out that for the histograms of 9°, 10°, 23°, 24° and 25° a distribution consisting of two Gaussian and one uniform distribution is a better description, because these histograms contain many large residuals, and they have heavier tails than predicted by Gaussian distributions. Figure 2.5 shows the parameters of the distributions. The location of the negative and positive branches is determined by the maxima of two Gaussian distributions. The percentage of data belonging to each of the two distributions indicates the relative importance of the branches.

The extent of the shadow zone was estimated in a subjective way. Around the negative and the positive branches as they appear in figure 2.3 two bands with a width of 14 s were drawn. Figure 2.6 displays the number of arrivals within each band as a function of epicentral distance. The curve corresponding to the positive branch shows that between 5° and 16° the number of arrivals within the band is low and approximately constant, from 16° to 18° it increases to a higher level, indicating that the positive branch becomes dominant. The gradual increase demonstrates that, due to lateral heterogeneity in the LVZ, the upper boundary of the shadow zone varies mainly between 16° and 18°. On the basis of the same argument, the lower boundary varies between 11° and 16°. The respective boundaries of the shadow zone associated with the average velocity structure should be well within these extremes.

Figure 2.5 shows the final delay time curve. To convert this curve into a travel time curve J-B travel times were added. J-B travel times for different focal depths were tested to take care that the model resulting from the inversions was not biased by the initial choice of event depth.

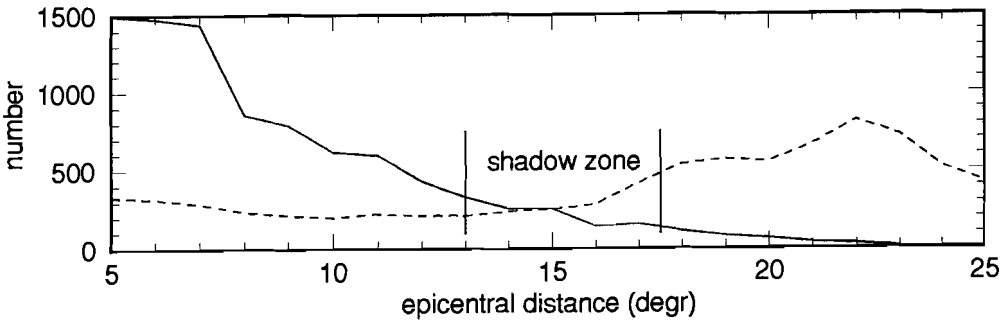

Figure 2.6. Number of data within a band of 14 s around the negative branch (solid line) and positive branch (dashed line) as a function of epicentral distance.

2.4 Inversion

Travel times were inverted using the generalized inversion technique with tapered eigenvector cut off (Wiggins, 1972). In the inversion a trade-off exists between depth resolution and variance in the model velocities. The number of eigenvectors determines this trade-off. The fit of the model to the data is measured by the relative deviation of the travel time data from the travel times as calculated for the model. The relative deviation corresponds to $\sqrt{\chi^2/N}$, where χ^2 is the statistical quantity and N the number of data. In the following $\sqrt{\chi^2/N}$ is briefly denoted by ξ. If ξ is too large the fit of the model is bad. "Too large" means too large compared to the value to be expected for ξ on the basis of a χ^2–distribution with $N-K$ degrees of freedom, K being the number of eigenvectors used in the inversion. The expected value for ξ is $\sqrt{(N-K-1)/N}$, for this inversion with 26 data and 11 eigenvectors equal to 0.73. A ξ well below this value should be avoided too since this means the model fit is too good in comparison to the estimated uncertainties in the data. Resolution is calculated by doing a separate "inversion", allowing uniform velocity changes over thick layers, thereby forcing the problem to be overdetermined. Inversion then gives the variance in velocity averaged over the layer.

The model resulting from the inversion procedure is influenced by subjective factors. The starting model has an influence on the result, probably due to the fact that the problem is underdetermined for detailed models. Also, inversion of travel times shows highly non-linear effects. In general, during the inversions the model was changed in such a way that the shadow zone became too large or too small compared to the observations (figure 2.6). In those cases the model had to be adjusted "by hand" to see that the requirements concerning the extent of the shadow zone were satisfied.

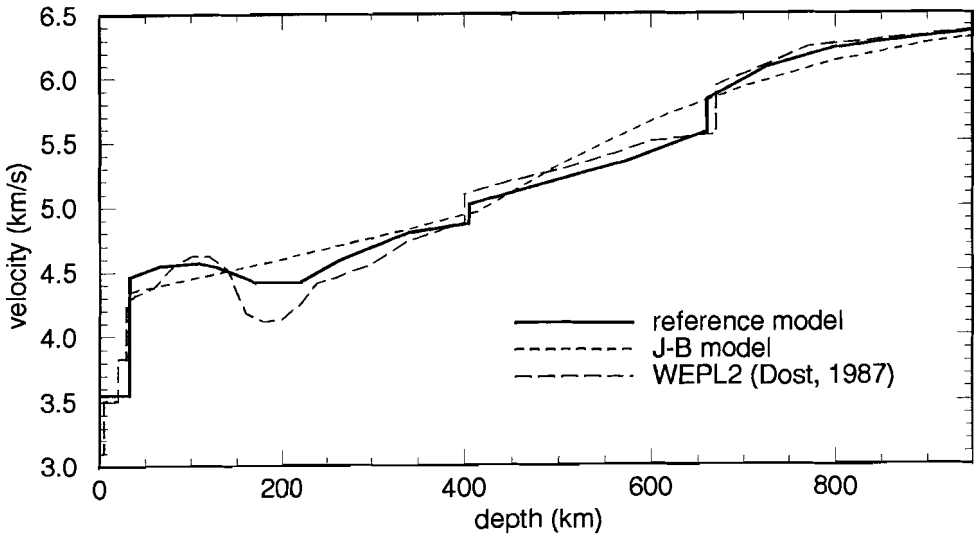

Figure 2.7. The new S model for Europe. For comparison, the models J-B and WEPL2 (Dost, 1987) are shown.

2.5 Results of travel time inversions

Several starting models were tested. These inversions resulted in different models that fit the first arrival travel times equally well. The preferred model is shown in figure 2.7. For this model, ξ=0.74. The velocities and the resolution are listed in table 2.1 and table 2.2. The experiments with different starting models provided some information about the uncertainties in the model. To start with, the exact shape of the LVZ is not resolved by the data. The LVZ of the preferred model has minimum velocity equal to 4.386 km/s, a gradient at 250 km and a discontinuity at 405 km, but two other models with a broad, less pronounced LVZ and minimum velocity of 4.5 km/s, one bounded by a discontinuity at 380 km, the other by a gradient of the same size centered at 325 km, were also permitted by the data. Neither the velocity jumps at the "400 km" nor the "660 km" discontinuity or their precise depths are well constrained. For instance, two models with a jump of about 0.2 km/s at 400 km but jumps of 0.09 km/s and 0.4 km/s respectively at 660 km fit the data equally well. These features are badly resolved by first arrival data only, whereas later arrivals - which presumably contain relevant information on these features - can not easily be identified. The delay density plot, however, provided some constraints to the velocity jumps at the major discontinuities. Between 17° and 26° the shape of the lowest density contours (see figure 2.8) indicates that later arrivals belonging to triplication branches were misidentified as first arrivals. This is likely to happen when the appearance of the first arrival on a seismogram is much weaker than of later arrivals. In a density plot of P delays

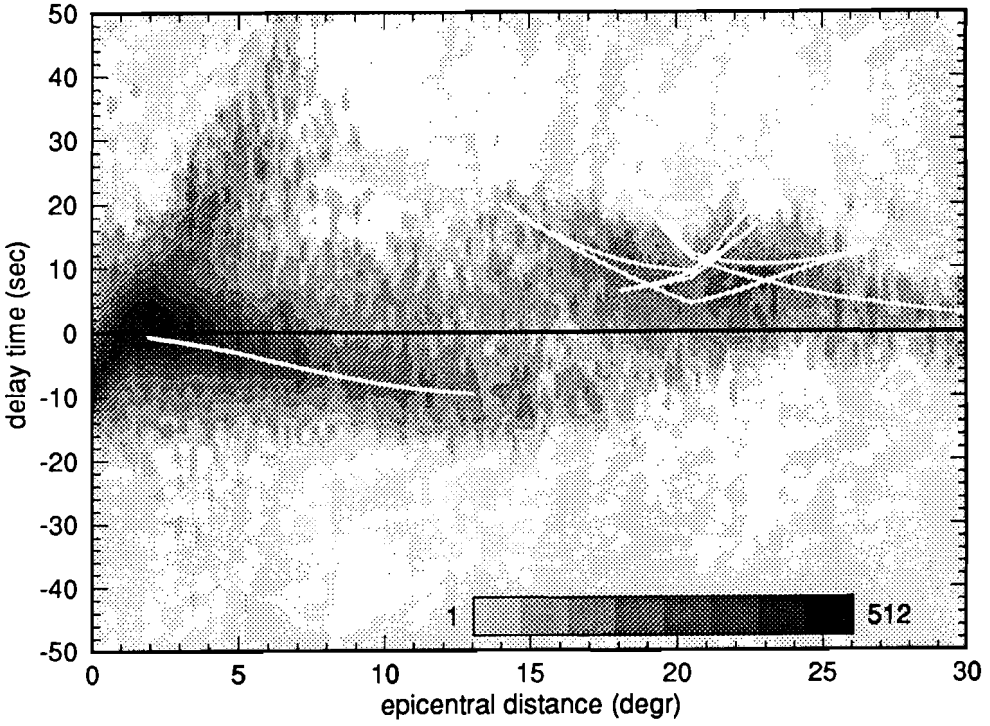

Figure 2.8. Travel time curve of the model relative to J-B travel times. The number of data in bins of 0.2° × 2 s is contoured according to the scale in the figure..

for the same area triplications are more clearly visible since there are many more P registrations (Spakman, pers. comm.). Therefore, with trial and error the velocity jumps of the model resulting from the inversion were adjusted to achieve that the corresponding triplications would match the density plot. Figure 2.8 shows that the travel time curve of the model fits well to the delay time data. The shadow zone extends between 13° and 18° but the triplication branch corresponding to the 400 km discontinuity folds back to 14°. A point supportive of the reality of this model is that its main features are in agreement with the WEPL2 model recently derived from dispersion measurements of higher modes (Dost, 1987, see figure 2.7).

2.6 Evidence for lateral heterogeneity from ISC S delays

As a preliminary study to the tomographic inversion of ISC S delays it was investigated whether lateral variations in the upper mantle below Europe are reflected by the values of these data. For four regions with a different tectonic history, the Baltic Shield, the Hercynian Belt, the Alps and the Balkan region, the behaviour of S delays as a function of epicentral distance was investigated. The boundaries of the four regions are indicated in

Table 2.1: Velocities

depth (km)	v_s (km/s)	depth (km)	v_s (km/s)
0.0	3.550	405.0	4.820
33.0	3.550	405.0	5.041
33.0	4.460	500.0	5.249
67.0	4.578	600.0	5.468
108.0	4.601	660.0	5.600
128.0	4.570	660.0	5.860
171.0	4.390	725.0	6.066
226.0	4.386	800.0	6.211
276.0	4.596	850.0	6.275
340.5	4.708	950.0	6.335

Table 2.2: Resolution

depth (km)	v_s (km/s) averaged over Δz	st dev (km/s)	vertical resolution Δz (km)
16.5	3.550	0.12	33
50.0	4.519	0.059	34
108.0	4.601	0.061	82
200.0	4.388	0.017	102
328.0	4.687	0.048	154
469.0	5.181	0.048	128
596.5	5.460	0.19	127
745.0	6.105	0.087	170

Figure 2.9 (opposite page). Delays associated to rays located within the Baltic Shield (region 1, fig 2.2) as a function of epicentral distance.

Figure 2.10. Density plot of delays associated to rays bottoming below the Hercynian Belt (region 2, figure 2.2), as a function of epicentral distance. The number of delays per square area of 0.5° ×1 s is contoured with intervals shown in the legend.

Figure 2.11. Density plot of delays associated to rays bottoming below the Alps (region 3, figure 2.2), as a function of epicentral distance. The number of delays per square area of 0.5° ×1 s is contoured with intervals shown in the legend.

Figure 2.12. Density plot of delays associated to rays bottoming below the Balkan region (region 3, figure 2.2), as a function of epicentral distance. The number of delays per square area of 0.5° ×1 s is contoured with intervals shown in the legend.

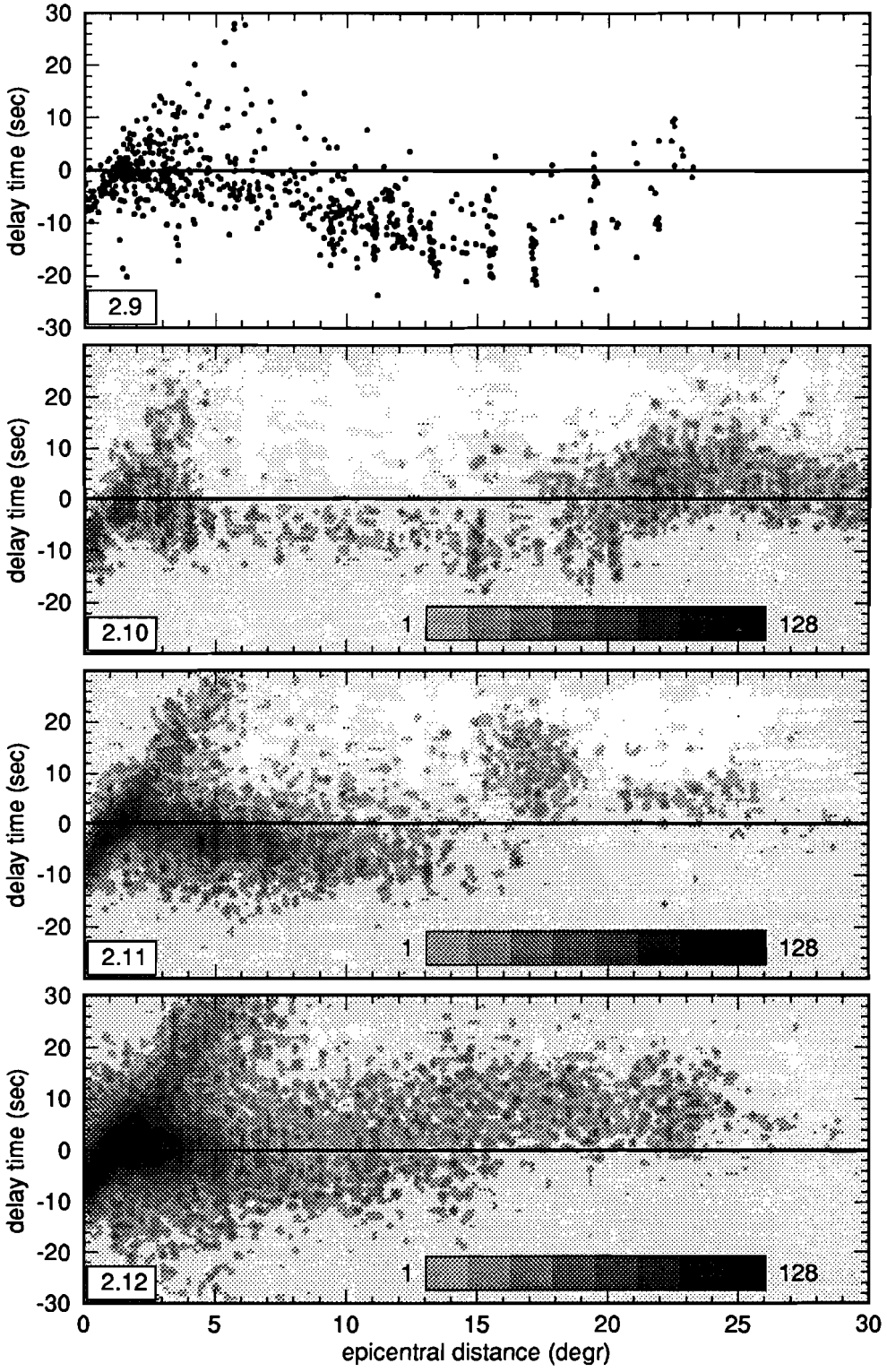
delay time (sec)
epicentral distance (degr)
2.9
2.10
2.11
2.12
1
128

figure 2.2. Figure 2.9 shows the diagram of S delays belonging to ray paths that fall within region 1 (see figure 2.2), which encompasses the Baltic Shield. The other three regions are too small for rays with considerable epicentral distances to fall completely within the region. Therefore, for regions 2-4 delays belonging to ray paths that have the turning point below these regions were plotted as a function of epicentral distance (figures 2.10-2.12). The four diagrams exhibit similar features. At short epicentral distance delays are predominantly negative (figures 2.9-11) or distributed around 0 s (figure 2.12). At larger distances, the average value of the delays as a function of epicentral distance becomes (more) positive. The negative delays at shorter epicentral distances belong to waves that bottomed within the high velocity lid. The more positive delays at larger distances belong to waves that bottomed below the LVZ or in the transition zone. The diagrams demonstrate that the distance at which the average value of the S delays changes from negative to positive differs among these regions. For the Baltic Shield and the Hercynian Belt this distance is about 20°, for the Alps about 13°, and for the Balkan region somewhere between 11° and 15°. This observation explains why in figure 2.3, which shows delays of waves bottoming below Europe, the negative and positive branches are present between approximately 11° and 20°. Furthermore, the diagrams indicate that the average value of delays as a function of epicentral distance is different for these regions. The largest, negative, delays for waves bottoming within the high velocity lid are reported for the Baltic Shield and they become increasingly more positive for the Hercynian Belt, the Alps and the Balkan region. For example, at an epicentral distance of 10° the average value of delays is -10 s on the Baltic Shield, -7 s, -4.5 s and 0 s for the Hercynian Belt, the Alps and the Balkan region, respectively. The behaviour of S delays as a function of epicentral distance indicates that the lid velocity is highest below the Baltic Shield and decreases with age of the tectonic provinces.

2.7 Concluding remarks

The delay density plot shows that there is a significant, systematic deviation of observed S travel times in Europe from J-B travel times. This means that the average velocity structure of the upper mantle beneath Europe differs significantly from the J-B model. A new S model has been derived from the ISC data set. Figure 2.1 shows that the distance between ray paths as calculated for the J-B model and this model, in the introduction referred to as "a more realistic model", can be up to 200 km. Therefore, the J-B model is inadequate as a reference model for tomographic imaging of the S velocity of Europe's upper mantle. Diagrams of S delays associated to rays bottoming below different tectonic regions in Europe against epicentral distance show that these data contain information about heterogeneity in Europe's upper mantle, which is encouraging for a tomographic interpretation of these data.

Chapter 3

3-D structure from ISC S delays

3.1 Introduction

Linearized body-wave tomography with P delay-time data published by the International Seismological Centre (ISC) proved to be a powerful tool in imaging aspherical variations in seismic velocity in the Earth's interior (Dziewonski, 1984; Spakman, 1988, 1991; Inoue et al., 1990; Van der Hilst et al., 1991). In this study we apply body wave tomography to ISC S-wave travel-time residuals to obtain a three dimensional (3-D) model of variations in S-wave velocity in the upper mantle below Europe. Like 3-D models of P-wave velocity, a 3-D model of the S wave velocity is of interest by itself. More importantly, however, knowledge on both P- and S-wave velocity enables the interpretation of seismic structure in terms of thermal and compositional variations (Yan et al., 1989; Furlong et al., 1992).

Compared with P delay-time tomography, there are the following difficulties. First, the ISC reports far less S delays than P delays. Second, S phases arrive in the coda of other waves and, as a consequence, the reported phase data are subject to much larger errors caused by inaccurate readings. Third, S waves are more difficult to identify than P waves. For example, an Sp wave can easily be misidentified as an S wave. Yet, a correlation between tectonic provinces and S residuals corresponding to ray paths bottoming in the upper mantle below Europe exists (chapter 2), despite the relatively large data errors. This indicates the presence of structural signal in the ISC S data, which encouraged us to attempt

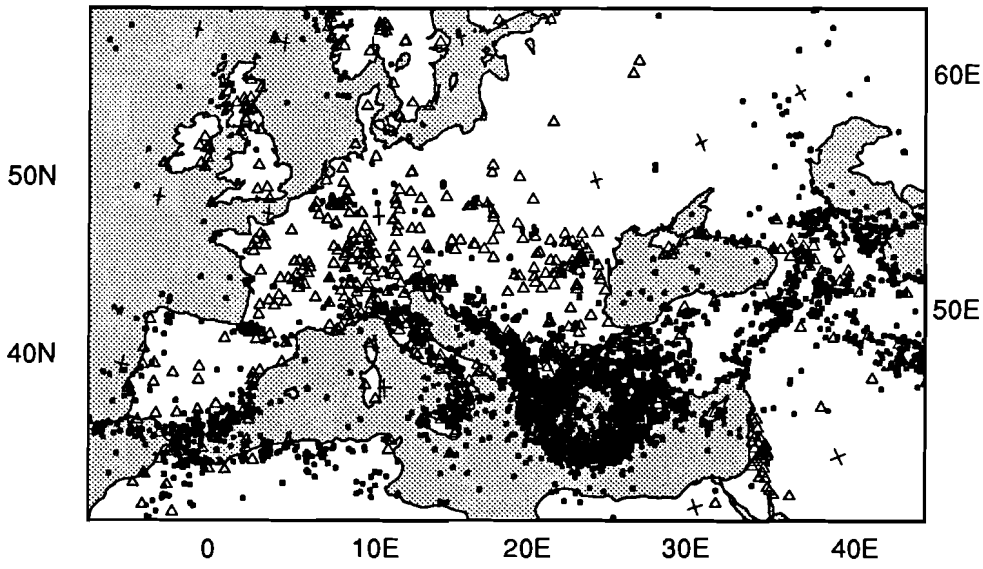

Figure 3.1. Map of the study region. Epicenters of events of magnitude Mb ≥ 4 are plotted with dots. Station locations are indicated with triangles.

a tomographic interpretation of this data set. Fourth, lateral heterogeneity in upper mantle S-wave velocity is larger than in P-wave velocity. Paulssen (1987) concluded, from modelling broadband P and S waveforms, that lateral heterogeneity in Europe's upper mantle above the 400 km discontinuity is at least 4% for S waves and 2.5% for P waves. Snieder's model (1988) of the lithosphere and low velocity zone below Europe shows perturbations in the S velocity up to 5%, while the P velocity perturbations in Spakman's model (1988) are not larger than 3%. Therefore, we expect that the use of a 1-D reference model to linearize the inversion of S residuals is less accurate than a similar approximation for P wave tomography. The reference model is used to predict the ray paths associated to the delay time data, and should therefore be an adequate description of the average S velocity below the study region. This subject has been discussed by Zielhuis et al. (1989) and, for a study with P-data, by Van der Hilst and Spakman (1989). In chapter 2 we derived a 1-D reference model for the S-wave velocity below Europe from ISC S delays reported in the period 1972-1982. By the time we started with the 3-D inversion, data from the period 1964-1986 became available to us. On the basis of this enlarged data set, we slightly modified the reference model with trial and error (similar to the procedure described in chapter 2) in order to better fit the triplication branches which are more clearly visible in de delay time vs epicentral distance plot of the larger data set (see figures 2.8 and 3.2). Here, we use this 1-D reference model. Finally, it is unknown if the reported delay

times belong to the horizontal or vertical component of the S wave. Little is known about the strategy followed by operators at seismic stations to pick a seismic phase. In general, S waves are picked from the long-period vertical or horizontal component of the seismogram, depending on which component they appear most clearly (R. D. Adams, and K. van Gent, pers. comm.). In regions where many dip-slip events occur, S phases are picked from the vertical component, while in regions with predominantly strike-slip events S phases are identified from the horizontal components (R. D. Adams, pers. comm). Thus, we probably inverted delay times belonging to SH and SV waves. Since we inverted for average velocity perturbations, transverse anisotropy, if present, influenced the value of the velocity perturbations in parts of the model that were sampled by rays with a predominant direction.

Despite the complications mentioned above, we performed in this study a 'standard' inversion of the S-wave travel-time residuals. We assumed that ray paths for all delay time data can be calculated accurately enough with a 1-D reference model, and that errors in the data have a Gaussian distribution. We used a least squares formalism, but to avoid that outliers contaminate the inversion result we used a simple cut-off criterion: we rejected delays with an absolute value exceeding a set maximum.

In this chapter we do not describe the result of the delay time inversion in detail. Instead, we compare in chapter 7 the model obtained here with results of the Partitioned Waveform Inversion.

3.2 Parameterization of the model

In Figure 3.1 we show the region under study. Following common practice, the Earth volume below the study region was parameterized with non-overlapping cells in which seismic velocity is assumed to be constant. In this study, the horizontal dimension of the cells is $2° \times 2°$; in vertical direction, the cells vary in height from 33 km at the surface to 150 km at a depth of 1370 km, i.e., in the lower mantle. This parameterization yielded 9600 cells.

3.3 Data selection

In the Bulletins of the International Seismological Centre, S delays are labelled either as the phase identification by the operators at the seismic stations (OPID) or as an ISC identification (ISCID). After hypocenter location, arrival times of secondary phases are analysed with the Jeffreys-Bullen (J-B) travel-time tables and associated to a phase when the residual falls within the association window ($\pm 7.5s$) (Arnold et al., 1968; Adams et al., 1982). This identification procedure is carried out only for observations at epicentral distances larger than 25 °. If successful, the data are labelled as ISCID.

From the Bulletin tapes of the ISC (Jan 1964 - Oct 1986) we selected ISCID and OPID S delays that are associated to earthquakes with body wave magnitude $m_b > 4$, reported by at least 10 stations, and correspond to ray paths that cross the parameterized mantle volume below the study region. The (subjective) restrictions on event magnitude and minimum number of recording stations were invoked with the objective to reject data from

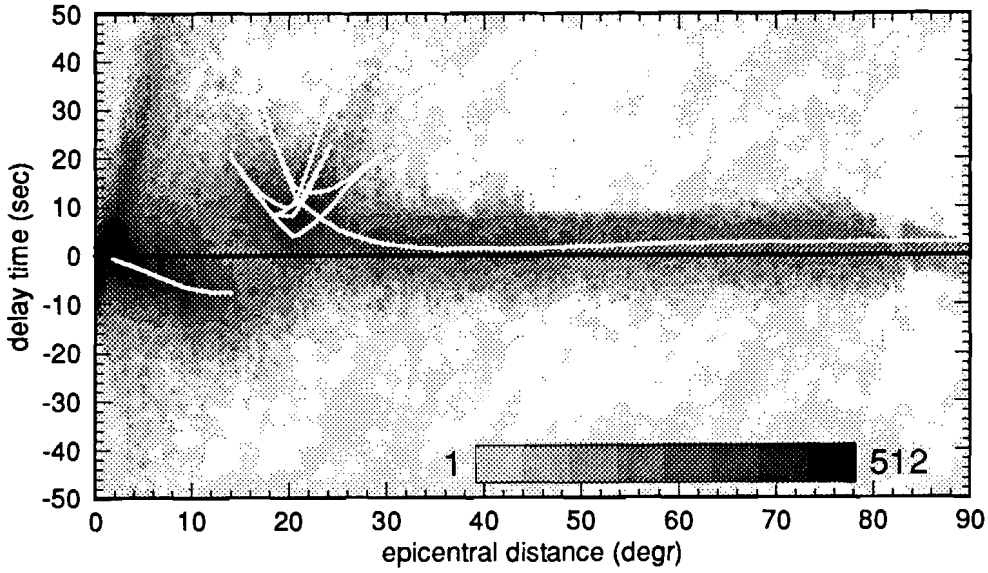

Figure 3.2. Selected S delay times (250,000) against epicentral distance. The density of data per area of 0.5° × 1 s is contoured with the grey scale shown in the legend.

earthquakes with hypocenters that are not reliably located.

3.4 The quality of the data

The selected delay times are plotted as a function of epicentral distance in figure 3.2. The scatter in the delay time data shown in figure 3.2 is due to data errors and effects of lateral heterogeneity. Before inverting the data, we assessed the noise level in the data. In this section we discuss the following contributions to data errors: mispicks (or erroneous phase associations), random reading errors, and errors due to hypocenter mislocation.

Figure 3.2 shows that, in particular at regional epicentral distances, many phases can be misidentified as direct S waves. The steep positive branch between 0° and 8° consists of delays corresponding to S_g phases misidentified as S phases. The negative branch from -20 s at 0° to -50 s at 3° coincides with the travel time difference between P and S waves as predicted by the J-B travel time tables. Thus, these delays probably belong to P waves which were misidentified as S waves. Between 14° and 28° the travel time curve has triplication branches due to first order discontinuities in seismic velocity at depths of 400 and 670 km. In this epicentral distance range, many S waves were reported as the first arriving S waves, although they actually belong to one of the triplication branches. The distribution of delay times in figure 3.2 vaguely reflects the contours of the triplication branches. Beyond 30° the scatter in the delays reduces significantly. At approximately 82° the SKS travel time curve crosses the travel time curve of S waves. The gaps in the density

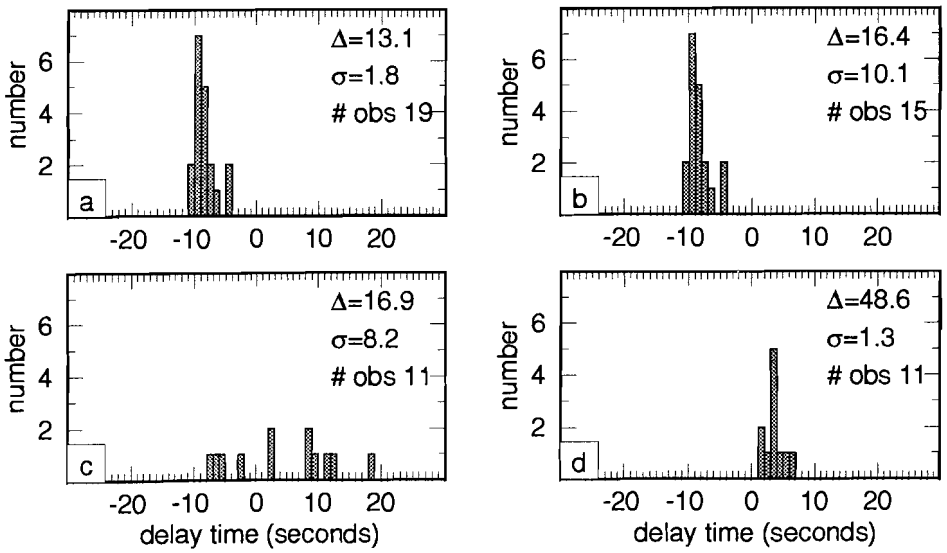

Figure 3.3. Histograms of delays reported at station DOU from clusters at different epicentral distances. The epicentral distance, Δ, the standard deviation of the delays, σ, and the number of delays reported, # obs, are indicated in the figures.

plot at this distance reflect the ISC association procedure: the reported phases are identified by the ISC as the phase that arrives closest to the predicted phase by the J-B model. For the subsequent error analysis and inversion we selected data from 3° to 82° to avoid that S_g and SKS phases are in the data set. Although the S_g branch extends to 8°, we choose 3° as a lower boundary because values of delays belonging to this branch are larger than the delays that we planned to select for inversion.

In order to separate data errors from structural signal, we estimated the magnitude of data errors by examining data corresponding to composite rays. These data are obtained by assembling, for a specific station, all delays associated to earthquakes that occur within a small volume in the Earth (an event cluster). In our analysis we used event clusters of $0.5^0 \times 0.5^0 \times 35 km$. We assumed that for clusters of this size lateral heterogeneity contributes equally to all delays, because the waves travel along approximately the same ray path. The delays contributing to a composite ray are, however, influenced by hypocenter mislocation, which is mainly caused by near source heterogeneity and an uneven distribution of recording stations. Since near-source heterogeneity is approximately equal for events located within the same cluster, its effect probably contributes to bias in the delays rather than to scatter. In contrast, the distribution of stations that record an earthquake depends on the magnitude of the seismic event, which can be different for sources within a single cluster. Consequently, the variation of magnitude for seismic events within a cluster can contribute to the variation of S delays. Thus, at one station, the variation of S delays

associated to events located within the same cluster is influenced by reading errors (mispicks, inaccurate readings), specific errors in hypocenter location, and, possibly, instrument errors and event-magnitude dependent instrument bias (Grand, 1990). The level of data errors at one station is estimated from the variance of all delays that belong to one event cluster. As an example we show in figure 3.3 the variation in S delays reported at station DOU (Dourbes, 50.09N, 4.59E) The delays in figure 3.3a are from an event cluster centered at 13° from station DOU and have a standard deviation of 1.8 s. In figure 3.3b and 3.3c the delays form two groups: one belongs to the negative branch in figure 3.2 corresponding to rays bottoming in the high velocity lid, the other one belongs to the positive triplication branches. The standard deviation of the delays in figures 3.3b and 3.3c is large: 10.1 and 8.1 s, respectively. At teleseismic distances S phases are picked more accurately, which is also illustrated by figure 3.3d: the standard deviation of delays from an event cluster at 48° is 1.3 s.

We calculated the variances of all event-cluster vs. station combinations with more than 2 delays. Absolute delays larger than 25 s were excluded because we do not consider them reliable. Then, we estimated the standard error in a delay time in different epicentral distance intervals from the variances of all cluster-station combinations in that distance range. The estimator for the standard deviation of delays in one interval is (Gill, pers. comm.):

$$\sigma = \left[\sum_j \left[\frac{n_j \sigma_j^{\,2}}{\sum_j n_j} \right] \right]^{1/2}$$

where n_j is the number of delays in the jth event-cluster/ station combination, and $\sigma_j^{\,2}$ the variance of delays within this combination. This analysis yields the following standard errors for delay time data:

$$3° - 14°: \ \sigma = 4.8\ s$$
$$14° - 28°: \ \sigma = 5.0\ s$$
$$28° - 82°: \ \sigma = 3.2\ s$$

3.5 Inversion method

We applied the method of linearized delay time tomography as developed by Spakman and Nolet (1988). Details of this method are discussed by Nolet (1985) and Spakman and Nolet (1988). The delay time data were inverted simultaneously for slowness perturbations to the reference model, for station delays, and for corrections to the event origin times. A station delay is a parameter that is assumed to absorb the delay acquired along ray path segments between the cell model and stations located outside the study region. We did not invert for perturbations to the spatial components of hypocenters, because the distribution of the stations reporting S delays is much more uneven than the distribution of the stations reporting P delays. Because the tomographic system of equations is usually

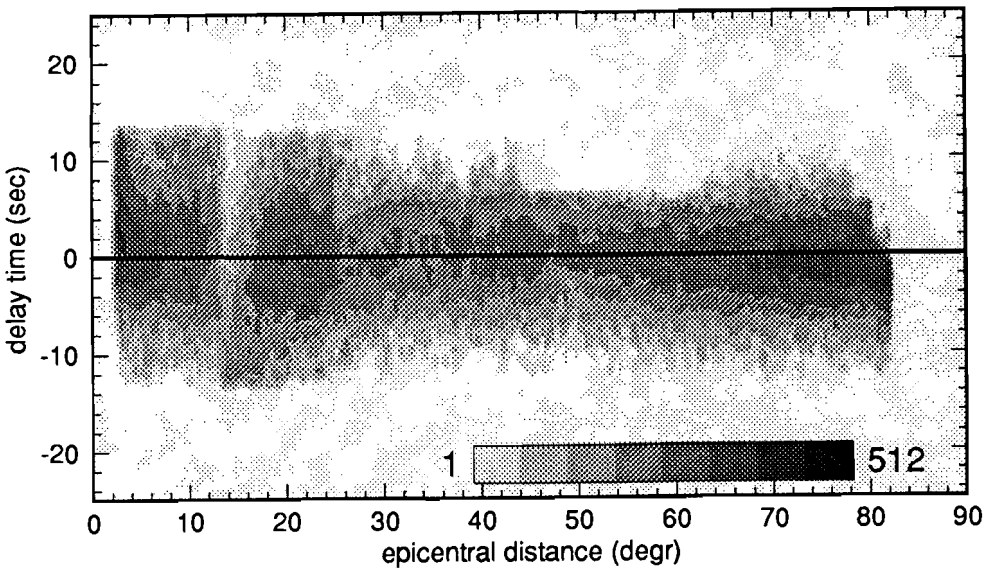

Figure 3.4. Delay times with respect to the travel time of the new reference model as function of epicentral distance. The density of data per area of 0.5° × 1 s is contoured with the grey scale shown in the legend.

underdetermined we followed Spakman and Nolet (1988) and appended a diagonal damping matrix to the system of equations. In order to obtain a smooth solution, we used a smoothing operator (Spakman and Nolet, 1988) in the inversion. The matrix elements were scaled with the square root of the cell volume to minimize the influence on damping of the solution of differences in cell volume (Nolet, 1987a). Matrix rows were weighted with the standard error for corresponding data as estimated above.

To reduce the number of unknown parameters in the inversion, we constructed composite rays (Spakman and Nolet, 1988). When we assume that the correction of the origin time is similar for events that are spatially close together we can compute a correction for a group, or a *cluster*, of events instead of a correction for individual earthquakes. For the geographical region between 40W and 70E longitude, and 10N and 90N latitude, earthquakes were grouped in clusters of 0.5° × 0.5° × 35 km; for events elsewhere clusters of 1.8° × 1.8° × 100 km were used. Rays from an event cluster to a station construct a composite ray. The median of the delays is taken as the delay time datum for the composite ray. Matrix rows consisting of composite rays, are weighted with the standard deviation of the delays contributing to the ray, divided by the square root of their number.

To investigate the reliability of the result, we performed sensitivity tests (Spakman and Nolet, 1988) in which data calculated from a known input model are inverted. The

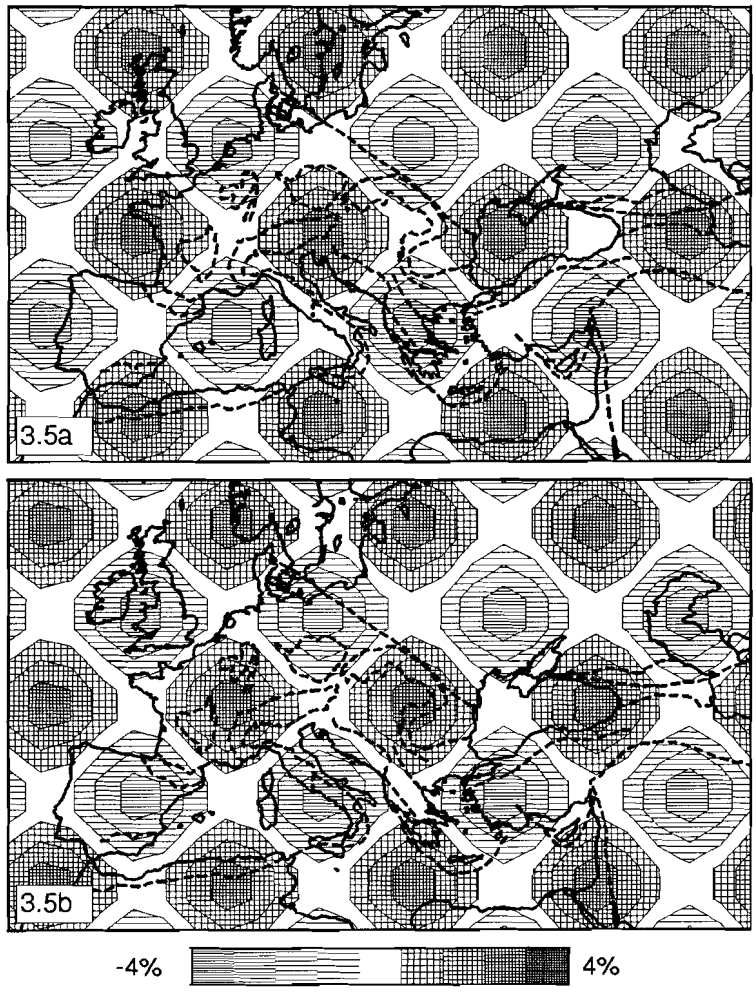

Figure 3.5. a) Harmonic input model for odd layers. b) Harmonic input model for even layers.

contamination of the real data by errors was simulated by adding noise to the synthetic data. The noise had a Gaussian distribution with standard deviation equal to the estimated standard error for the epicentral distance range under consideration. Figure 3.5a and 3.5b shows the anomaly pattern of the input model with harmonic velocity variations. By comparing the inversion response with the input model, we can assess how well the S-wave velocity perturbations are resolved. However, the diagnostic value of sensitivity tests for the investigation of the reliability of the results of delay-time tomography studies is limited

because (cf. Van der Hilst et al., 1992): (1) the synthetic data are not biased due to possible hypocenter mislocation; (2) systematic errors in the data are not modelled; and (3) these tests are not sensitive to inadequacies of the linearization about the reference model and initial hypocenter locations, because synthetic data are always consistent with the reference ray paths. However, since no tests are available with which we can systematically examine the resolution in the whole 3-D model, we used them in the resolution analysis.

3.6 Inversion of the delay time data

The ISC delays were converted into residuals with respect to the travel time in the new reference model (see Van der Hilst (1990) for the details of this conversion procedure). In figure 3.4 we plotted the newly determined delays against epicentral distance. We performed separate inversions of travel time residuals with absolute values (with respect to the new reference model) smaller than 12, 9 and 6 s, respectively. The resulting models exhibited features that indicated that the reference model used does not adequately represent the laterally averaged upper mantle velocity below Europe: the average value of the anomalies is positive between 128 and 405 km, and negative between 405 and 490 km. Although we cannot exclude that this effect was caused by outliers, the fact that the average value of the velocity anomalies deviates systematically from zero over a certain depth range suggests small deficiencies of the reference model. It would require further research to investigate the effects on the reference ray paths used in the inversion, and to assess the adequacy of the linearization about the reference model used here. The systematic deviation of the velocity anomalies is rather small in the result of the inversion of data with an absolute residual smaller than 6 s. Therefore, we preferred this model.

Selection of a rather narrow delay time window implied a severe damping constraint on the solution. It is likely that we rejected accurate readings with a delay time larger than 6 s. We also rejected accurate data that can not be used in a linearized inversion. We infer from figure 2.9 that data corresponding to rays bottoming below the Baltic Shield have residuals with respect to the new reference model that exceed the maximum accepted value of 6 s between 13° and 20°. This implies that these data were not used, although they contain structural signal. The use of these data, would, however, not be warranted in a linearized inversion. With the current 1-D reference model, delays at stations between 13° and 20° are associated to the triplication branches of the travel time curve that correspond to rays bottoming in the mantle below 400 km, whereas the Baltic Shield delays are clearly associated to rays bottoming within the high velocity lid. In order to predict correctly the ray paths associated with these delays, a 3-D reference model is required, or at least different 1-D reference models for shield areas and younger tectonic provinces. The latter approach was followed by Grand (1987).

The original estimates of the errors in the data were based on a selection of delays within a time window of [-25 s, +25 s]. Residuals with absolute values less than 6 s - with respect to the new reference model - are likely to have smaller errors. We recomputed the standard error for these data: $\sigma = 3.5, 3.7$, and $2.9\ s$ for epicentral distance intervals of 3° -

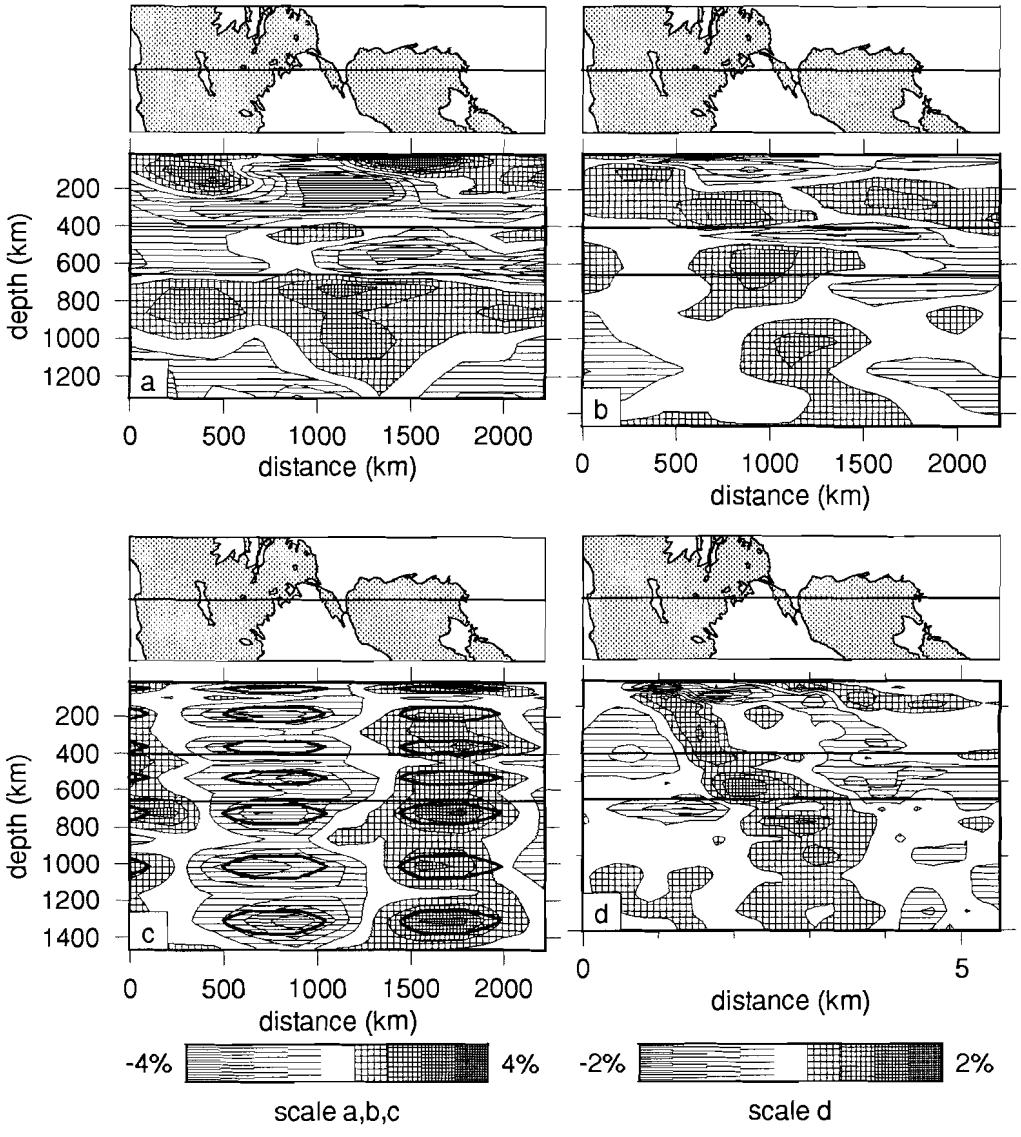

Figure 3.6. a) vertical section through model EURS89A (model obtained with J-B reference model). The location of the section is indicated in the rotated map above the sections. b) vertical section through EURS89B. c) vertical section through the result of harmonic sensitivity test. The contours of the input model are indicated with thick lines. d) vertical section through the P velocity model of Spakman et al. (in preparation).

14°, 14° - 28°, and 28° - 82°, respectively.

From the 142,000 delays selected we constructed, by the clustering procedure, approximately 68,000 matrix rows. The number of unknown parameters in the inversion was about 15,390: 9,600 cell slowness perturbations, about 4,900 origin time corrections, and 890 station delays. The inversion yielded a value for χ^2/n equal to 1.12, where n is the number of data in the inversion.

To investigate the influence of the reference model we also inverted the original ISC delays, using the JB model for linearization. Because we wanted to include in this inversion all data that were involved in the inversion with the new reference model, we had to use a wider delay time window of [-15 s, +15 s]. This implied, however, also a much larger risk of severe contamination of the solution by outliers. Hereafter, we refer to the result obtained with the J-B reference model as EURS89A, to the result obtained with the new reference model as EURS89B. EURS89A yielded a value of χ^2/n equal to 2.6.

3.7 Results

3.7.1 Influence of reference model

In Figures 3.6a and 3.6b we show an upper mantle section across the Hellenic Arc - Black Sea region through EURS89A and EURS89B, respectively. We also show the vertical sections through the inversion response to the harmonic input model, calculated with ray paths in the new reference model (Figure 3.6c). The cross section of figure 3.6b reveals a zone of high velocity anomalies dipping towards the northeast. These anomalies form the image of the high velocity slab below the Hellenic arc, which is also imaged by Spakman (1988) and Spakman et al. (in preparation) with P delay-time tomography. The vertical section through the P-wave velocity model resulting from the latter study is presented in figure 3.6d.

The vertical section through EURS89A (figure 3.6a) shows a continuous zone of low velocities between 200 and 400 km and high velocities between 670 and 1000 km. Although we cannot assess which influence outliers had on model EURS89A, the fact that these features are consistent over a certain depth range strongly suggests that they are caused by the deficiencies of the J-B model. These are the absence of a low velocity zone and a 400 and 670 km discontinuity. Similar observations were made by Van der Hilst and

Figures 3.7 - 3.15. (next 6 pages) For each layer:
a) S velocity perturbations of EURS89B; b) Result of the harmonic sensitivity test.
Figure 3.7: layer 1 (0-33 km); Figure 3.8: layer 2 (33-70 km); Figure 3.9: layer 3 (70-128 km); Figure 3.10: layer 4 (128-242 km); Figure 3.11: layer 5 (242-324 km); Figure 3.12: layer 6 (324-405 km); Figure 3.13: layer 7 (405-490 km); Figure 3.14: layer 8 (490-575 km); Figure 3.15: layer 9 (575-670 km).

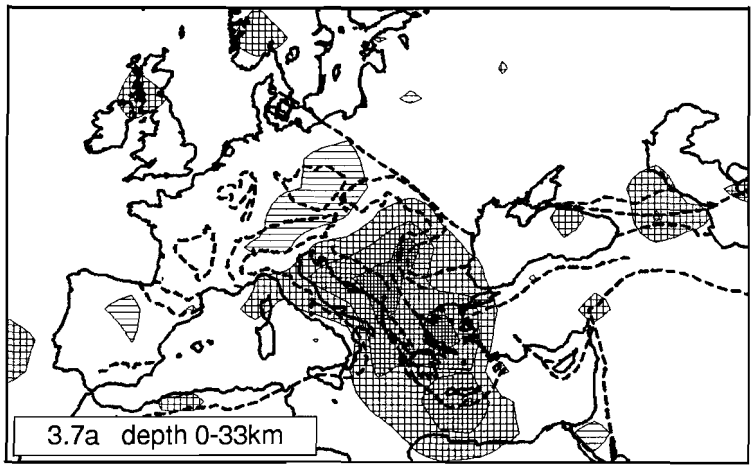
3.7a depth 0-33km

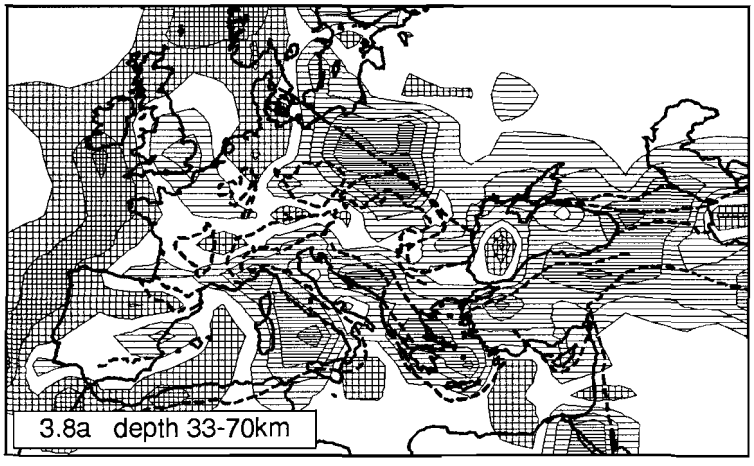
3.8a depth 33-70km

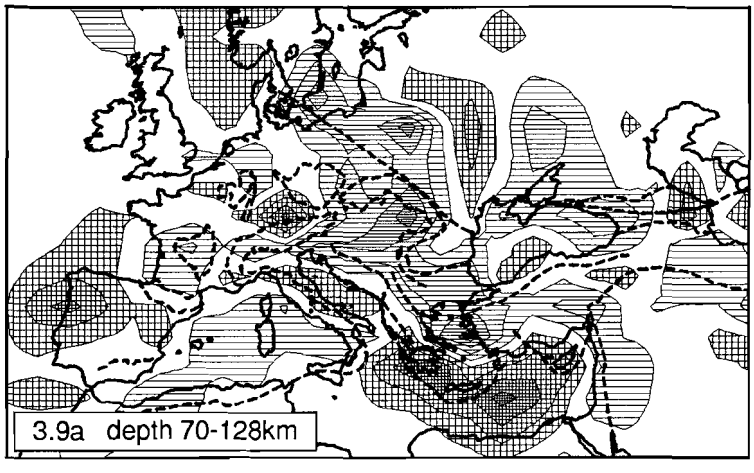
3.9a depth 70-128km


-4%
4%

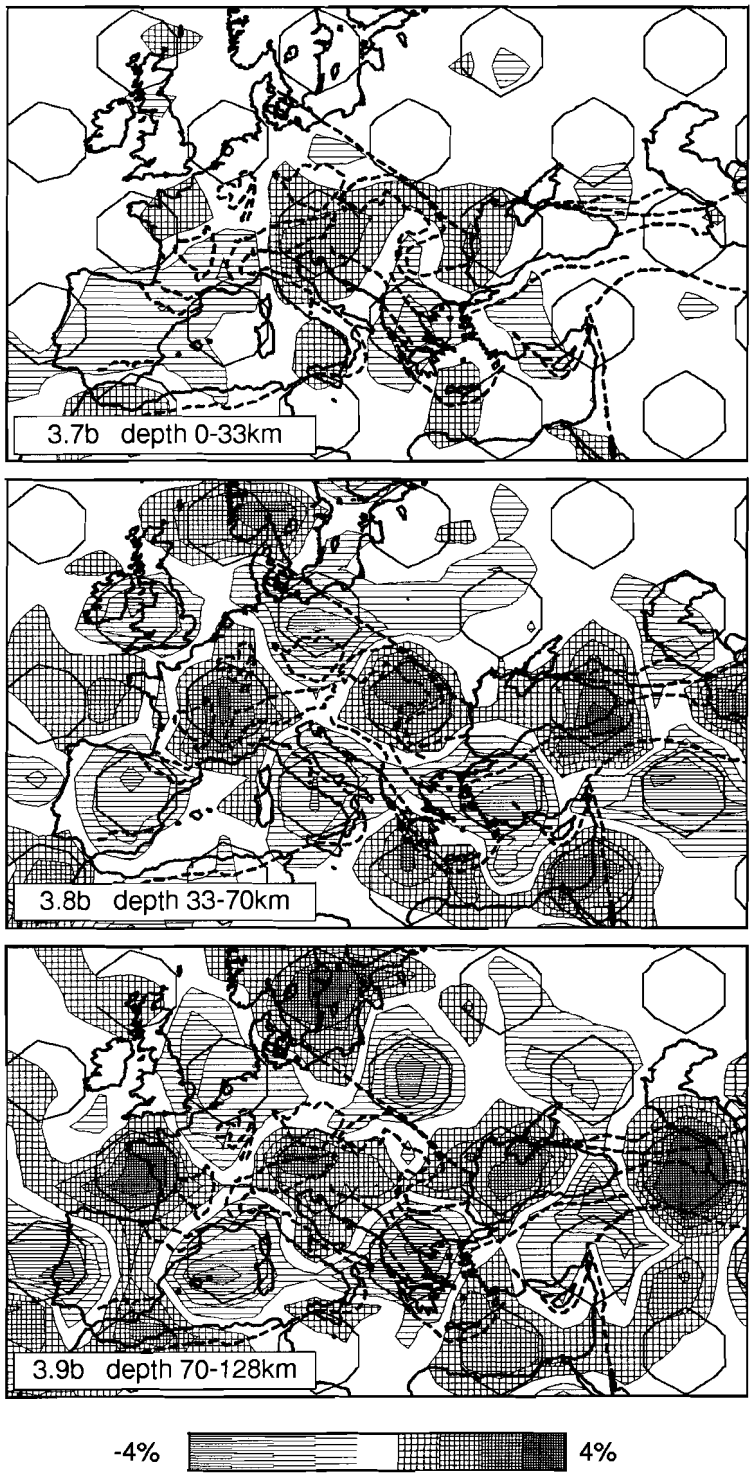
3.7b depth 0-33km
3.8b depth 33-70km
3.9b depth 70-128km
-4%
4%

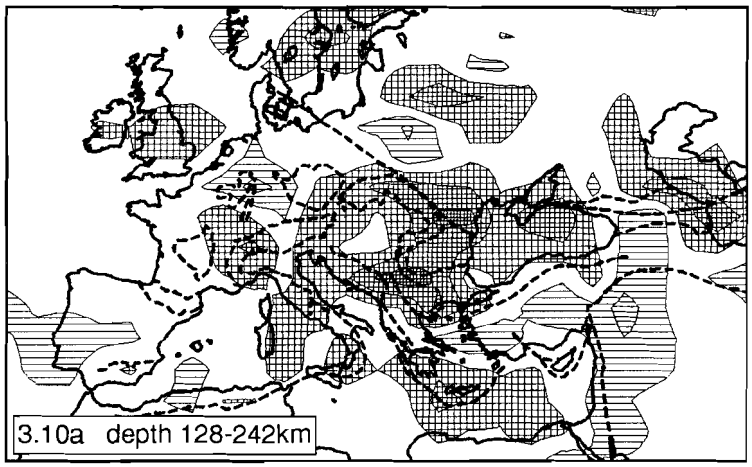
3.10a depth 128-242km

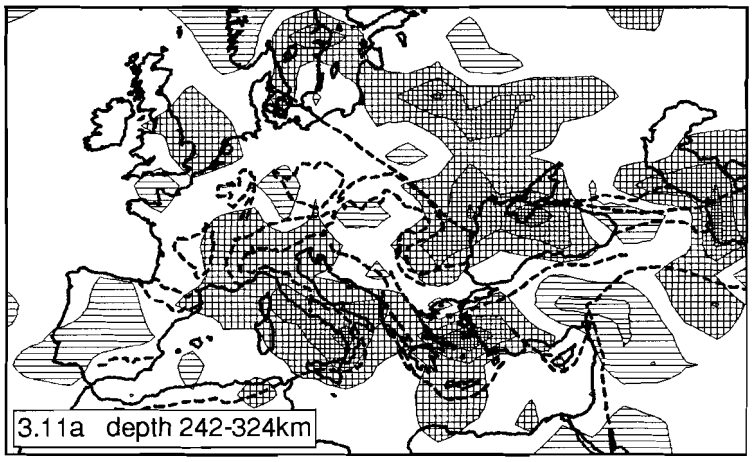
3.11a depth 242-324km

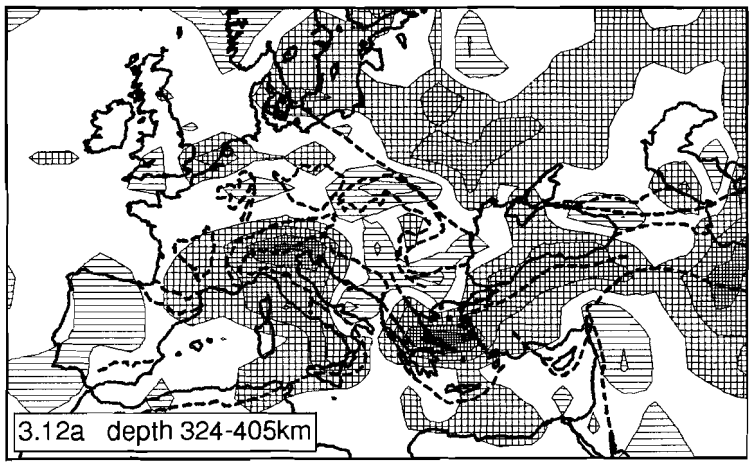
3.12a depth 324-405km


-4%
4%

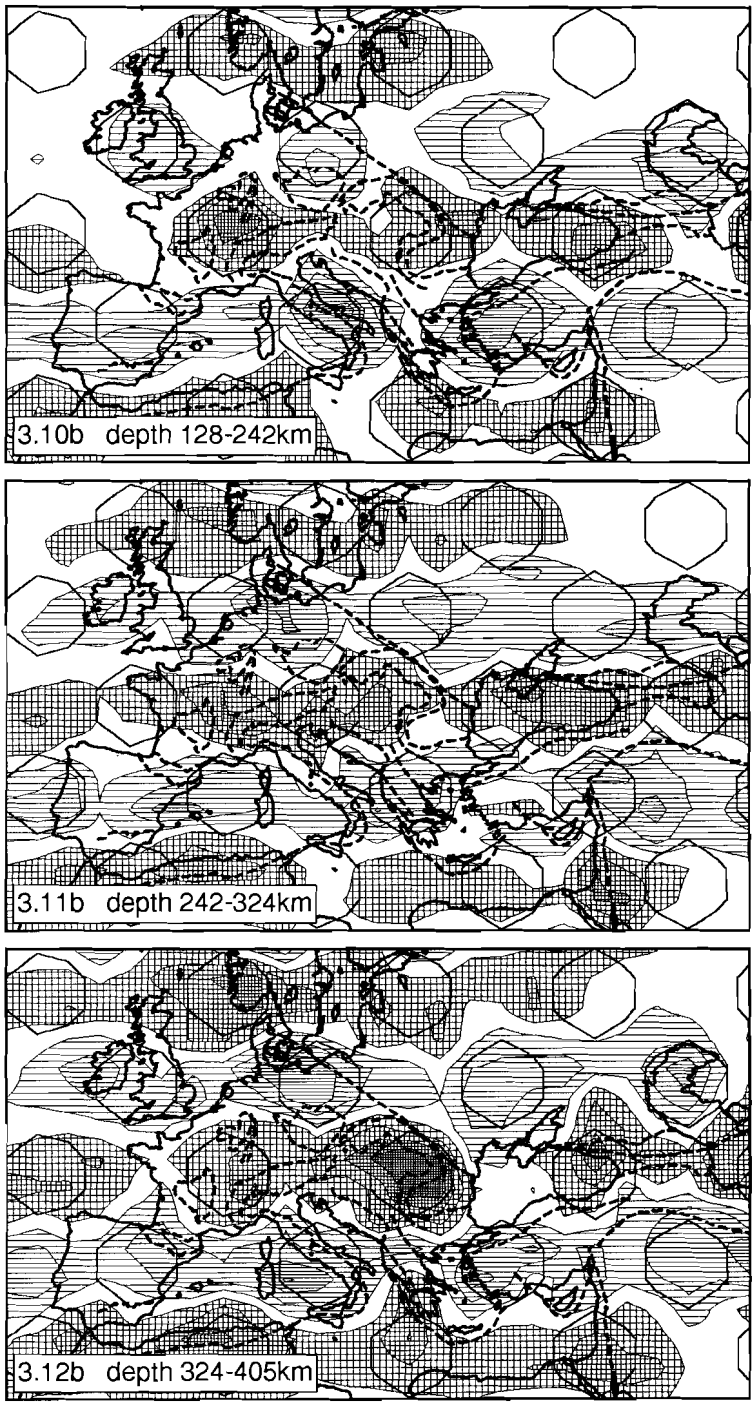
3.10b depth 128-242km
3.11b depth 242-324km
3.12b depth 324-405km
-4%
4%

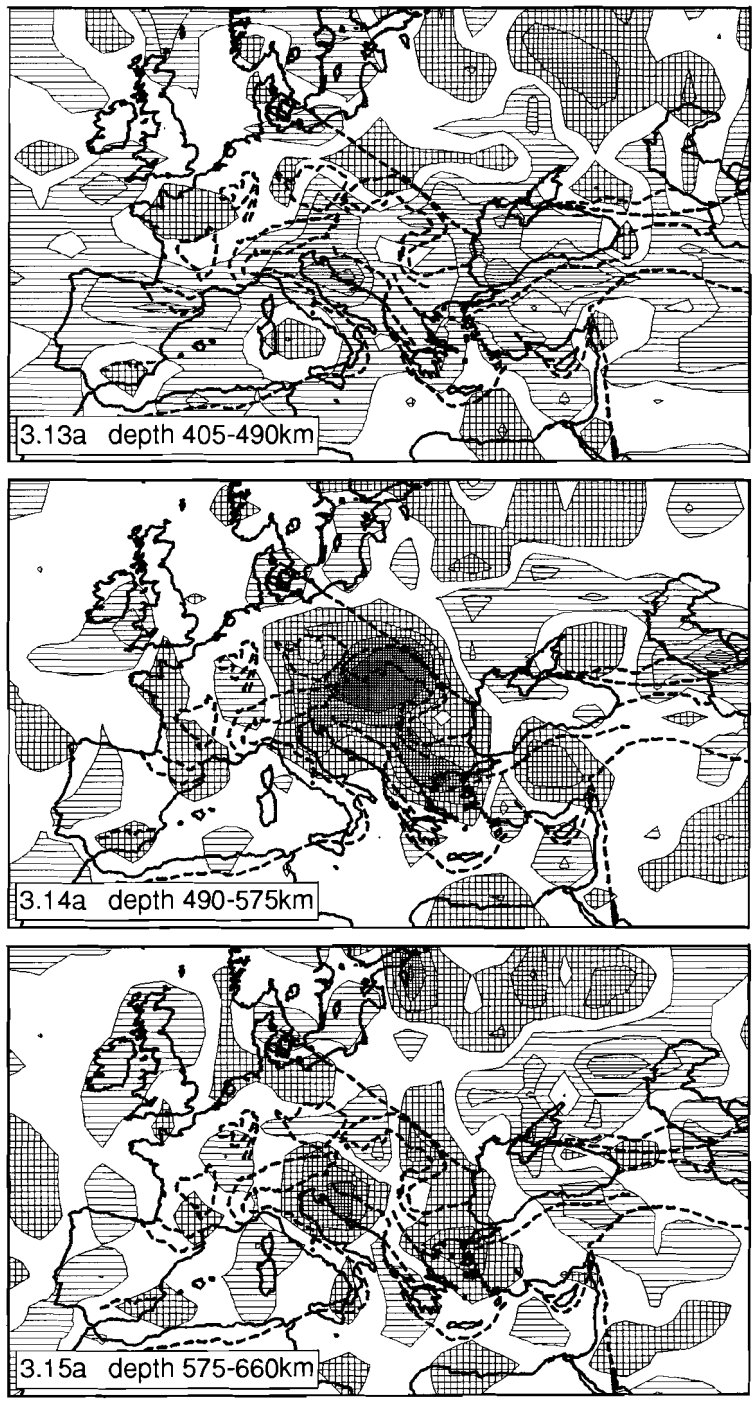
3.13a depth 405-490km
3.14a depth 490-575km
3.15a depth 575-660km
-4%
4%

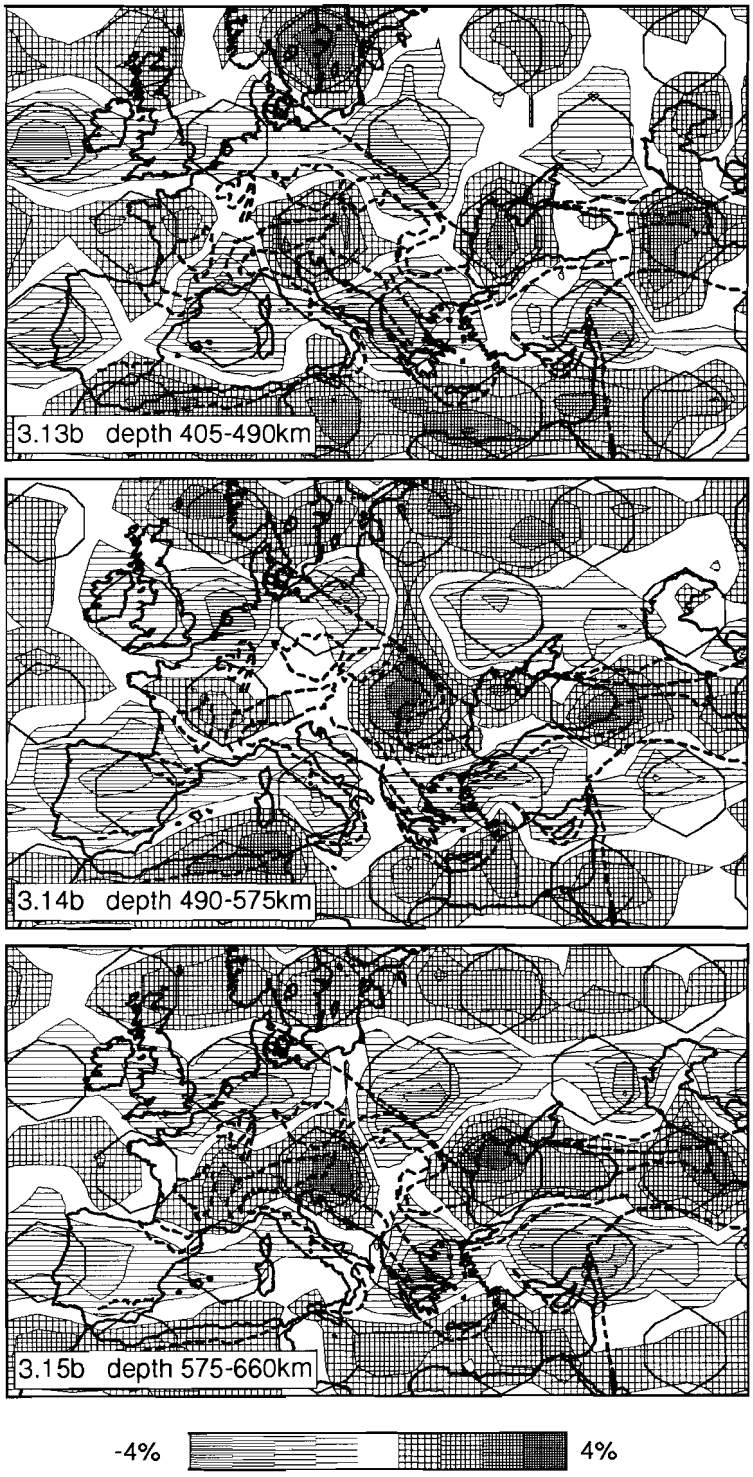
3.13b depth 405-490km
3.14b depth 490-575km
3.15b depth 575-660km
-4%
4%

Spakman (1989), who investigated the influence of the reference model on tomographic images of the aspherical variations in P-wave velocity below the Caribbean region. From figure 3.6a, one might conclude that subduction below Crete stops at 200 km depth, while EURS89B, obtained with an improved reference model, suggests that the African plate subducts at least to 670 km depth, which would be in agreement with the P velocity image (Figure 5.6d). Therefore, we conclude with Van der Hilst and Spakman (1989) that the use of an inadequate reference model may lead to erroneous interpretations.

3.7.2 3-D model

In figures 3.7a-3.15a we show horizontal cross sections through the upper mantle part of the preferred model. Along with each cross section we present the corresponding cross section through the result of the harmonic sensitivity test (figures 3.7b-3.15b). For reference, the outlines of major tectonic features are plotted with dashed lines.

The result of the harmonic sensitivity test shows that the input model is poorly recovered in layer 1 (0-33 km; figures 3.7a,b). According to the ray geometry predicted by the reference model rays arriving beyond 3° bottom below this layer, which is consequently sampled by nearly vertical rays. Hence a relatively small portion of the ray paths sample this layer, which explains the poor resolution. The resolution is good nearly everywhere in central, western and southern Europe in layers 2 and 3 (33-128 km; figures 3.8a,b and 3.9a,b). In layer 2 the anomaly below southern Sweden is mapped incorrectly. In layer 3 the synthetic model is recovered well below southern Sweden and the western boundary of the Russian Platform, indicating a good resolution below these regions. The resolution is somewhat worse in layers 4-6 (128-405 km; figures 3.10a,b, 3.11a,b and 3.12a,b). With the current reference model there are no rays associated to first arrivals that bottom in the depth range encompassed by these layers. Consequently, structure in this depth range is sampled predominantly by nearly vertical rays. In the recovered model the resulting lack of vertical resolution is visible as *leakage* (= smearing in vertical direction) of the anomaly pattern of adjacent layers. This leakage is clearly visible in the recovered model in layer 6, and, in particular, in layer 5. In the input model, the anomaly pattern of adjacent layers is shifted in x-direction (figures 3.5a,b). As a consequence of vertical leakage the inversion response shows an alternation of east-to-west striking zones of positive and negative anomalies rather than the 'checkerboard' pattern of the input model. In layer 7 (405-490 km; figure 3.13a,b) the resolution is good below central and southern Europe and the southwestern boundary of the Baltic Shield/Russian Platform. In layer 8 and 9 (490-660 km; figures 3.14a,b and 3.15a,b) the resolution is somewhat worse. Below southeastern and central Europe the resolution is reasonable, but below western Europe the vertical resolution is poor.

3.8 Concluding remarks

We obtained a 3-D model of S-wave velocity below Europe by a tomographic inversion of the ISC S delays. A regional 1-D reference model was used for the linearization of the

inversion problem. Sensitivity tests with realistic errors indicate that the resolution is reasonable below most parts of Europe.

To avoid contamination of the solution by outliers in the data, we used a simple cut-off criterion for the value of residuals. The preferred model was obtained by inversion of residuals with a maximum absolute value of 6 s with respect to the travel time of the reference model used. It is likely that we rejected accurate readings with this rather small residual window. However, inclusion of delays exceeding the maximum absolute value of 6 s in the inversion requires attention for the following problems. First, inversions of data sets that include residuals with an absolute value larger than 6 s resulted in models in which the average value of the velocity anomalies deviates systematically from zero over certain depth ranges. This suggests small deficiencies of the reference model used. Therefore, the adequacy of the linearization with the current reference model has to be investigated in more detail. Second, to include delays belonging to ray paths that bottom in the high velocity lid of the Baltic Shield and arrive in the epicentral distance range 13°-20° a laterally varying reference model is needed. Third, by inverting S residuals within a larger delay-time window there is an increased danger of contamination of the solution by outliers. A more robust inversion scheme is necessary to avoid this. However, instead of investigating these problems in detail and refining this method we prefer to obtain an S velocity model by inversion of full waveforms with the method of partitioned waveform inversion (Nolet, 1990). In this method, linearization with respect to the reference model plays a less important role.

Chapter 4

3-D structure from Rayleigh-wave phase velocity data

4.1 Introduction

By now, a large number of phase velocity measurements between stations in western Europe is available, and it seems timely to attempt modelling these data using state-of-the-art tomographic techniques. Panza et al. (1980) combined the then available long period phase velocity data to obtain a model of S velocity and lithosphere thickness below Europe. The same data set was used by Yanovskaya et al. (1990) who constructed two-dimensional phase velocity maps at different periods using a method based on the Backus-Gilbert approach. In this study we wanted to obtain a model of the S wave velocity directly.

Following common practice in body wave tomography (e.g., Spakman and Nolet, 1988) we parameterized the upper mantle with discrete cells without any a priori regionalization, and we inverted an augmented data set. Our aim was to find the smoothest model that fits the data while giving an acceptable misfit, and to determine the degree of detail in this model that can be resolved by the data set.

4.2 Method

Figure 4.1 shows the wave paths included in our data set. We augmented the data set used by Panza et al. (1980) with profiles across the Baltic Shield (Calcagnile and Panza, 1978; Noponen, 1966), the British Isles and North Sea (Clark and Stuart, 1981; Stuart, 1978), the Balkan (Calcagnile et al., 1984; Papazachos, 1969), the Pyrenees (Souriau and

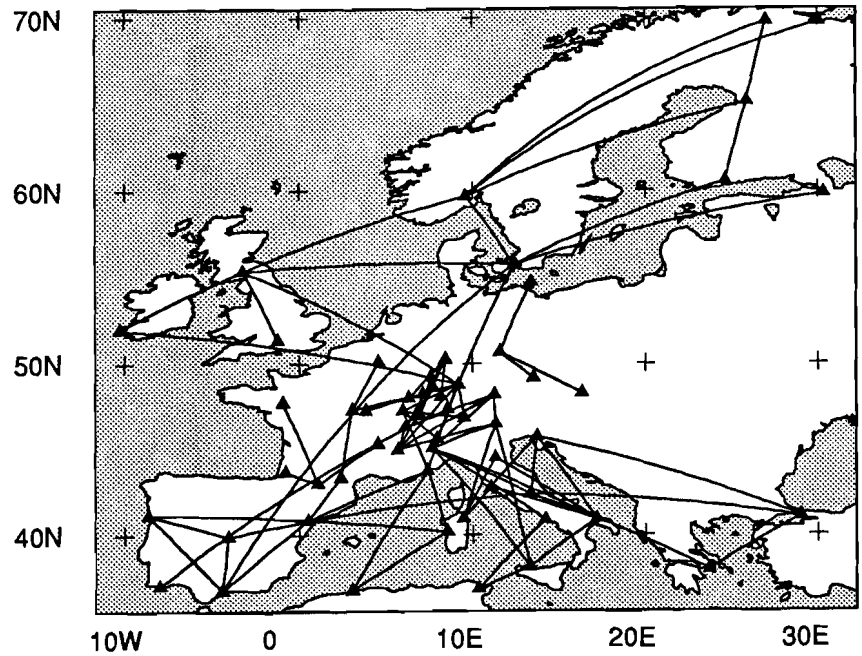

Figure 4.1. Wave paths of which phase velocity data were used.

Vadell, 1980), and Czechoslowakia (Neunhofer et al., 1981; Neunhofer et al., 1983). For the inversion we selected phase velocities for the periods 25, 50 and 80 s. Phase velocities for these three periods are most sensitive to the S velocity in the depth ranges (0-60 km), (50-110), (70-180 km) respectively. We subtracted phase velocities calculated from a modified PREM model (Dziewonski and Anderson, 1981) from the data and inverted for velocity perturbations relative to this model. The upper mantle was parameterized with a grid of discrete cells. We assumed a linearized relationship between model **m** and phase velocity deviations δc. We aimed at minimizing a weighted sum of model misfit and gradient of the model:

$$|\mathbf{Gm}-\delta\mathbf{c}|^2 + \lambda\int|\nabla\mathbf{m}|^2 dv = \min$$

Following Nolet (1987a) we regarded this as the minimisation problem belonging to the linear system:

$$\begin{bmatrix}\mathbf{G}\\ \mathbf{D}\end{bmatrix}\begin{bmatrix}\mathbf{m}\end{bmatrix} = \begin{bmatrix}\delta\mathbf{c}\\ \mathbf{0}\end{bmatrix}$$

where **D** is the damping matrix which uses finite differences to yield the gradient of **m**. Allowing for different weights λ_h and λ_v for horizontal and vertical derivatives, the

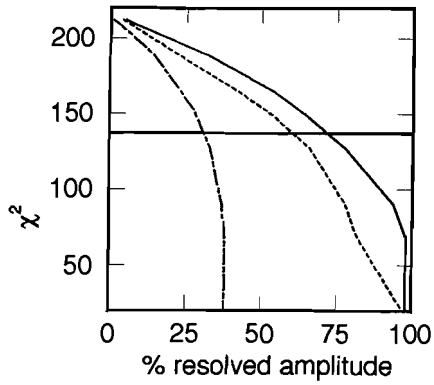

Figure 4.2. χ^2 versus resolved amplitude (in %) for three synthetic tests on different cells in the second layer: a well constrained cell below the Alps (solid line), a reasonably constrained cell below southern Spain (dotted), and a cell below Scandinavia which is sampled by three almost parallel profiles (dash-dotted). The line indicates the value of χ^2 and resolved anomalies for the chosen damping parameter.

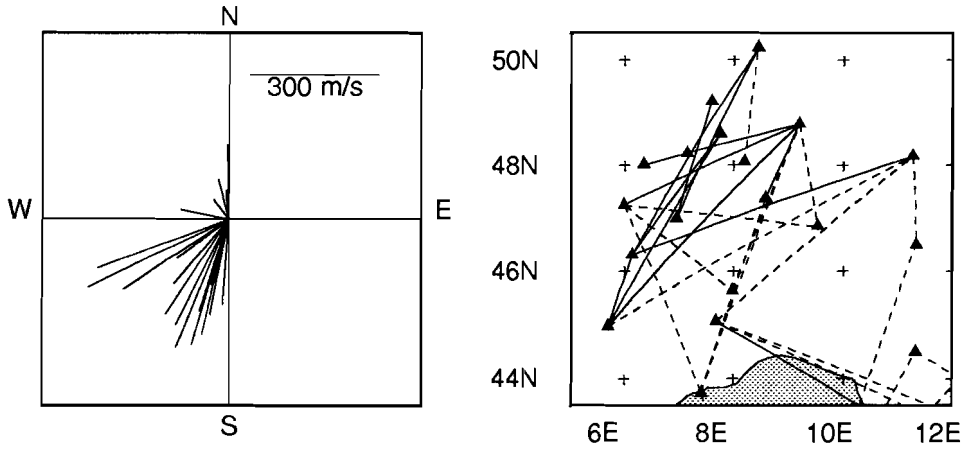

Figure 4.3. a) Phase velocities (minus 3.5 km/s) for periods of 25 s plotted in direction of wave-path azimuth for the area between 5E and 11.5E, 43.6N and 50.5N. b) Locations of wave paths used in figure 3a, solid line: wave paths with phase velocities higher than average for the area, dashed line: wave paths with phase velocities lower than average for the area.

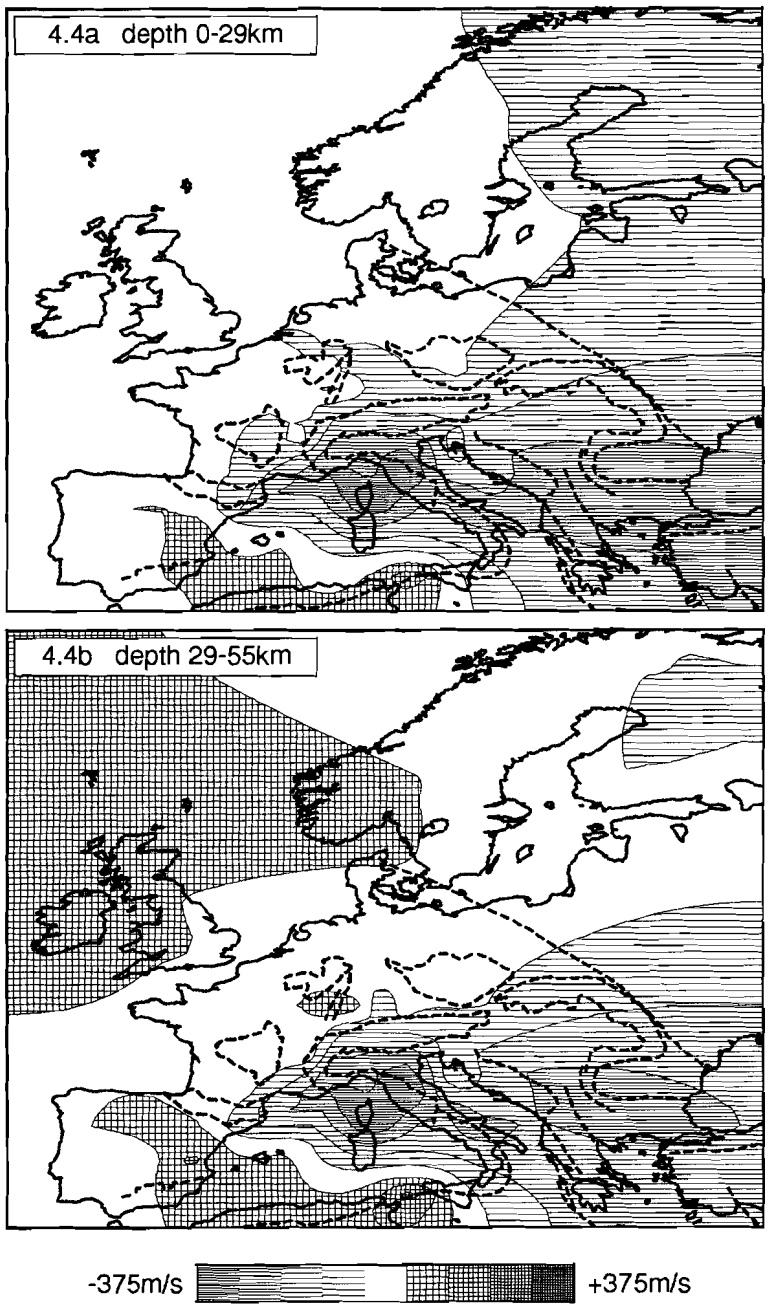

Figure 4.4. S velocity perturbations of the final solution. a) depth 0-29 km; reference velocity 3.48 km/s. b) depth 29-55 km; reference velocity 4.41 km/s.

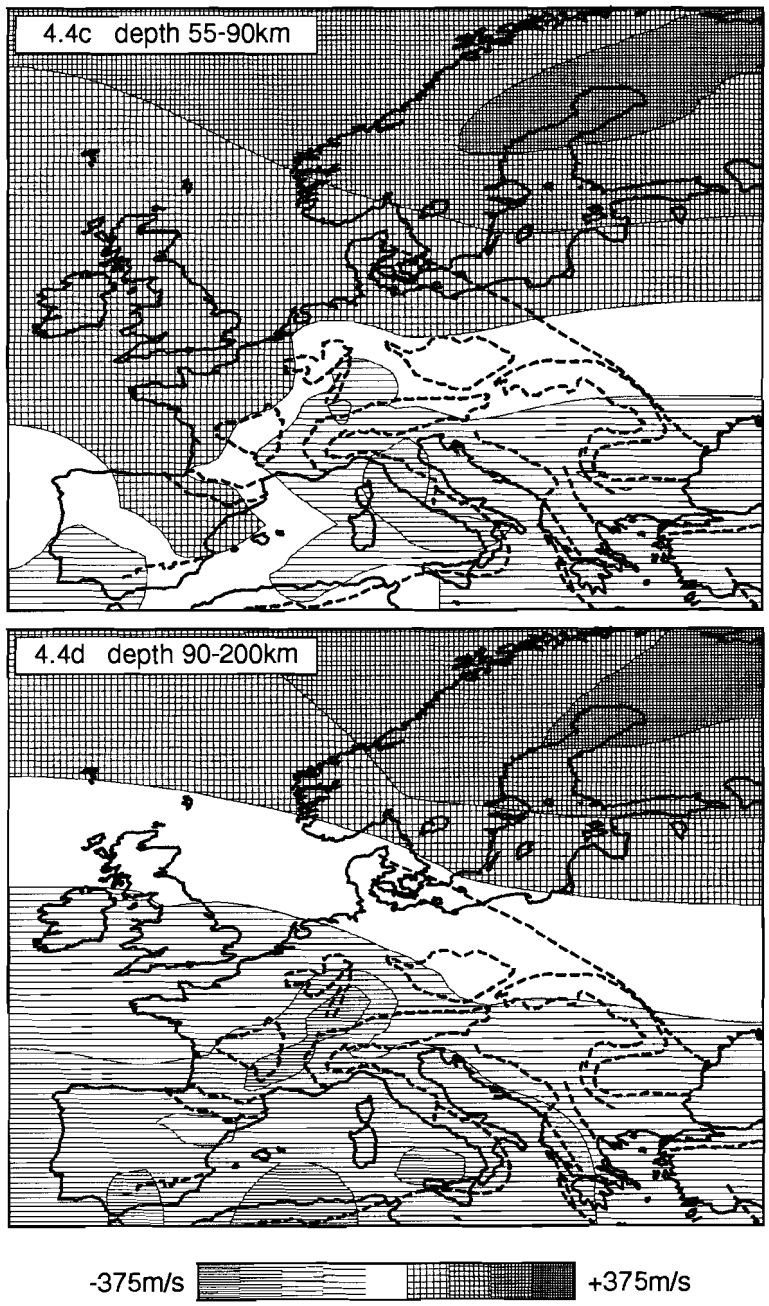

Figure 4.4 (continued). S velocity perturbations of the final solution. c) depth 55-90 km; reference velocity 4.5 km/s. d) depth 90-200km; reference velocity 4.5 km/s.

damping matrix **D** consists of three matrices $\mathbf{D}_r$, $\mathbf{D}_\phi$ and $\mathbf{D}_\theta$ which yield the first derivative in the r, ϕ and θ direction:

$$\left[\mathbf{D}\right] = \begin{bmatrix} \lambda_v \mathbf{D}_r \\ \lambda_h \mathbf{D}_\phi \\ \lambda_h \mathbf{D}_\theta \end{bmatrix}$$

In the inversions we virtually applied only regularization in the horizontal directions by assigning a very low value to λ_v. The system was solved with the LSQR algorithm (Paige and Saunders, 1982).

The choice of the weight to assign to damping is usually ad hoc. We tried to determine the weight for the damping in a more quantitative way. For various damping parameters λ_h we performed two synthetic tests. First, a data vector consisting of random, normally distributed noise with a standard deviation σ was inverted. As a measure of the misfit we calculated $\chi^2 = \sum_i (\delta c_i - G_{ij} m_j)^2/\sigma^2$. Second, we calculated a data vector from a synthetic model with only one anomalous cell (spike). Applying the same damping as in the first test this data vector was inverted and we estimated the percentage of the original amplitude that was resolved. After having performed the two tests for different damping parameters we constructed a curve (figure 4.2) of χ^2 versus resolved amplitude. According to theory, one should aim for χ^2 to be equal to the degrees of freedom of the problem after a random Gaussian noise inversion. There are $n-k$ degrees of freedom, with n the number of data and k the number of model parameters. It is not clear to us what k should be in this problem. Many cells are not sampled by profiles or otherwise not resolved and damping affects the effective rank of the system, so it is not correct to take k as the number of cells in the grids. Since the data vector δc influences the directions of search of LSQR it would be incorrect to use the number of iterations of LSQR as number of degrees of freedom. We therefore chose the appropriate value of the damping parameter on the basis of two criteria:
- damping should take care that the level of noise which propagates in the solution is as low as possible.
- damping should, on the other hand, not suppress too much the amplitude of the spike.
We thus tried to determine a value of χ^2 that is neither too high nor too low on the basis of the results of our synthetic tests. The combination of these criteria leads to a choice of damping parameter associated to a point near the inflection point of the curve. However, the character of the curve depends strongly on how well the particular the spike is constrained by the data. We therefore performed the tests for a few cells with different resolvability (see figure 4.2), and chose the value for the damping parameter λ_h on the basis of the curves for these cells.

4.3 Azimuthal anisotropy ?

Since the wave path coverage is high in the Alps, we checked if there is evidence for azimuthal anisotropy from the data which belong to wave paths in the area between 5E and 11.5E, 43.6N and 50.5N. A diagram of phase velocities for periods of 25 s plotted in

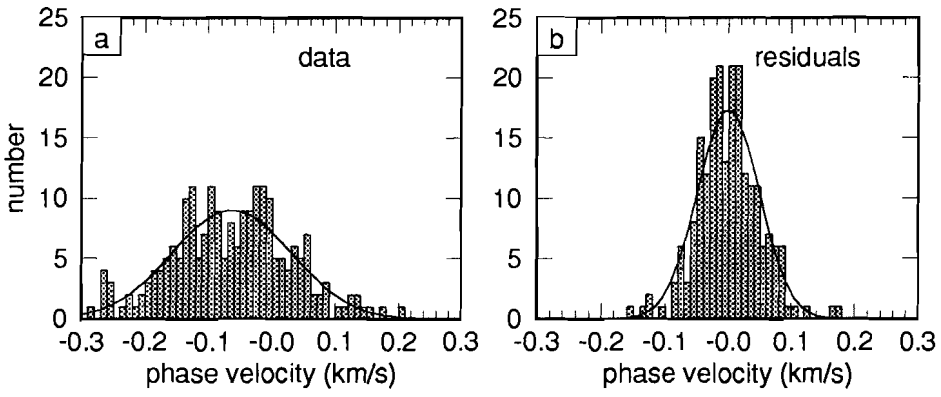

Figure 4.5. a) Histogram of phase velocity data (relative to reference phase velocities), standard deviation is equal to 0.93 km/s. b) Histogram of residuals after inversion, standard deviation is 0.049 km/s.

direction of azimuth of the wave path (fig 3a) suggests that phase velocities are higher in the NE-SW direction than in northwestern direction. Figure 4.3b shows the actual locations of the wave paths with indications if phase velocities are higher (solid line) or lower (dashed line) than the average value of the wave paths in this region. The map shows that the dependence of the values on direction of the values can be explained by the presence of a high velocity zone in the northwestern Alps, which is sampled by most northeast-southwest paths, and low velocities in the southern Alps. We checked similar diagrams for the periods of 50 and 80 s but didn't find azimuthal dependence of the phase velocities that could not be explained by the location of the wave paths and lateral heterogeneity. Although anisotropy is not ruled out by these observations, it is not needed to explain the data.

4.4 Results

In figure 4.4a-4.4d we show the final model. The cell grid is divided in four layers with different thickness. The horizontal dimensions of the cells are $1° \times 1°$. Since the data set consisted of phase velocities for three different periods, not more than three layers can be resolved. This is visible in the solution. Phase velocities for periods of 25 s are nearly equally sensitive to S velocities in both layers, while phase velocities of periods of 50 and 80 s are much less influenced by the S velocity at these depths. Therefore, the solution in the first (0-29 km) and second layer (29-55 km) is almost identical. Figure 4.5a and 4.5b show the histograms of the phase velocity data and the residuals after inversion. The standard deviation of the data is 0.093 km/s, the standard deviation of the residuals after inversion is 0.050 km/s. There is no regional bias in the values of the residuals.

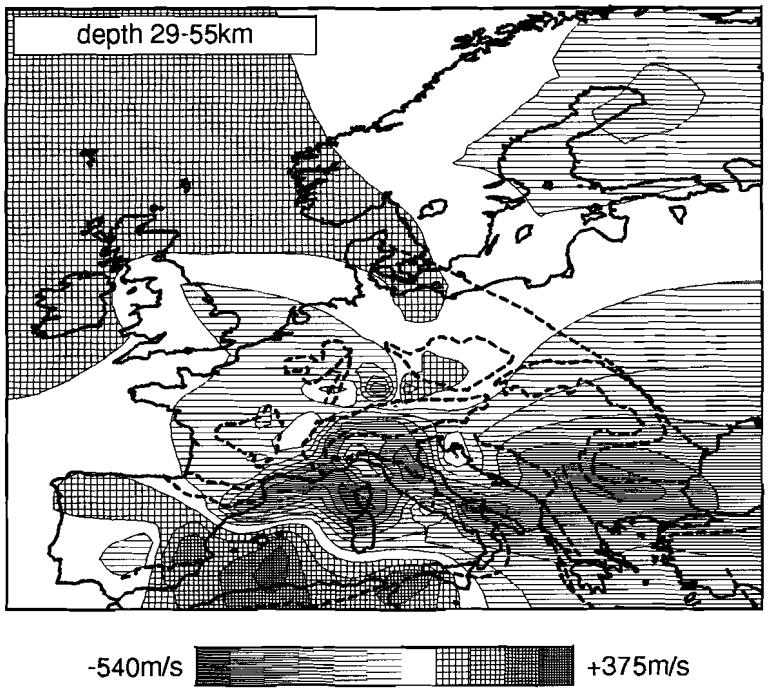

Figure 4.6. S velocity perturbations of a model which gives a residual distribution with a standard deviation of 0.03 km/s, depth: 29-55 km. (Note that the contouring scale differs from figure 4.4)

We also performed an inversion which resulted in a residual distribution with a much smaller standard deviation of 0.03 km/s. This was achieved by lowering the values of the damping parameters. Figure 4.6 shows the second layer of this model. Especially in the region with dense profile coverage this model has much more detail and amplitudes of anomalies as large as 0.5 km/s, which must probably be considered unrealistic. Therefore, we prefer the smooth model presented in figure 4.4.

The velocity perturbations are calculated relative to a continental model with a crustal thickness of 29 km. The reference velocity is given in the figure captions. The model is not constrained by data on the Russian platform and the Atlantic ocean. The gradient damping causes the solution to be interpolated between the profiles bordering on these regions. At depths corresponding to the lower lithosphere and LVZ (55-200 km, figure 4.4d), the model shows high velocities below the Baltic shield and low velocities below Variscan and Alpine areas. A prominent feature of the model is the low velocity anomaly below the Ligurian Sea and north and central Italy at depths between 0 and 55 km (figure 4.4a, 4.4b). The anomaly was reported by Panza et al. (1982), using phase velocity data which are part of

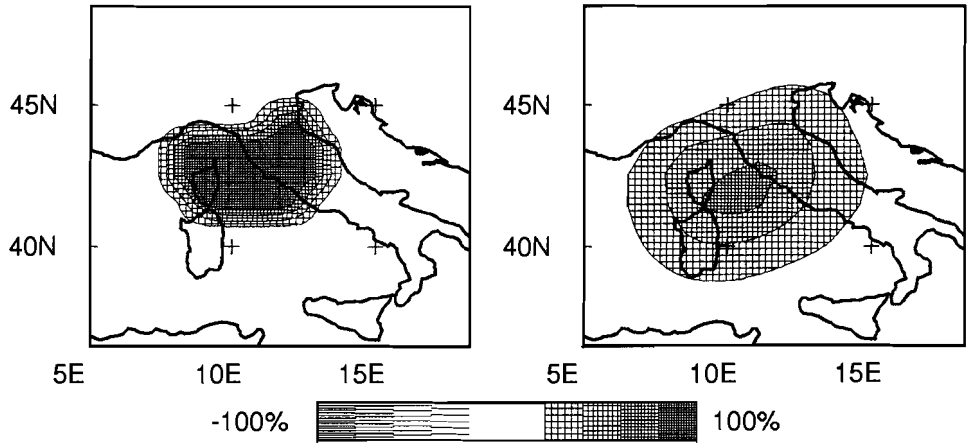

Figure 4.7. Sensitivity test for the Ligurian Sea, depth 29-55 km. a) input model, b) recovered model.

this data set. Snieder (1988), who inverted fundamental mode Rayleigh waveforms recorded at the NARS array using surface wave scattering theory, also found a low velocity anomaly below this region. A spike test indicates that the anomaly is well resolved (figure 4.7). Between 0 and 55 km a high velocity anomaly is present below the northwestern Alps. Spike tests show that this anomaly is well resolved. The Balkan region has low velocities at all depths. In the deepest layer a low velocity anomaly suggestively links the Bresse Graben, which is the northern part of the Rhone valley, and the Rhine Graben. This is not an artifact caused by smearing of the anomaly in the southwestern direction (figure 4.8). However, the extent of the anomaly is not well constrained to the north and to the west, because the wave path coverage is poor in those directions. The presence of the anomaly is supports the idea of a common origin of the Rhine Graben and the Bresse Graben, as was revealed from geological evidence (Illies ,1974; Laubscher, 1970). Details of the relationship between the grabens, which are not well known, are not resolved with our method.

4.5 Crustal corrections

The shear velocity model was computed from the phase velocity data assuming a crustal thickness of 29 km. However, phase velocities are sensitive to structures in the mantle and crust, and therefore, variations in crustal thickness affect the phase velocities and thus influence the retrieved shear velocity at mantle depths. Modes are not very sensitive to the precise depth of discontinuities but rather measure the average velocity over a certain depth range. We used this to correct the shear velocity model for variations in crustal thickness. We assembled information about crustal velocities and Moho depth from

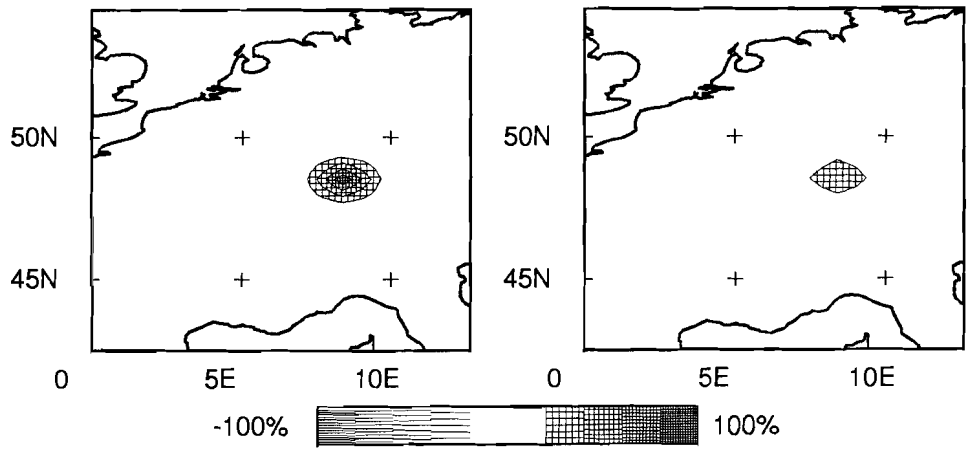

Figure 4.8. Sensitivity test for the Rhine Graben region, depth 90-200 km.
a) input model, b) recovered model. Although the amplitude of the spike is not well resolved, the recovered anomaly is not distorted in the direction of the Bresse Graben.

different sources (Henkel et al., 1990; Mostaanpour, 1984; the Moho map compiled by Giese and Mostaanpour (Giese, pers. comm.) and the following maps from the Geothermal Atlas of Europe: Depth of the Crust-Mantle Boundary, Average Velocities in the Consolidated Crust, Thickness of the Undeformed Sedimentary Cover). Under the condition that locally the average velocity over crust and mantle remains the same, we corrected the retrieved mantle velocity using the known value for Moho depth and crustal velocity. We assumed that the retrieved shear velocity of the deepest layer (90-200 km) is predominantly determined by phase velocities of the fundamental mode at 80 s, which is relatively insensitive to the Moho depth. Therefore, we corrected the velocity in the upper mantle above 90 km depth. The corrections to the velocity perturbations increase linearly from 0 at 90 km to maximum at the local Moho depth. We checked if, locally, the corrected velocity model indeed yielded, within measurement errors of phase velocities, the same phase velocity as the uncorrected model. If necessary, we adjusted the mantle velocity so that this condition was met. The corrected velocity perturbations in layer 2 and 3 are shown in figures 4.9a and 4.9b. The grey areas are the regions below which the model is not constrained by data. Because crustal corrections gave meaningless velocity perturbations in these regions, they were colored grey.

Figure 4.9 (opposite page). S velocity perturbations after crustal corrections. Below the grey areas the model is not constrained by data, and the crustal corrections resulted in meaningless velocity perturbations. a) Moho depth - 55 km, reference velocity 4.41 km/s, b) depth 55-90 km, reference velocity 4.5 km/s.

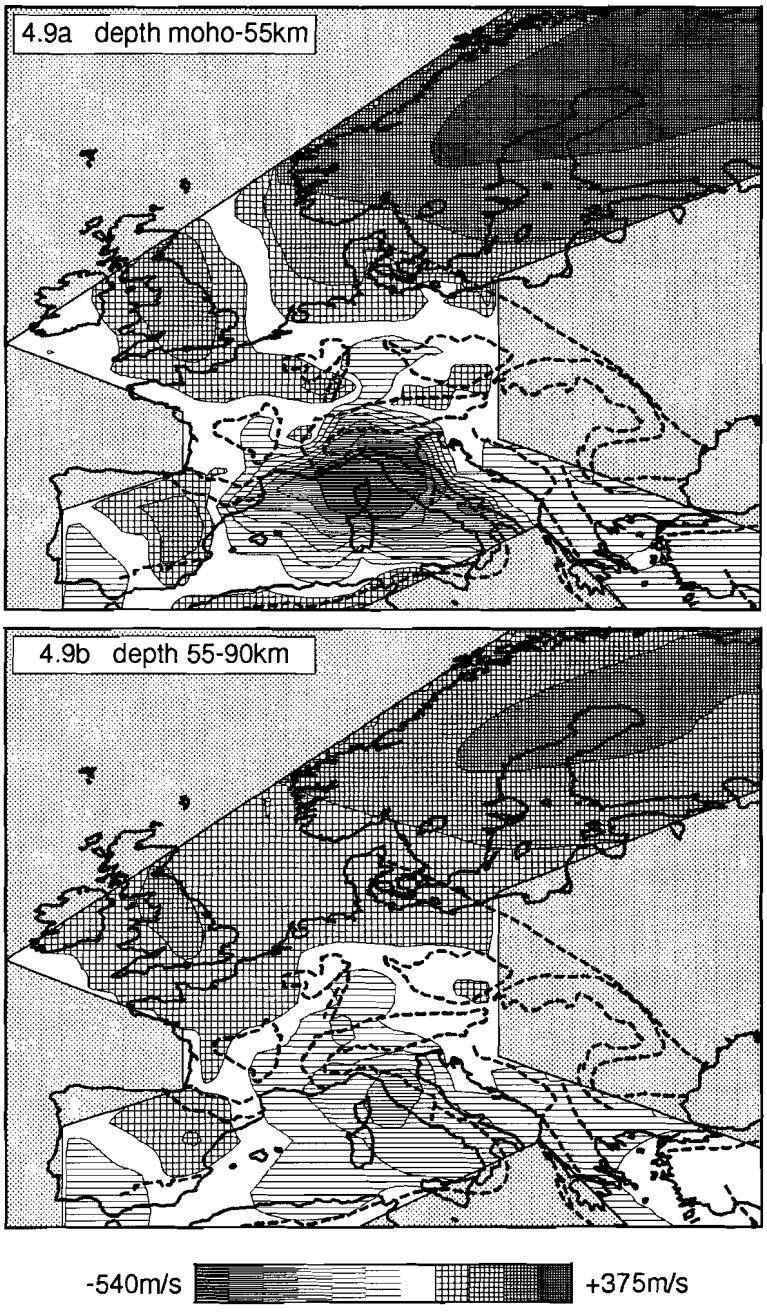
4.9a depth moho-55km
4.9b depth 55-90km
-540m/s
+375m/s

Compared to the uncorrected model the Baltic Shield has higher velocities below the Moho. Also England and the eastern part of the Iberian Peninsula are characterized by higher sub-Moho velocities. The low velocity anomaly below the Ligurian Sea and northern and central Italy has become very strong. There are high sub-Moho velocities below the Western Alps.

We realize that there are drawbacks of this method to apply crustal corrections. First, we are not confident that the information about the crustal thickness and velocity is everywhere correct because different sources give inconsistent information. Furthermore, there are gaps in our information, for instance about the crustal velocity in the western Mediterranean, the parts of Baltic Shield and eastern Europe, so in many regions we had to interpolate over large distances. Secondly, because of lack of resolution, the anomalies in the upper layer of the uncorrected model do not represent the true crustal velocity (or an average of the velocity in the upper 29 km of the Earth) in many regions. Applying corrections for crustal velocity and thickness may thus lead to an overcorrected model or wrongly corrected model. Finally, there appear features in the corrected anomaly pattern that are not resolved by the data set. An example is the outline of the North Sea graben. Therefore, we strongly emphasize that the corrected model is one, possible, interpretation of the phase velocity data set.

4.6 Conclusions

Inversion of the available phase velocity data in Europe has been interpreted in terms of a smooth model, which gives a residual distribution with a standard deviation of 0.05 km/s. The solution shows high velocities below the Baltic shield and relatively low velocities below the Alpine and Variscan regions. The most striking features of the model are a strong low velocity anomaly below the Ligurian Sea and parts of north and central Italy between 0 and 55 km depth, and a deep low velocity anomaly beneath the Bresse Graben and the Rhine Graben.

Chapter 5

Partitioned waveform inversion: theory

5.1 Introduction

In the previous chapters we described two studies in which different data sets were inverted for a model of the S wave velocity below Europe. In chapter 3 we described the linearized inversion of S delay times reported by the ISC with the method of delay time inversion as developed by Spakman and Nolet (1988). We recognized two major problems with the application of this method to ISC S delays. Firstly, there is a danger that the basic assumption that all ray paths can be calculated accurately enough with a 1-D reference model is violated because lateral heterogeneity is larger for S waves than for P waves (Paulssen, 1987). Secondly, these data can have large errors, which yields a high risk at contamination of the solution by data with large errors. A general shortcoming of the method of delay time tomography is that only structures in regions with a high density of stations and earthquakes can be resolved well. In regions with many stations but without seismic activity incoming waves travel along nearly vertical rays so the depth resolution is poor. With the inversion of phase velocity measurements of fundamental mode Rayleigh waves, as described in the previous chapter, structures in these regions can be resolved. With the data set that we used, consisting of phase velocity measurements for periods less than 80 s, only structures shallower than approximately 200 km depth can be resolved. In the remaining part of this thesis we apply a method with which the shortcomings of the above mentioned studies can largely be overcome.

The method of partitioned waveform inversion, as developed by Nolet et al. (1986a) and Nolet (1990), makes it possible to invert a large set of waveform data of body waves and surface waves for a 3-D velocity model. The inversion is a step-wise procedure. In the first step, the time window of a seismogram containing the S or SS wave - depending on distance - up to the fundamental mode of the Rayleigh wave is fitted in a non-linear inversion. The results of this non-linear inversion are linear constraints on the velocity at the source-receiver path. The non-linear waveform inversion is repeated for many seismograms belonging to crossing paths. In this way, a large set of linear constraints on the velocity along the different paths is assembled. The second step is to combine all linear constraints in a linear inversion for a 3-D velocity model.

The basic assumption underlying partitioned waveform inversion is that a seismogram is only influenced by Earth's structure in a clearly defined region. The specific theory applied to construct the synthetic seismogram determines the extent of this region. It can be, as in this study, the (infinitesimally narrow) vertical plane through the source-receiver minor arc. Or, if scattering is taken into account, a finite region around this plane. The non-linear inversion of a seismogram is, under this assumption, reduced to a problem with a small number of variables, that can be solved without too much computational effort. The method is called "partitioned" because the waveform inversion step is separate from the linear inversion of all constraints that results in a tomographic image. The theory has been described by Nolet (1990) and Nolet (1992) and is summarized here for the sake of completeness.

5.2 Partitioned waveform inversion

In waveform inversion, the aim is to predict an observed time series $d(t)$ as accurately as possible with a synthetic seismogram $s(t,\mathbf{p})$, $\mathbf{p}$ being a vector with elements the parameters that are to be varied in the Earth model. Generally, the inverse problem can be stated as finding the "model" $\mathbf{p}$ that gives the minimum of the "penalty function" $F(\mathbf{p})$:

$$F(\mathbf{p}) = \int [Rd(t) - Rs(t,\mathbf{p})]^2 dt + \mathbf{p}^T \mathbf{C}_p^{-1} \mathbf{p} \qquad (1)$$

R is an operator that selects the time window to be fitted and filters it to the frequency band of interest. In general, this problem is ill-stated because F is insensitive to some parameters or because there are trade-offs between two or more parameters. In order to constrain unresolved parameters we bring in a priori information in the form of a damping term $\mathbf{p}^T \mathbf{C}^{-1} \mathbf{p}$ added to the r.h.s of (1), where $\mathbf{C}$ is the a priori covariance matrix of the

The question is how to construct the synthetic seismogram $s(t,\mathbf{p})$, and which parameters are selected to be varied in the Earth model. In partitioned waveform inversion, the basic assumption is that the seismogram is only influenced by the properties of the Earth in a clearly defined region. Nolet (1990) constructs the time window of a seismogram containing the S wave up to the fundamental mode of the Rayleigh wave as a sum of higher modes of surface waves. For a laterally homogeneous Earth model, the spectrum $S_j(\omega)$ of the seismic signal in a station at epicentral distance Δ_j is:

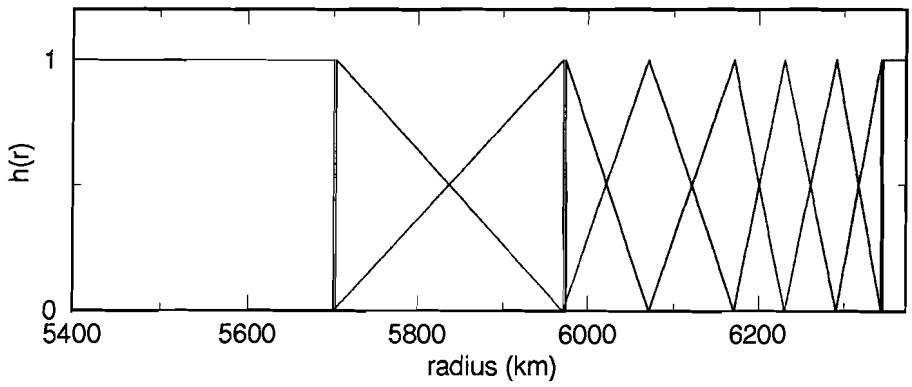

Figure 5.1. An example of a set of basis functions $h_i(r)$. The triangular shaped functions interpolate linearly between support points. The boxcar functions at both ends model a constant velocity perturbation.

$$S_j(\omega) = \sum_{n=0}^{\infty} A_{nj}^0(\omega)\exp\left[ik_n^0(\omega)\Delta_j\right] \tag{2}$$

where $A_{nj}^0(\omega)$ is the excitation coefficient for mode number n, $k_n^0(\omega)$ the wave number at circle frequency ω. The superscript "0" indicates that these quantities are calculated for a laterally homogeneous (starting) model. Deviations from lateral homogeneity will perturb the phase factor $k_n^0(\omega)\Delta_j$. Neglecting effects such as backscattering the perturbed phase factor is modelled with a phase integral approximation:

$$k_n^0(\omega)\Delta_j \rightarrow \int_{P_j} k_n\,[\theta(\Delta),\phi(\Delta);\omega]d\,\Delta \tag{3}$$

θ and ϕ are the colatitude and longitude along the surface ray path. $k_n(\theta,\phi;\omega)$ is the local wavenumber, i.e. it represents the dispersion of this mode in a hypothetically laterally homogeneous Earth with the properties found in the heterogeneous Earth along the radius pointing in the direction of (θ,ϕ). P_j denotes that integration is along the path j. To a certain extent we correct for the perturbation in the excitation coefficient due to lateral heterogeneity: we use different models (continental or oceanic) for the source- and receiver structure if this is appropriate. The spectrum is now written as:

$$S_j(\omega) = \sum_{n=0}^{\infty} A_{nj}^0(\omega)\exp\left[i\int_0^{\Delta_j} k_n\,[\theta(\Delta),\phi(\Delta);\omega]d\,\Delta\right] \tag{4}$$

Since only S body waves and Rayleigh waves are modelled, it is assumed that perturbations in the phase integral are caused by perturbations $\delta\beta(\mathbf{r})$ in the S-wave velocity of the starting model $\beta^0(r)$. The phase integral is then approximated by:

$$\int_{P_j} k_n[\theta(\Delta),\phi(\Delta);\omega]d\Delta = k_n^0(\omega)\Delta_j + \int_{P_j}\int_0^a \left[\frac{\partial k_n(\omega)}{\partial\beta(r)}\right]\delta\beta(\mathbf{r})\,dr d\Delta$$

$$= k_n^0(\omega)\Delta_j + \int_0^a \left[\frac{\partial k_n(\omega)}{\partial\beta(r)}\right]\int_{P_j}\delta\beta(\mathbf{r})d\Delta\,dr \qquad (5)$$

The Frechet derivatives $\partial k_n/\partial\beta$ are given by, e. g. , Takeuchi and Saito (1972). The factor $\int_{P_j}\delta\beta(\mathbf{r})d\Delta$ is, apart from a factor Δ_j^{-1}, the average one-dimensional (1-D) velocity-depth function along the path. We develop this velocity function in a set of basis functions $h_i(r)$, i=1,...N:

$$\frac{1}{\Delta_j}\int_{P_j}\delta\beta(\mathbf{r})d\Delta = \sum_i^N \gamma_i^j h_i(r) \qquad (6)$$

For the basis functions $h_i(r)$ we take boxcar- and triangular shaped functions (see figure 5.1). The last term of the r.h.s. of equation 5 then becomes:

$$\int_0^a \left[\frac{\partial k_n(\omega)}{\partial\beta(r)}\right]\int_{P_j}\delta\beta(\mathbf{r})d\Delta\,dr = \sum_{i=1}^N \gamma_i^j \int_{P_j}\int_0^a \left[\frac{\partial k_n(\omega)}{\partial\beta(r)}\right]h_i(r)\,dr d\Delta \qquad (7)$$

With

$$h_i(\omega) = \int_0^a \left[\frac{\partial k_n(\omega)}{\partial\beta(r)}\right]h_i(r)dr \qquad (8)$$

we find for the spectrum:

$$S_j(\omega) = \sum_{n=0}^{\infty} A_{nj}^0(\omega)\exp\left[i\Delta_j\,[k_n^0(\omega)+\sum_i \gamma_i h_i(\omega)]\right] \qquad (9)$$

The synthetic seismogram is constructed as the Fourier-transform of this spectrum. Note that in the expression for the spectrum $A_{nj}^0(\omega)$ and $k_n^0(\omega)$ are determined by the choice of the starting model and the $h_i(\omega)$ are determined by the choice of basis functions $h_i(r)$. The γ_i^j, which are the path integrals of the velocity, are the parameters to be determined in the inversion. The synthetic seismogram s_j is thus a non-linear function of the path integrals: $s_j = s_j(t,\gamma)$, γ is the vector with elements γ_i^j.

The penalty function F of (1) can now be formulated as a non-linear function of γ:

$$F(\gamma) = \int[Rd_j(t) - Rs_j(t,\gamma)]^2 dt + \gamma^T \mathbf{C}_\gamma^{-1}\gamma \qquad (10)$$

The minimum of $F(\gamma)$ is found with methods of non-linear optimization. Nolet et al. (1986a) and Nolet (1987b) have described this iterative procedure in detail. As already mentioned, R is an operator that selects the time window to be fitted and filters it to the frequency band of interest. In the search for the global minimum of F, R plays a role in

avoiding convergence to local minima. In early iterations, F is minimized with a strong low pass filter in R. In each next iteration, higher frequencies are added to the signal and the search for the minimum of the changed F starts from the end point of the last iteration. Furthermore, in order to prevent that wave trains with large amplitudes dominate the properties of $F(\gamma)$, R can be designed as a time-varying weighting function that equalizes or otherwise modifies the energy of the wave groups to be fitted. In principle, we use R to select separate time windows for the fundamental mode and the body waves. This makes it possible to fit the surface waves and body waves for different frequency bands, which is important because the effect of scattering becomes significant at lower frequencies for the

Once γ_{opt}, the model for which the object function F has its global minimum, is found we have estimates of the integrals over the velocity $\beta(r)$ along the path j (weighted with the functions $h_i(r)$). In the next section we shall see how these can be transformed into a

5.3 Transformation of the path integrals into independent linear constraints

The non-linear waveform inversion described in the last section results in values for the integral of the velocity along the source-receiver path. If many seismograms belonging to criss crossing paths are fitted, we assemble a large set of values for the path integrals of the velocity. These can be used together as data in a linear inversion for the 3-D velocity.

We must realize, however, that the γ_i have errors which are in general strongly correlated. Although we have found, through the non-linear inversion, a γ_{opt} that gives a good fit of the synthetic to the observed seismogram, there is always a range of values for γ around γ_{opt} that also give an (acceptably) good fit. We define this region by the region of all γ for which the value of the misfit function $F(\gamma)$ is less than $F(\gamma_{opt})+\varepsilon$. The value of ε is determined for each seismogram by constructing synthetics for small deviations $\Delta\gamma$ away from γ_{opt} and deciding subjectively which is the maximum value of $F(\gamma)$ that gives an acceptable fit. This region determines the uncertainty in the solution γ_{opt}. It is necessary to determine a set of parameters with uncorrelated errors. Otherwise we might not only be too optimistic about the errors in the data, but also end up with a set of incompatible data for the 3-D velocity model $\beta(r)$. Nolet (1992) gives an example of a situation in which errors are correlated, and which shows the necessity for determining independent parameters. Suppose the basis $h_i(r)$ are boxcar functions, so they represent a system of layers. Then γ_i is the integral of the velocity in the layer where $h_i(r)$ is equal to 1. For surface waves, it is likely that the average velocity over two layers (say $\gamma_1+\gamma_2$) is determined much more accurately than the velocity contrast between the two layers $\gamma_1-\gamma_2$. This situation is sketched in figure 5.2, where F is sketched as a function of these two parameters. If we accept a certain misfit level $F(\gamma_{opt})+\varepsilon$, we might assign uncertainties $\delta\gamma_1$ and $\delta\gamma_2$ to these parameters. In figure 5.3, the coordinate frame is rotated along the axis of the ellipse denoted by $F=F_{opt}+\varepsilon$. The new coordinates $\eta_1=\gamma_1+\gamma_2$ and $\eta_2=\gamma_1-\gamma_2$ have widely varying uncertainties. Because they are orientated along the major axes of the ellipse, errors in η_1 and η_2 are uncorrelated.

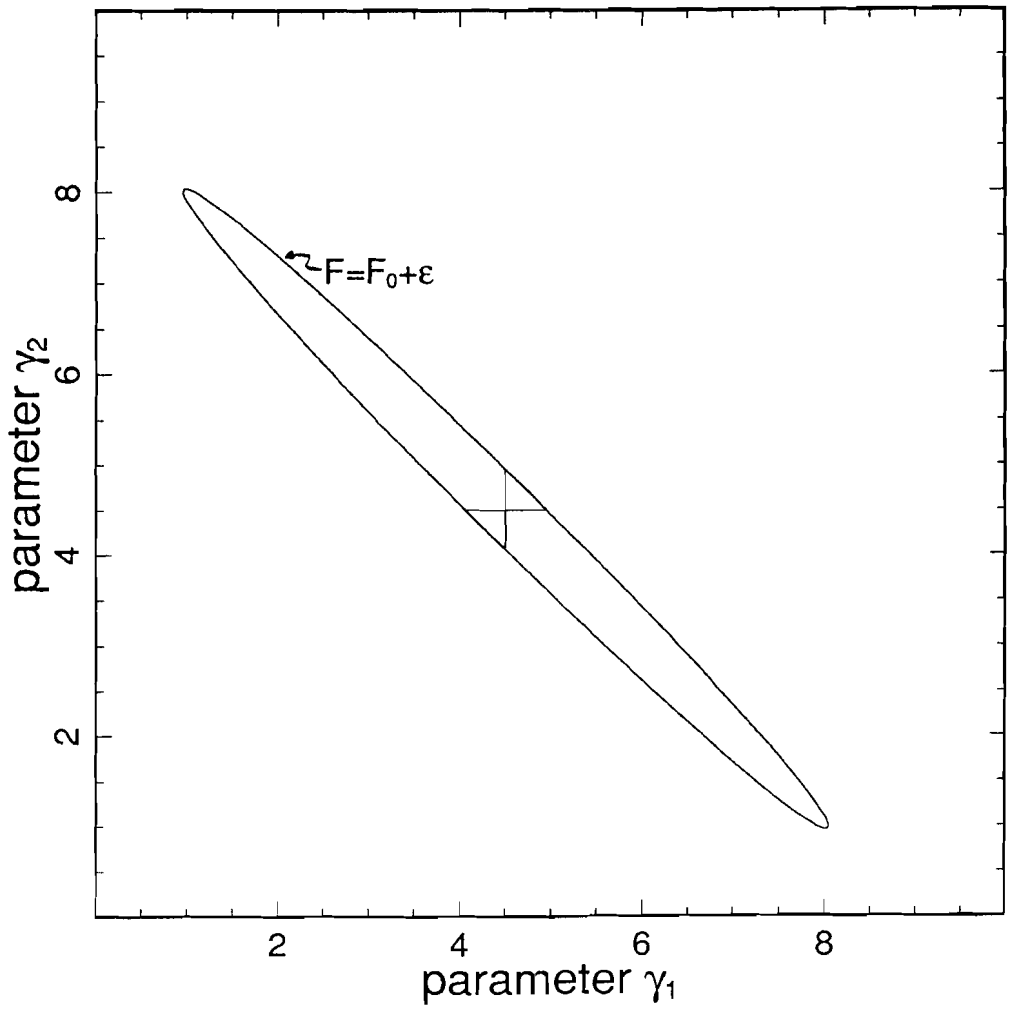

Figure 5.2. A hypothetical example of a misfit function. The contour for a misfit level ε is shown. In this case $\gamma_1+\gamma_2$ is much better constrained than $\gamma_1-\gamma_2$. If uncertainties in γ where read by measuring their possible deviation from the minimum (cross in the center), an optimistic error estimation would result.

For the more complicated cases with more than two parameters, the set of parameters with uncorrelated errors is determined as follows. We approximate the objective function around γ_{opt} by a second order Taylor expansion:

$$F(\boldsymbol{\gamma}) \approx F(\boldsymbol{\gamma}_{opt}) + \tfrac{1}{2}(\boldsymbol{\gamma}-\boldsymbol{\gamma}_{opt})^T \mathbf{H} (\boldsymbol{\gamma}-\boldsymbol{\gamma}_{opt}) \qquad (11)$$

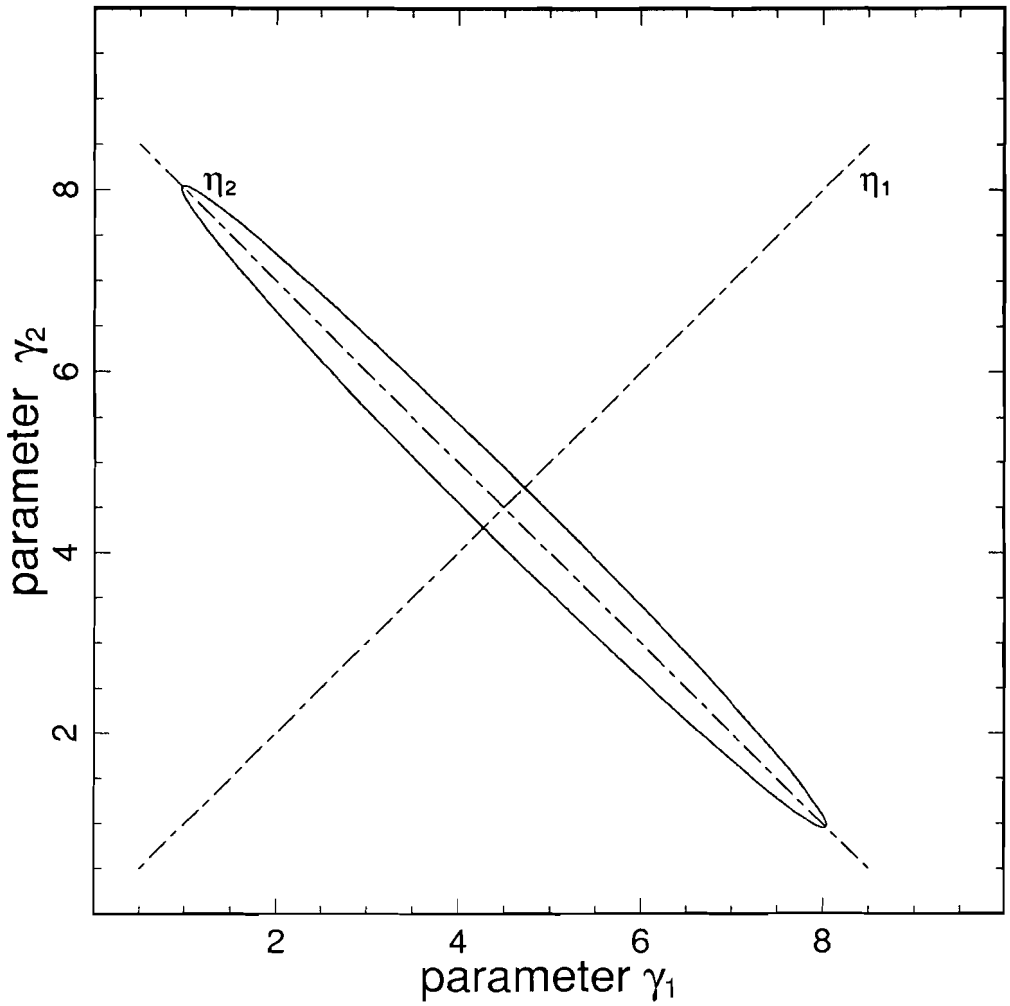

Figure 5.3. After transformation (equation 14), uncertainties in parameters $\eta_1=\gamma_1+\gamma_2$ and $\eta_2=\gamma_1-\gamma_2$ can be correctly determined (equation 16).

where **H** is the Hessian matrix in γ_{opt}:

$$H_{ij} = \frac{\partial^2 F}{\partial \gamma_i \partial \gamma_j} \tag{12}$$

We use **H** to transform the parameters γ_i into a set of independent parameters η_j with estimated errors. If we transform **H** to diagonal form:

$$\mathbf{H} = \mathbf{S}\Lambda\mathbf{S}^T \tag{13}$$

where the columns of **S** are orthogonal eigenvectors since **H** is symmetric, we can define a new datum:

$$\boldsymbol{\eta} = \mathbf{S}^T\boldsymbol{\gamma} \tag{14}$$

The region $\Delta\gamma=\gamma-\gamma_{opt}$ that gives an acceptable fit is defined by:

$$\tfrac{1}{2}\Delta\boldsymbol{\gamma}^T\mathbf{H}\Delta\boldsymbol{\gamma} < \varepsilon \tag{15}$$

This implies for the transformed parameters that $\tfrac{1}{2}\Delta\eta^T\Lambda\Delta\eta<\varepsilon$, or

$$|\Delta\eta_i| \le \sqrt{\frac{2\varepsilon}{\lambda_i}} \tag{16}$$

The velocity perturbation $\delta\beta(\mathbf{r})$ now satisfies, instead of (6),

$$\frac{1}{\Delta_j}\int_{P_j}\delta\beta(\mathbf{r})d\Delta = \sum_{i=1}^{N}\sum_{j=1}^{N} S_{ij}\eta_j h_i(r) = \sum_{j=1}^{N}\eta_j g_j(r) \tag{17}$$

with transformed basis functions

$$g_j(r) = \sum_{i=1}^{M} S_{ij}h_i(r) \tag{18}$$

(17) represents an infinite set of equations, since r is a continuous variable. In order to reduce (17) to a finite set of independent equations, the dual basis $\tilde{g}_j(r)$ is introduced, which satisfies an orthogonality condition with the original set of basis functions $g_i(r)$

$$\int_0^a \tilde{g}_j(r)\cdot g_i(r)\,dr = \delta_{ij} \tag{19}$$

Multiplication of (17) with $\tilde{g}_k(r)$ and integration over depth gives a set of linear constraints for $\delta\beta(\mathbf{r})$

$$\frac{1}{\Delta_j}\int_{P_j}\int_0^a \delta\beta(\mathbf{r})\cdot\tilde{g}_k(r)dr\,d\Delta = \eta_k \pm \Delta\eta_k \tag{20}$$

To give an impression on what kind of functions the $\tilde{g}_k$ are, figure 5.4 shows the $\tilde{g}_k(r)$ from the inversion of the recorded seismogram of the Romania, 30 august 1986, earthquake in station NE03. In (20) $\delta\beta(\mathbf{r})$ is the perturbation of the velocity with respect to the specific reference model that we used for the path.

In order to make the equation independent of the reference model, the integral over the reference model $\beta^0(r)$ is added to each side of (20):

$$\frac{1}{\Delta_j}\int_{P_j}\int_0^a \delta\beta(\mathbf{r})\cdot\vec{g}_k(r)drd\Delta = \frac{1}{\Delta_j}\int_{P_j}\int_0^a \delta\beta^0(r)\cdot\vec{g}_k(r)drd\Delta + \eta_k \pm \Delta\eta_k \tag{21}$$

All the quantities on the r.h.s. of (21) are known and are related in a linear way to the 3-D velocity $\beta(\mathbf{r})$, which is the unknown parameter in the equation.

For each fitted seismogram, the partitioned inversion results in a set of linear constraints on $\beta(\mathbf{r})$ of the form of (21). In the next sections it is shown how they are combined into a

5.4 The linear inversion for a 3-D velocity model

By fitting many seismograms belonging to criss crossing paths, we assemble a large set of linear constraints in the form of (21) for each source-receiver path. The final step of the partitioned waveform inversion is to combine all linear constraints in a linear inversion for a 3-D velocity model $\beta(\mathbf{r})$. In this inversion, the η_i act as data with uncertainties $\Delta\eta_i$. In general, this data set will be underdetermined so we want to impose a minimum norm (and/ or smoothness) constraint on the solution. Therefore, it is useful to transform the set of equations into a set of equations on $\delta\beta(\mathbf{r})$, which is the deviation of $\beta(\mathbf{r})$ from an appropriate reference model $\beta^R(\mathbf{r})$ for the region under consideration. $\beta^R(\mathbf{r})$ may be different model than $\beta^0(r)$ used for the path in the last section. This is simply done by subtracting from both sides of (21) the path integral of $\beta^R(\mathbf{r})$:

$$\int_{P_k}\int_0^a \vec{g}_k(r)\delta\beta(\mathbf{r})drd\Delta = \eta_k - \int_{P_k}\int_0^a \vec{g}_k(r)\beta^R(\mathbf{r})drd\Delta \pm \Delta\eta_k \tag{22}$$

We changed the indexing of the paths to conform to the data index and replaced P_j and Δ_j by P_k and Δ_k. This doesn't change the system of equations, because the path of the $k-th$ datum is equal to the "old" path j. Furthermore, to scale the data to unit variance, each datum is divided by $\Delta\eta_k$. Writing $G_k(r)$ for the scaled kernel and q_k for the scaled and shifted datum η_k, (22) becomes:

$$\int_{P_k}\int_0^a G_k(r)\delta\beta(\mathbf{r})drd\Delta = q_k \pm 1 \tag{23}$$

We now expand $\delta\beta(\mathbf{r})$ as a sum of basis functions $s_i(\mathbf{r})$, $i=1,...M$:

$$\delta\beta(\mathbf{r}) = \sum_i^M b_i s_r(\mathbf{r}) \tag{24}$$

For the horizontal coordinates, the s_i are defined as discrete rectangular cells. For the vertical coordinate, the "layers" are defined as depth functions equal to the basis functions $h_i(\mathbf{r})$ used in the non-linear inversion. The reason for this is purely practical: the parameters which are needed to compute the synthetic seismograms as predicted by the 3-D model can

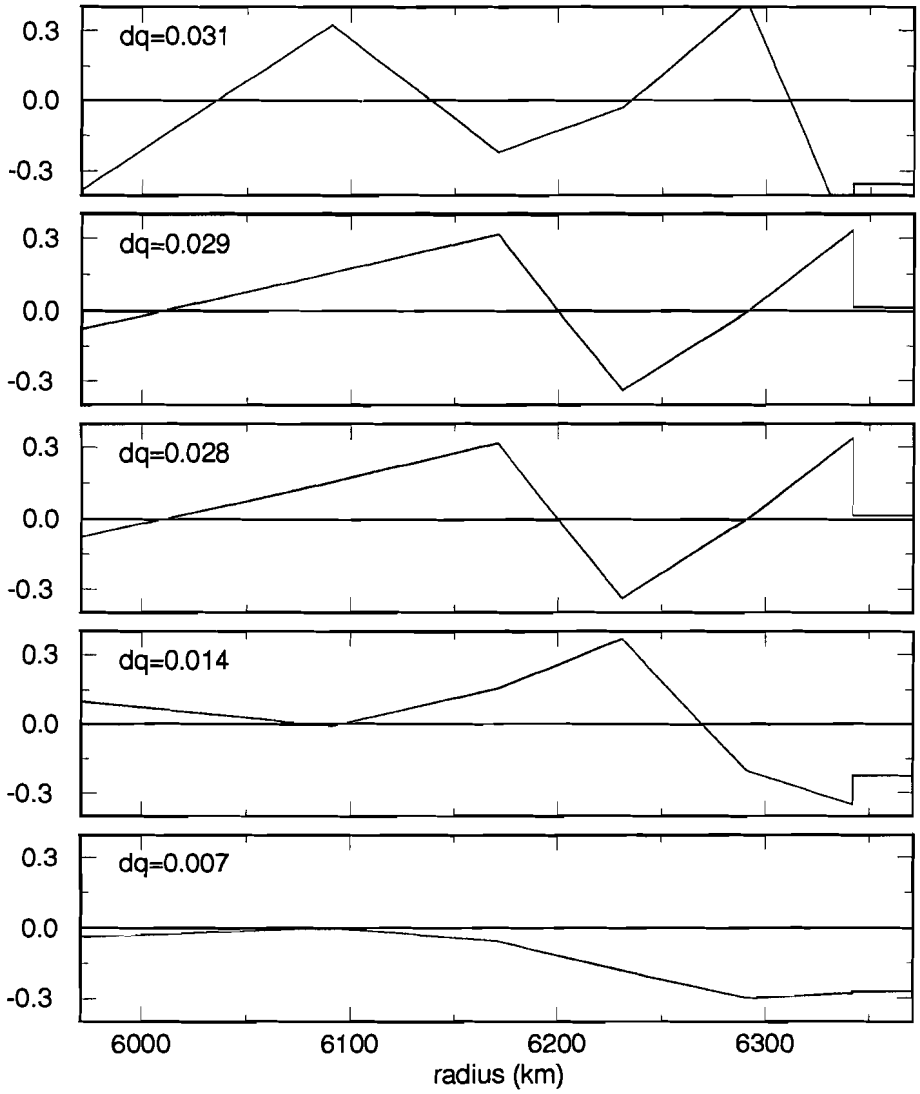

Figure 5.4. An example of a set of dual basis functions $g_k(r)$ for the S velocity along the path between the Romania earthquake of August 30, 1986, and station NE03 (see figure 6.1). Amplitude is in 10^{-8}/m, the horizontal scale is radius in km. In every plot, dq denotes the uncertainty ($\Delta\eta_k$ in equation 21) for every constraint in m/s. Note that the most precise constraint, at the bottom of the figure, averages the S velocity in the lithosphere.

now, without any interpolations, be calculated from the inversion output. In formula, the s_i are :

$$s_i(\theta,\phi,r)=l_i(\theta,\phi)h_i(r)$$

$l_i(\theta,\phi)=1$ if (θ,ϕ) are inside the cell defined for the horizontal coordinates, 0 elsewhere. Depending on which layer s_i belongs to, h_i is a boxcar or triangular shaped function (see figure 5.1). Inserting this expression in (23) yields:

$$\sum_i A_{ki} b_i = q_k \pm 1$$

in which

$$A_{ki} = \int_{P_k}\int_0^a l_i(\theta,\phi)h_i(r)G_k(r)dr d\Delta = \frac{L_{ik}}{\Delta_k}\int_0^a h_i(r)G_k(r)dr \tag{25}$$

L_{ik} is the length of the segment of path k in cell i. The matrix equation for the model **b** with elements b_i, $i = 1,..M$ and data **q** with q_k, $k=1,...N$ is:

$$\mathbf{Ab}=\mathbf{q}$$

The elements of **A** have been defined in (25). We choose to impose a minimum norm and minimum gradient constraint on the solution. We do this by searching the model **b** that minimizes a weighted sum of data misfit, model norm and norm of the gradient of the solution:

$$\min\left[(\mathbf{Ab}-\mathbf{q})^T(\mathbf{Ab}-\mathbf{q}) + \alpha\mathbf{b}^T\mathbf{b} + \gamma(\mathbf{Gb})^T(\mathbf{Gb})\right] \tag{27}$$

G is the operator that yields the gradient of model **b** α and γ are weights that determine the trade-off between data misfit, model norm and gradient norm. Following Nolet (1987b) we regard this as the minimisation problem to the linear system:

$$\begin{bmatrix}\mathbf{A}\\ \alpha\mathbf{I}\\ \gamma\mathbf{G}\end{bmatrix}\mathbf{b} = \begin{bmatrix}\mathbf{q}\\ \mathbf{0}\\ \mathbf{0}\end{bmatrix} \tag{28}$$

I is the identity matrix, it provides the term $\mathbf{b}^T\mathbf{b}$ in (28), which is the (squared) norm of **b**. **G** is assembled from three matrices $\mathbf{G}_r$, $\mathbf{G}_\theta$ and $\mathbf{G}_\phi$ which yield the first order derivatives in the r, θ and ϕ direction, respectively.

$$\begin{bmatrix}\mathbf{G}\end{bmatrix} = \begin{bmatrix}\gamma_v\mathbf{G}_r\\ \gamma_h\mathbf{G}_\theta\\ \gamma_h\mathbf{G}_\phi\end{bmatrix}$$

Different weights γ_h and γ_v have now been assigned to the derivatives in the horizontal and vertical direction. This allows us to apply different constraints on the smoothness of the solution in these directions. Equation (28) is solved with the LSQR algorithm (Paige and Saunders, 1982).

Chapter 6

Partitioned waveform inversion: the non-linear waveform inversion

6.1 Introduction

In chapter 5 we focussed on the theory of the Partitioned Waveform Inversion (PWI). Here, we describe the application of the first step of the PWI, i.e., the non-linear inversion of seismograms for average one-dimensional (1-D) velocity models. We show specific examples of waveform fits and discuss how, in practice, we tried to ensure the validity of essential assumptions concerning the starting model and the accuracy of the focal parameters. We inverted waveforms for periods between 16 and 100 s. Consequently, we collected our data from both long period and broadband stations.

6.2 Data

The digitally recording long period and broadband stations of which we assembled data are listed in table 6.1. Most data were collected from the NARS and GDSN stations because these stations have been operational for a long time. Data from the stations OBN and KIV in eastern Europe, which became available only during the last months of this study were also used, which improved the path coverage considerably.

Table 6.1

Station	Lon (deg)	Lat (deg)	Network	# data used
UKNET			Blacknest	
EKA	-3.159	55.333		3
HEA	-1.264	51.358		1
LLW	-3.665	52.849		3
MMY	-1.869	54.176		2
SBD	-4.686	50.565		2
LAM	-4.068	52.114		1
WOL1	-1.223	51.313		2
GDSN/IRIS				
NRA0	11.5414	60.7353	USTN	10
KEV	27.0066	69.7553	DWWSSN	17
KONO	9.5982	59.6490	ASRO	26
TOL	-4.0484	39.8814	DWWSSN	9
BER	5.3257	60.3868	DWWSSN	4
BGIO	35.0877	31.7219	SRO	3
ANTO	32.7935	39.8689	SRO	6
GRFO	11.2217	49.6919	SRO	8
OBN	36.57	55.11		8
KIV	42.68	43.95		7
NARS				
NE02	9.1700	56.4590		3
NE03	9.1530	55.0450		6
NE04	6.6680	52.8130		16
NE05	5.1720	52.0880		9
NE06	4.5950	50.0970		9
NE07	2.2320	49.0740		3
NE14	-3.5950	37.1900		10
NE15	5.7850	50.8670		8
NE16	3.1030	45.7630		8
NE10	-0.699	43.0860		4
NE08	1.7300	46.4200		1
NE17	-4.0490	39.8810		6
NE34	7.7710	52.3110		1
NE35	7.3480	51.9720		1
NE35	51.4419	7.2703		1
NE13	-4.0910	38.6850		1
NE11	-1.5170	41.8140		2

Table 6.1 (continued)

Station	Lon (deg)	Lat (deg)	Network	# data used
GRAEFENBERG				
GRA1	11.2217	49.6919		2
GRC2	11.5220	49.9960		1
GEOSCOPE				
SSB1	4.54000	45.2800	IDA	1
OTHER				
ATH	23.7200	37.9700	WWSSN	1
JER	35.2000	31.77	WWSSN	2
STU	9.2000	48.77	WWSSN	2
PTO	-8.6000	41.14	WWSSN	1
UME	20.2400	63.810	WWSSN	1
EIL	34.9500	29.5500	WWSSN	1

The only selection criterion for an event was the availability of an accurate source mechanism and hypocenter location. The density of stations in Europe is high and we anticipated that for events of magnitude m_b>4.5 epicenter locations are accurate enough for our purpose. For many events of magnitude m_b > 5.0, a HRVD (Harvard) source mechanism (Dziewonski et al., 1981) is reported; for events of m_b>5.8 a NEIC mechanism is usually reported as well. The HRVD and NEIC mechanisms are published in the Bulletins of the International Seismological Centre (ISC) and in the Preliminary Determination of Epicenters (PDE) monthly bulletins. Earthquakes of m_b>6.2 are less suitable because they often have complex source time functions which may not be modelled adequately by the reported half duration time of the HRVD mechanisms. The earthquakes of which we used seismograms are listed in table 6.2. Most of these events occurred in the Mediterranean and the Middle East. Because of the density of stations in western Europe, we can expect a good path coverage in central and western Europe. There are only few stations on the Baltic Shield and Russian Platform which limits the attainable resolution below these regions. To improve the path coverage we digitized a few analog records from long period WWSSN (World Wide Standardized Seismograph Network) stations.

6.3 The non-linear inversion

To distinguish between fits in the different stages of the inversion process we use hereafter the term "initial fit" for the fit of the waveform predicted by the starting model to the observed seismogram; the term "individual fit" refers to the fit obtained after non-linear inversion. For each seismogram to be inverted we examined the the assumptions concerning the starting model and the accuracy of the source parameters.

Table 6.2

Event	Date	time	Latitude (deg)	Longitude (deg)	depth (km)	m_b
1	12-05-1971	06:25:15.4	37.640	29.720	30.0	5.5
2	01-01-1980	16:42:38.6	38.750	-27.750	0.0	6.0
3	18-05-1980	20:02:56.5	43.310	20.870	20.0	5.7
4	28-05-1980	19:51:20.0	38.480	14.270	19.0	5.5
5	09-07-1980	02:11:57.3	39.290	22.910	47.0	5.8
6	23-11-1980	18:34:52.2	40.860	15.330	0.0	6.0
7	07-12-1980	17:37:08.8	36.060	1.300	0.0	5.3
8	25-02-1981	02:35:53.5	38.170	23.120	30.0	5.7
9	13-08-1981	02:58:12.5	44.850	17.330	16.0	5.3
10	27-12-1981	17:39:13.3	38.910	24.920	10.0	5.4
11	17-08-1982	22:22:20.0	33.710	22.940	23.0	6.1
12	16-11-1982	23:41:20.8	40.820	19.580	20.0	5.5
13	13-12-1982	09:12:51.0	14.670	44.230	18.0	5.8
14	19-03-1983	21:41:42.0	35.020	25.320	59.0	5.7
15	23-03-1983	23:51:05.5	38.230	20.290	13.0	5.6
16	28-05-1983	11:35:55.2	32.610	48.560	43.0	5.6
17	30-10-1983	12:40:25.5	40.350	42.170	31.0	5.3
18	22-12-1983	04:11:29.3	11.870	-13.530	11.0	6.2
19	07-05-1984	17:49:42.7	41.760	13.900	16.0	5.4
20	21-06-1984	10:43:40.5	35.310	23.280	25.0	5.8
21	30-04-1985	18:14:12.9	39.260	22.810	26.0	5.4
22	15-08-1985	04:28:47.4	47.060	18.010	10.0	4.7
23	27-09-1985	16:39:46.4	34.400	26.550	41.0	5.6
24	27-10-1985	19:34:57.2	36.430	6.780	10.0	5.4
25	09-11-1985	23:30:42.9	41.260	23.980	18.0	5.5
26	26-04-1986	14:15:07.7	36.520	71.100	185.0	5.6
27	05-05-1986	03:35:38.0	38.020	37.790	4.0	5.7
28	30-08-1986	21:28:36.0	45.540	26.310	137.0	6.3
29	13-09-1986	17:24:34.3	37.080	22.150	28.0	5.8
30	11-10-1986	09:00:10.9	37.940	28.560	5.0	5.4
31	25-11-1986	13:59:41.5	44.130	16.360	22.0	5.2
32	07-12-1986	14:17:08.1	43.290	25.940	7.0	5.1
33	14-01-1987	11:03:49.3	142.880	42.450	108.0	6.3
34	27-02-1987	23:34:52.1	38.460	20.330	5.0	5.3
35	09-01-1988	01:02:47.4	41.250	19.660	30.0	5.2
36	26-03-1988	12:07:29.7	33.200	13.280	10.0	4.8
37	26-04-1988	00:53:43.8	42.370	16.610	8.0	5.0
38	17-03-1989	05:42:54.5	34.660	25.450	31.0	4.9
39	19-03-1989	05:36:59.2	39.240	23.500	10.0	5.2
40	27-04-1989	23:06:52.2	37.030	28.180	14.0	5.3
41	07-06-1989	19:45:53.7	38.060	21.620	25.0	5.0
42	14-06-1989	18:06:38.3	34.290	26.060	14.0	5.2
43	24-06-1989	03:09:58.3	36.710	35.930	46.0	4.9
44	27-08-1989	01:21:17.9	34.920	26.240	61.0	5.0

Table 6.2 (continued).

Event	Date	time	Latitude (deg)	Longitude (deg)	depth (km)	m_b
45	29-10-1989	19:09:12.9	36.790	2.450	6.0	5.7
46	05-05-1990	07:21:29.5	40.780	15.770	10.0	5.3
47	31-05-1990	00:17:4.:5	45.810	26.770	88.0	6.1
48	16-06-1990	02:16:21.2	39.260	20.530	32.0	5.6
49	18-07-1990	11:29:24.5	36.990	29.590	17.0	5.2

In the non-linear inversion, it is assumed that the starting model does not deviate too much from the average properties of the Earth along the wave path so that the relationship between the wavenumber perturbation and the perturbation of the shear velocity can be linearized (equation 5, chapter 5). In the present study we used three starting models for the waveform inversion, because in Europe we can distinguish three large provinces: the pre-Cambrian Baltic Shield/Russian Platform, the younger regions of west and central Europe, which have a thinner crust than the pre-Cambrian regions, and the Mediterranean, the western part of which is oceanic and the eastern part probably partly continental, partly oceanic (e.g., Morelli, 1985). For these provinces we used the models PREM (Dziewonski and Anderson, 1981), EUR, and USA (see figure 6.1). EUR and USA are modified PREM models of continental character and have a crustal thickness of 29 and 40 km, respectively. PREM has a thinner crust of 24.5 km and a low velocity zone and represents a mixed oceanic-continental path. The source-station configuration brings about that many wave paths cross at least two tectonic provinces. For each seismogram to be fit, we chose the starting model that gives the best approximation of the average seismic properties along the wave path. Furthermore, we used different models to calculate synthetic amplitudes for the source and station location if appropriate. In figure 6.2 we show the predicted waveforms at station NE04 for an event in the Mediterranean (33.71N, 22.94E), on August 17 1982, computed for different models for the source location. For the path and the station location we used model EUR, for the source we tried model PREM (thin solid line) and EUR (dashed line). This example shows that the structure at the location of the source influences the waveform by affecting the excitation. The difference between the two synthetics is much smaller than the misfit for the low frequency part of the signal, but the phase shift for the dominant frequency of 40 mHz is significant. The synthetic computed with PREM resembles better the observed fundamental mode, while the predicted waveforms of the S wave are similar, apart from a time shift. In view of the location of the source the choice of PREM seems reasonable. In absence of a priori information on the structure for a particular region, the choice of the background model that gives the best initial fit represents the conservative viewpoint that no misfit should be ascribed to lateral heterogeneity unless absolutely necessary.

In the PWI it is assumed that the hypocenter locations and source mechanisms are accurate. To avoid that errors in hypocenter location and focal mechanism propagate as velocity perturbations in the average model for the wave path, we always checked the initial fits. The hypocenter locations were taken from the Bulletins of the International

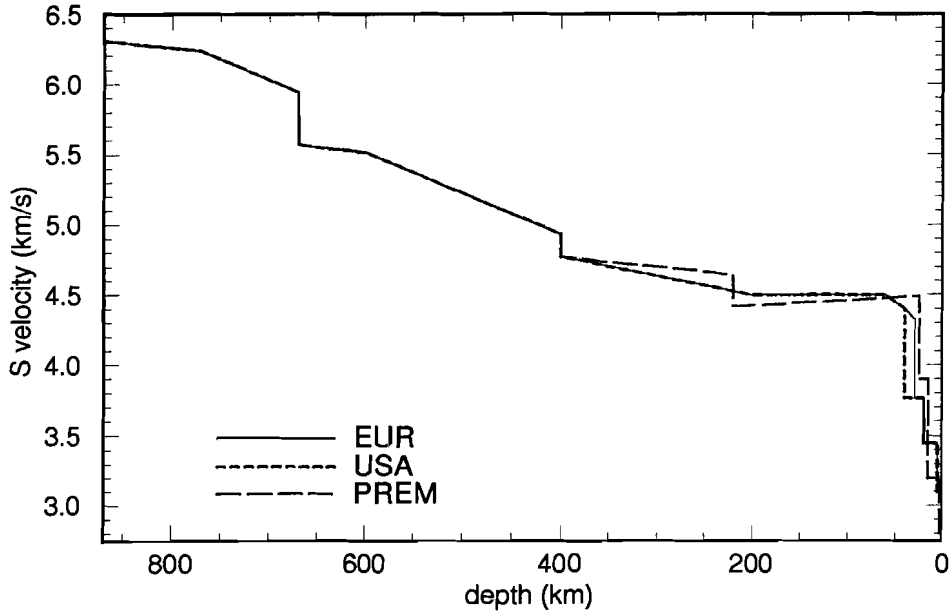

Figure 6.1. Shear velocity of the starting models used in the study.

Seismological Centre. For recent events, for which no ISC hypocenter locations were published yet, we used the hypocenter reported in the PDE monthly bulletins. The focal depth reported by the ISC is the most accurate depth determination for many events in our data set, which contains many events with $m_b < 5.8$. However, there can be large errors in these depths. Even for events of $m_b \geq 5.5$ the depth determined by ISC from pP–P differential travel times differs from the depth determined in the ISC hypocenter location procedure, in which only P data are used. For example, for an event in Sicily ((38.48N, 14.27E); May 28 1980; m_b=5.5) the depth determined from pP and P differential times is 66 km, the depth resulting from the hypocenter location procedure is 19 km. We computed synthetic seismograms for the two focal depths, for different Earth models for the source location. We chose model EUR for the source location and a focal depth of 19 km because this combination gave the best initial fit. The choice of the focal mechanism that gives the best initial fit is in agreement with the above mentioned viewpoint that no misfit should be ascribed to lateral heterogeneity unless absolutely necessary. This is the largest difference in focal depth that we observed. In other cases differences were smaller, though significant for waveform inversion. To model the source, we used the HRVD source mechanisms, the NEIC mechanisms (published in the PDE monthly bulletins), or other mechanisms if available. In most cases the HRVD mechanisms were judged to be accurate. As with the focal depth, if different mechanisms were published for the same event, we chose the one

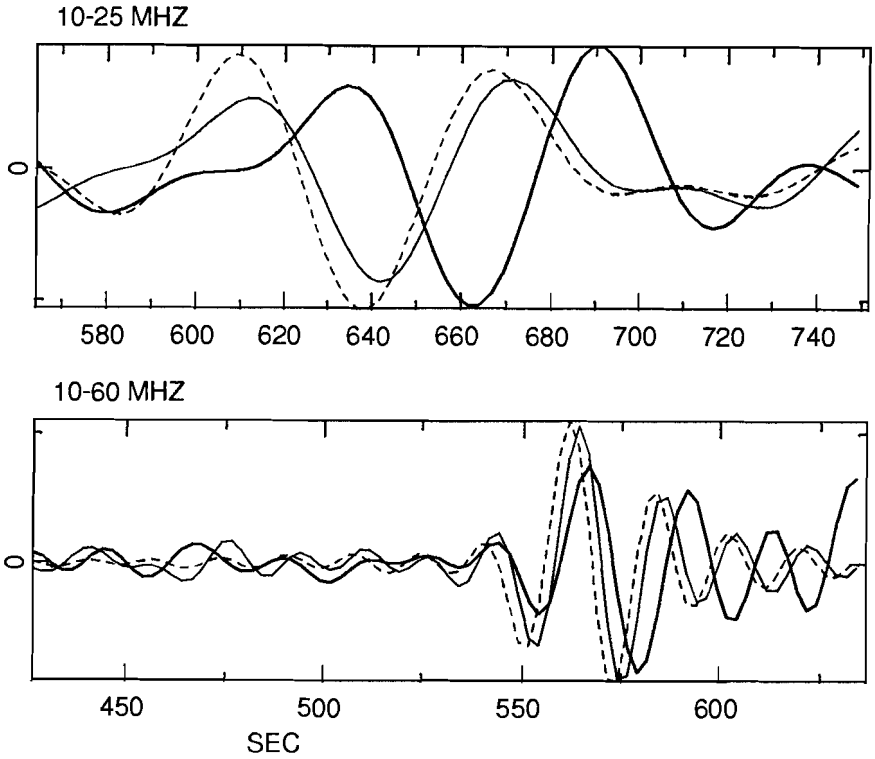

Figure 6.2. Predicted waveforms at station NE04, for an event in the Mediterranean on August 17, 1982. Model EUR is used for the path and station, for the source location we took respectively model PREM (thin solid line) and model EUR (dashed line). The thick solid line represent the observed waveform. The upper window, containing the fundamental mode, is low passed at 25 mHz, the lower window is low passed at 60 mHz.

giving the best initial fit. We found that even for large events, m_b>5.9, the HRVD mechanisms are not always accurate enough. It was, for instance, impossible to fit the waveforms of the Romania event on August 30, 1986, m_b=6.3, with the HRVD mechanism. Instead, we obtained very good fits with the mechanism reported by Monfret et al. (1990). For the event in Turkey, on October 30 1983, m_b=6.0, we used the NEIC-P mechanism because the HRVD mechanism failed to fit the S waves of the records. For 13 events (out of 59) we did not believe the HRVD mechanism to be accurate because it yielded bad initial fits. We were able to use 3 of these 13 events because other, accurate, mechanisms were available.

Synthetic seismograms are calculated by summing 20 modes for phase velocities below 11 km/s. The algorithm allows inversion of waveforms for perturbations of β and Q with respect to the starting model. However, in a number of cases, we could not fit the

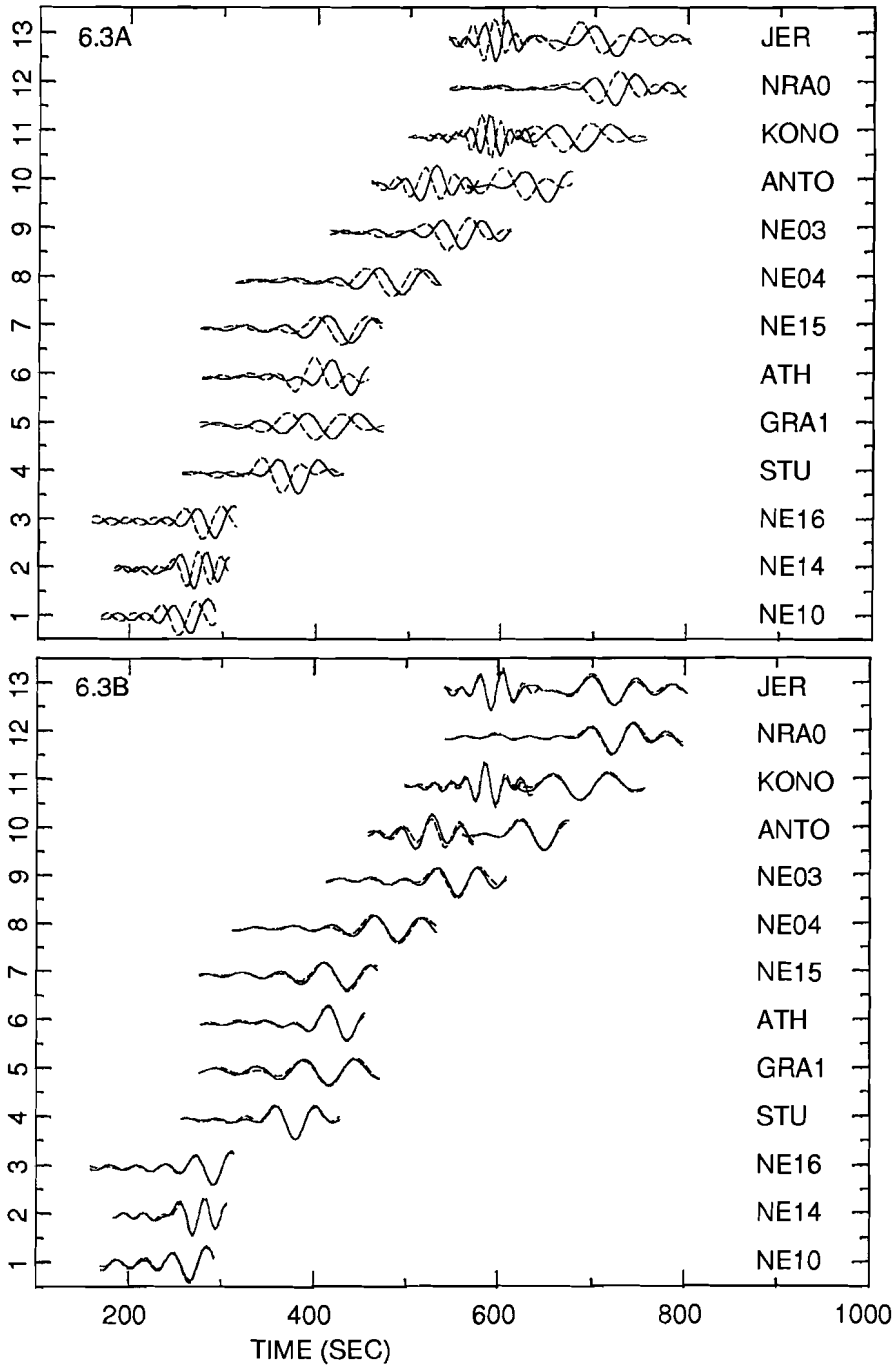

Figure 6.3. a) Observed waveforms (solid lines) of the Constantine event in Algeria (36.43N, 6.78E) on October 27, 1985, and predictions by the starting models (dashed lines). b) Individual fits obtained after non-linear inversion. Synthetic (observed) waveforms are depicted with dashed (solid) lines.

amplitudes of the waveforms satisfactorily by perturbing Q. The reason for this might be that either the reported seismic moment for the event is not correct, or that the misfit function is scaled such that it is not sensitive enough for the perturbations of Q in these cases. Because we were not primarily interested in the values of Q, we usually decided to equalize the energy in the synthetic and the observed time series, and inverted for the shear velocity perturbations only.

We used the following procedure for the inversion of the seismograms. We select an event that contributes relevant wave paths, check if a source mechanism is available, and assess the quality of the seismograms. We then correct for the instrument response and convert the records to displacement seismograms. At this point, we compare the part of the seismogram containing the arrival of the S wave up to the fundamental mode of the Rayleigh wave with the waveform predicted by the most appropriate starting model for the source, wave path and station location. If the synthetics and the observations do not differ too much, which could indicate that the focal mechanism or depth is not accurate or that the starting models are not appropriate, we accept a seismogram for inversion. If the fundamental mode arrives clearly separate from the S wave (generally for epicentral distances larger than 23°) we select two time windows from the seismogram, one containing only the fundamental mode of the Rayleigh wave, and one containing the S waves and higher modes with a group velocity higher than 4.0-4.2 km/s, depending on the arrival time of the fundamental mode. This has the advantage that we can, in the subsequent inversion, weight the time windows to correct for the difference in amplitude of the body waves and surface waves and thus equalize their influence of the shape of the misfit function. Moreover, the windowing allows for the possibility to fit the body and surface waves for different frequency bands. Short period fundamental mode Rayleigh waves transport most energy in the strongly heterogeneous crust and are therefore subject to out-of-plane propagation and scattering (Snieder, 1988). To avoid the influence of scattering on the velocity model we used the filter to fit the fundamental mode for frequencies below 25 mHz, while we fitted the higher modes for higher frequencies. Kennett and Nolet (1990) concluded from theoretical tests that the assumption of independent mode propagation, which underlies this inversion, is valid for surface waves up to 20 mHz, and for body waves up to 50 mHz (depending on the character of the heterogeneity). However, the computations of Kennett and Nolet consider scattering in a 2-D model. They mention that the frequency limits can be too pessimistic for the 3-D case: "Once energy has been scattered into a different mode in a 3-D situation it is likely to have a significant angular spread. As a result, further scattering interactions with other modes are likely to be reduced." In general we were able to fit the body waves for frequencies as high as 60 mHz. Although this exceeds the limit indicated by Kennett and Nolet (1990) we continued with these fits to see if they yield a reasonable 3-D model. The windowing, weighting, and filtering is established through the operator R in equation 1 of chapter 5. The non-linear inversion procedure is iterative: in order to avoid ending up in a local minimum, we first determine the global minimum for a smooth misfit function, then allow

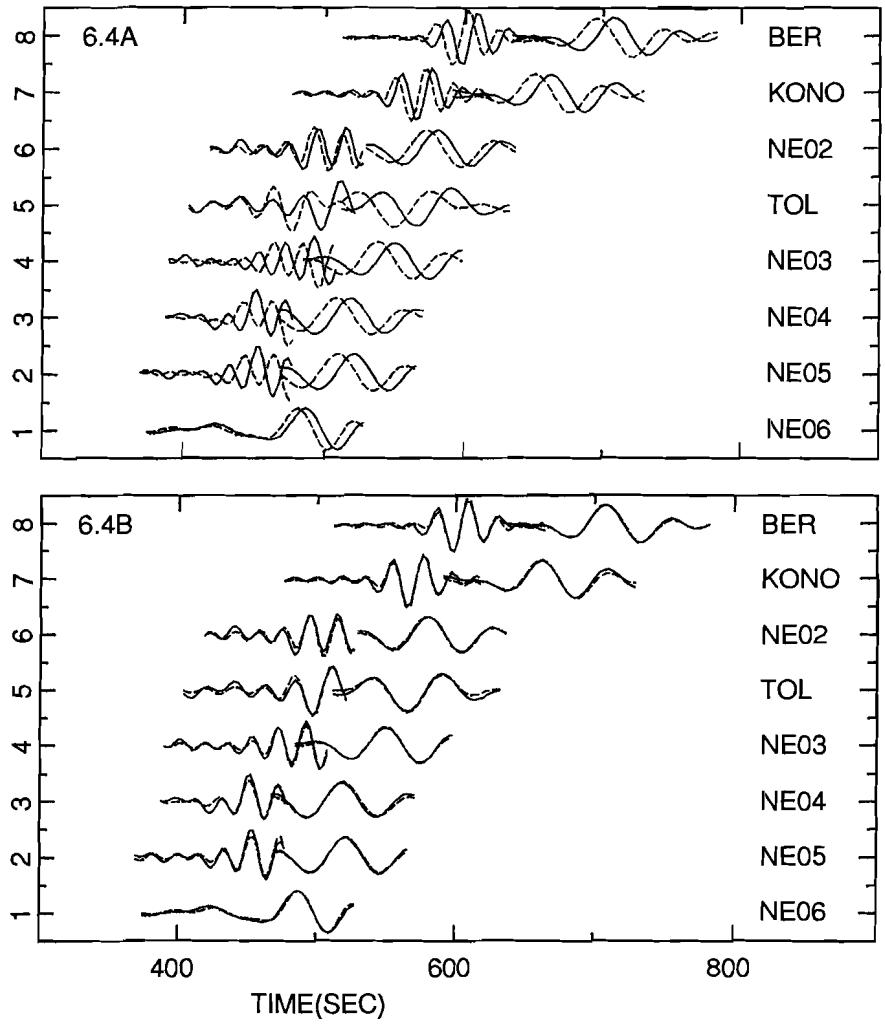

Figure 6.4. a) Observed waveforms (solid lines) of an event in Greece (38.29E, 20.26E) on March 23, 1983, and predictions by the starting models (dashed lines). b) Individual fits obtained after non-linear inversion. Synthetics are indicated with dashed lines, observed waveforms with solid lines.

more detail in the misfit function and search the new global minimum, starting from the previous one. More specific, in the first step we invert the envelope of the waveforms; subsequently we fit the waveforms with a strong low pass filter in R, starting with the perturbations retrieved in the last inversion, and add increasingly higher frequencies to the signal by adjusting the low pass filter. The latter step is repeated until we reach the

frequency level beyond which we can not fit the body waves. In each inversion we start with the velocity perturbations found in the previous inversion. At epicentral distances shorter than about 23° the triplicated S waves arrive shortly before the Rayleigh wave which makes it difficult to separate the body and surface wave into two time windows. Moreover, we observed that at these distances the S wave contains little energy below 30 mHz. Because fitting S and LR in separate time windows resulted in bad fits we adjusted the inversion scheme for records below 23°. We obtained the best fits for these data by inverting S and LR initially in one time window. After a few inversions, when we arrived at frequencies where the S wave is a pronounced signal (usually at 35 mHz), we split the window into a window containing the S wave and a window containing the LR wave. In the subsequent inversions we low passed LR at 25 mHz and continued the inversion procedure to fit the S waves for higher frequencies.

When an optimum fit is obtained, the independent linear constraints on the average velocity-depth profile along the wave path are determined (see chapter 5). The acceptable misfit level ε of the misfit function is determined by computing synthetics for small deviations $\Delta\gamma$ from the optimum model γ_{opt}, and judging visually what the maximum acceptable misfit level is.

With the above described standard procedure, we obtained good fits for many records. In figures 6.3a and 6.3b we show the initial and individual fits for the records of the Constantine event in Algeria, on October 27, 1985. Figures 6.4a and 6.4b display the initial and individual fits for an event in the Ionian Sea, on March 23, 1983. The predicted waveforms resemble the observations but there is a difference in arrival time. After inversion, we obtained good fits for all records. For stations NE06 and NE10 we were unable to fit, respectively, the S wave and the entire record for this event.

We obtained many good fits with the standard procedure, but the non-linear inversion is not an automatic procedure. The inversion of some records needed special attention. For example, the displacement seismograms of the Romania event on August 30, 1986, at stations NE03, NE04, NE05, NE15, and NE06 are contaminated with long period noise which prohibited an acceptable fit. For these stations we inverted the velocity seismograms instead, because the low frequencies are suppressed in the velocity seismograms. For the other stations we fitted the displacement seismograms. In figures 6.5a and 6.5b we show the initial and individual fits. For the records of stations NE03, NE04, NE05, NE15, and NE06 we fitted the S body wave and Rayleigh wave in one time window, because splitting would result in windows of less than 100 s, which is too short to apply Fourier transformation for periods of 100 s.

In some cases we had to experiment with the weighting of the time windows to obtain a satisfactory fit. As an example we discuss the inversion of the waveforms of an event in Albania, on June 16, 1990, recorded at station KEV. The amplitude of the fundamental mode is roughly 2.5 times the amplitude of the S wave. Initially we weighted the S wave window at 3x the weight of the surface wave window. Figure 6.6 shows the resulting fit, which we considered unsatisfying because the first downward and upward deflections of

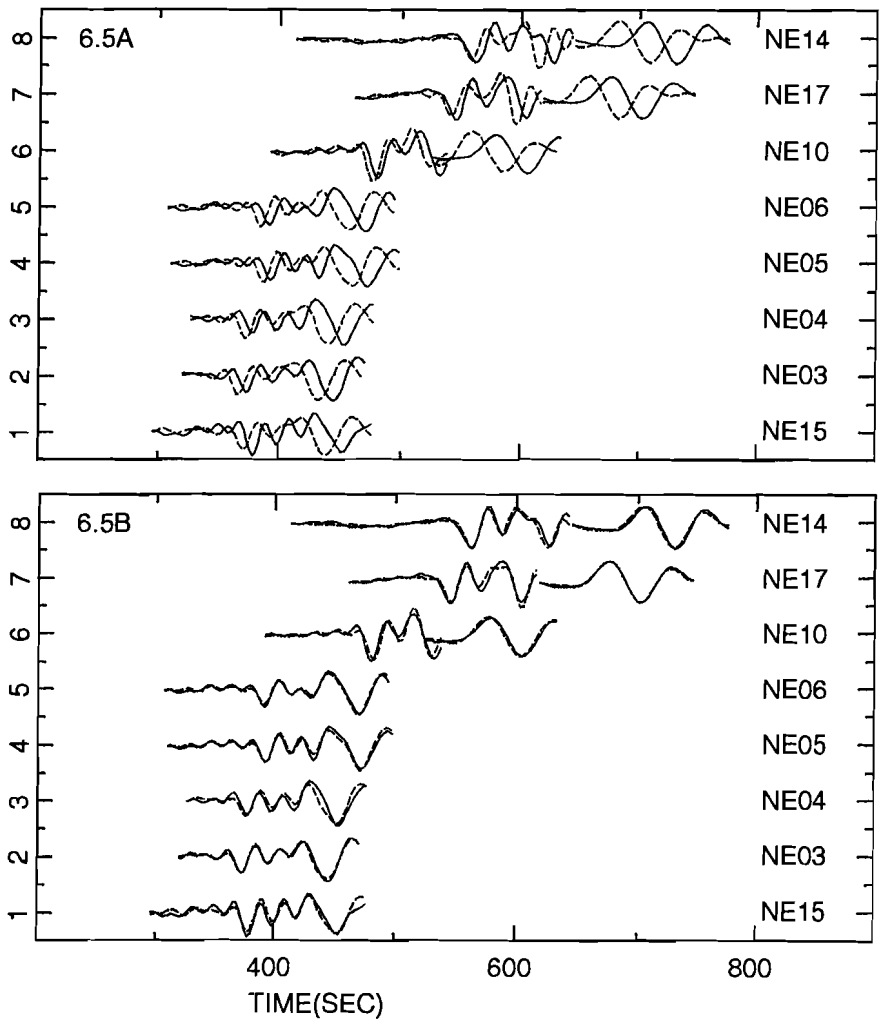

Figure 6.5. a) Observed waveforms (solid lines) of the Romania event (45.54N, 26.31E) on August 30, 1986, and predictions by the starting models (dashed lines). b) Individual fits obtained after non-linear inversion. Synthetics are indicated with dashed lines, observed waveforms with solid lines.

the S wave show a time mismatch of a few seconds. By weighting the S wave window at 8x against the surface wave, we were able to improve the fit (see figure 6.6).

We mentioned above that we checked the focal mechanism and focal depth for each event because we want to avoid that errors in these parameters propagate as velocity perturbations in the average 1-D model for the wave path. For a few events completely

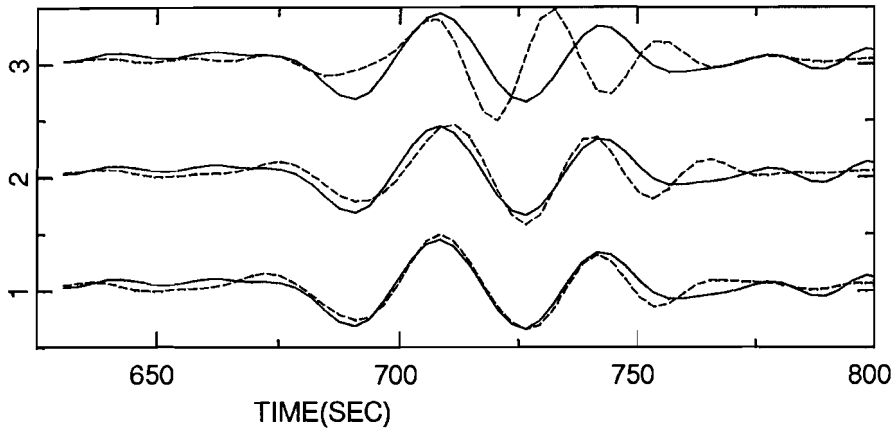

Figure 6.6. Influence of weighting on the fit of the S wave of an event in Albania (39.26N, 20.53E), on June 16, 1990, recorded at station KEV. Synthetics are displayed by a dashed line, data by a solid line. In the upper trace (3) we show the initial fit. The middle trace (2) shows the fit obtained after weighting the S wave 3x against the fundamental mode of the Rayleigh wave. The lower trace (2) shows the fit obtained after weighting the S wave 8x against the fundamental mode. All records are low passed at 60 mHz.

different focal mechanisms were published. As an example we discuss the event that occurred west of Crete, on June 21, 1984. Three different focal mechanisms, which are given in table 6.3, were available for this event.

Table 6.3

	dip	rake	strike
HRVD	85	-86	298
NEIC-P	87	-33	285
Taymaz et al. (1990)	72	83	110

None of the three mechanisms gave good initial fits to all seismograms. We fitted the seismograms of this event for all three mechanisms. The HRVD mechanism yielded the best individual fits (see figure 6.7) and therefore we preferred this mechanism. We were unable to fit the record at station NE10. Although the initial fits were not very good, we accepted the fits of this event because there were no other events at approximately the same location for which a mechanism was available.

Figure 6.8 shows the 217 wave paths for which we obtained good individual fits. We used 49 earthquakes. The 217 seismograms yielded 920 linear constraints, with a useful error, on the S wave velocity below Europe. For particular events we could fit most, but not all records. For some records we were able to fit the Rayleigh wave only. In figure 6.9 we

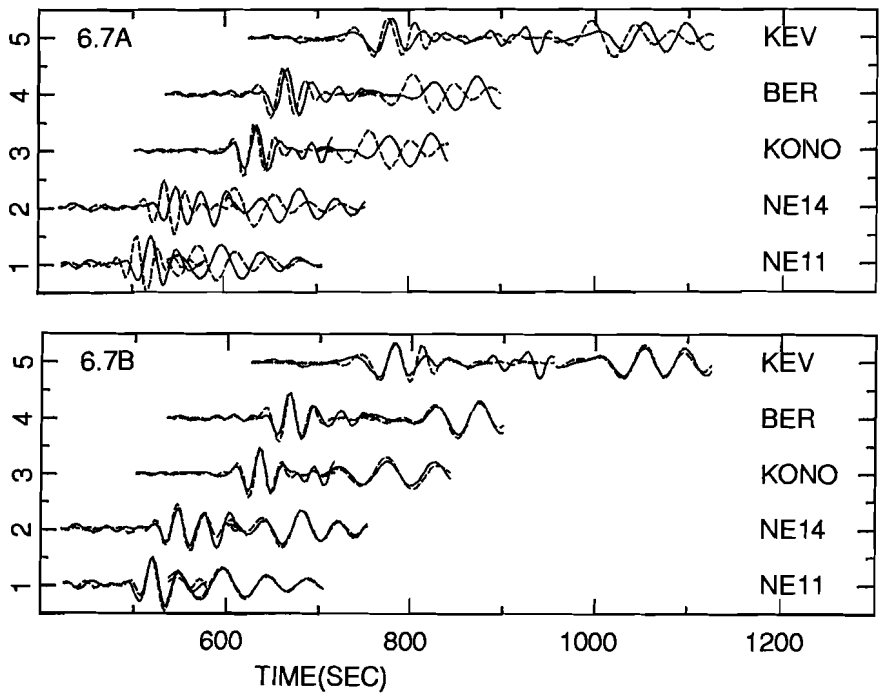

Figure 6.7. a) Observed waveforms (solid lines) of an event near Crete (35.31N, 23.28E) on June 21, 1984, and predictions by the starting models (dashed lines). b) Individual fits obtained after non-linear inversion. Synthetics are indicated with dashed lines, observed waveforms with solid lines.

show a map with the wave paths for which we could not fit the S wave (dashed lines), and for which we could not fit the entire record (solid lines). Comparing this map with figure 6.8, we see that the Mediterranean shows up as a region with a relatively large number of failures. Although we cannot exclude inaccurate focal mechanisms, we think that this regions is characterized by strong lateral heterogeneity, which causes out-of-plane propagation or mode conversion, and consequently distorts the seismograms to such an extent that the waveforms cannot be inverted using the simple path integral approximation. It is less clear why we could not fit the S waves on some of the records for paths from southern Europe to western Europe and the Baltic Shield. Since we fitted S waves for many nearby wave paths, we suspect inaccuracies of the focal mechanism or lateral heterogeneity confined to a small region around the wave path. This can also be the cause that we were unable to fit some of the S waves for wave paths from southern Europe to the Baltic Shield. However, the lateral heterogeneity must be confined to a small region around these wave paths because we could fit the entire records for many nearby wave paths.

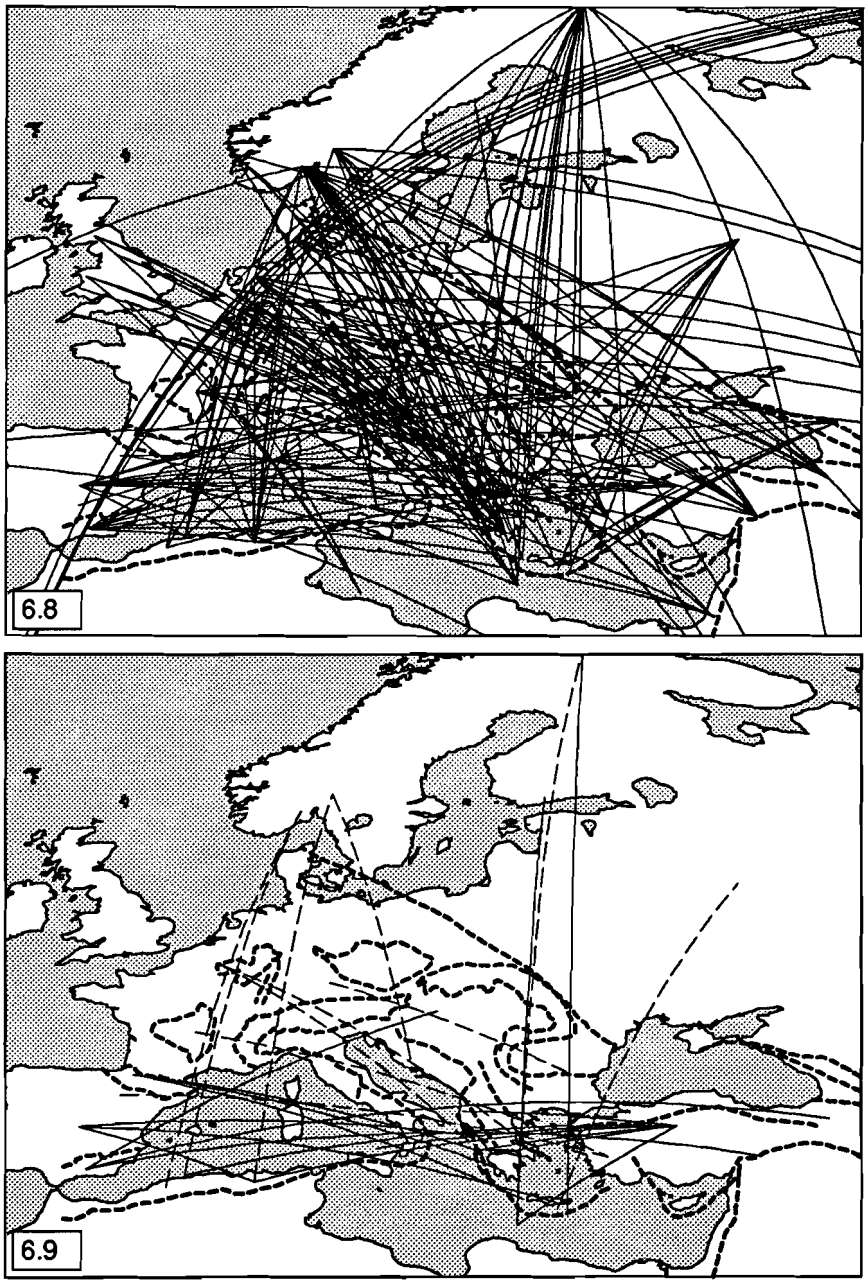

Figure 6.8. Wave paths for which we obtained good individual fits. The triangles indicate the locations of the stations. The dashed lines depict outlines of major tectonic features.

6.4 Conclusions

We inverted waveforms of S waves and fundamental mode Rayleigh waves recorded at stations in Europe in a systematic way. Usually, we equalized the energy of the waveform predicted by the starting model and the observed waveform, and inverted for the shear velocity perturbations. In general we obtained good fits. We low passed the fundamental mode of the Rayleigh wave at 25 mhz to avoid that scattering influences the values of the linear constraints (Snieder, 1988; Kennett and Nolet, 1990). Many body waves could be fitted well for frequencies as high as 60 mHz. Despite considerable effort we were unable to fit a number of seismograms belonging to wave paths in the Mediterranean. Lateral heterogeneity, causing out-of-plane propagation and mode conversion, is probably responsible for the fact that we cannot fit these seismograms using the simple path integral approximation. In total we fitted 217 seismograms, associated to 49 earthquakes. These seismograms yielded 920 linear constraints with a useful error on the 3-D S wave velocity below Europe.

Chapter 7

Partitioned waveform inversion: results for Europe

7.1 Introduction

In this chapter we describe the second step of the method of Partitioned Waveform Inversion (PWI): the inversion of the linear constraints which were obtained by non-linear inversion of many different seismograms. This is the first application of the method to obtain a three dimensional (3-D) velocity model. Nolet (1990) applied the method successfully to derive a 2-D model for the S wave velocity below the NARS array in western Europe. He fitted waveforms of teleseismic S body waves for frequencies as high as 50 mHz with a 2-D model with velocity perturbations up to 6%. In the previous chapter, we showed that we were able to fit many S body waves on regional seismograms for frequencies as high as 60 mHz with an average 1-D velocity model for the wave path. An important question in this study is whether we obtain, from the inversion of the linear constraints, a realistic 3-D model that fits the waveforms for these frequencies. If effects of scattering and out-of-plane propagation of seismic waves become predominant at these frequencies, we expect inconsistencies between the linear constraints and bad fits of the predictions by the 3-D model to the observations. Another question in this study is what resolution we can obtain with this method.

First, we describe how we obtained the 3-D model for the S wave velocity below Europe. Then, we discuss the fits of the waveforms predicted by the 3-D model to the observed seismograms. The 3-D model is presented by horizontal cross sections through the model. We compare the model with the result of the inversion of ISC S delays, which was presented in chapter 3.

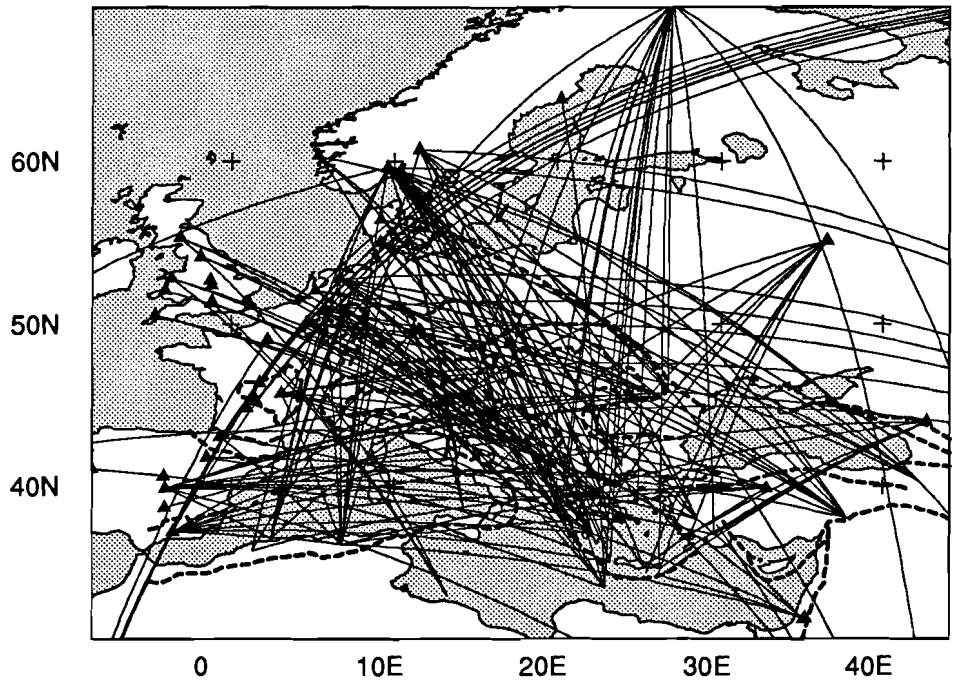

Figure 7.1. Wave paths used in this study.

Because the non-linear inversion of the waveform data results in (linear) path integrals of the velocity, we can easily perform a simultaneous inversion with the phase velocity measurements of chapter 4. In appendix 1 of this chapter we present the result of this combined inversion.

Vertical cross sections through the model are shown in the last chapter. In that chapter, we also compare the S velocity model with results of studies of the P wave velocity in Europe's upper mantle.

7.2 Parameterization of the model

The non-linear inversion of 217 seismograms resulted in 920 linear constraints on the S wave velocity below Europe. To invert the constraints for 3-D variations in the S wave velocity, we parameterized the volume of the Earth below the study region (figure 7.1) with a grid of cells. We use spherical coordinates, with the $\theta = 0$ axis orientated along the Earth's rotation axis, in the direction of the north pole. For horizontal coordinates θ and ϕ, the cells are rectangular. In θ–direction, the width of the cells is 1°. In the ϕ–direction the width of the cells varies with latitude in order to obtain cells with horizontal cross section equal to an area of 1° × 1° at the equator. In vertical direction, the model was

parameterized with triangular and boxcar functions. Similar to the parameterization in the non-linear inversion, we used two boxcar functions for the crust (0-29 km) and the lower mantle (670-2371 km), and eight triangular functions for the range in between with maxima at 29, 80, 140, 200, 300, 400-, 400+ and 670 km (see figure 5.1). The depths 400- and 400+ refer to the functions with maxima just above and just below the 400 km discontinuity. This parameterization results in 14510 cells. With 920 data and 14510 unknowns the model is strongly underdetermined. Overparameterization does not influence the resolution in the model, but damping is necessary to determine the model.

7.3 Inversion of the linear constraints

In chapter 5 the following matrix equation was derived for the inversion of the path integrals in the case of discrete parameterization:

$$\begin{bmatrix} \mathbf{A} \\ \alpha\mathbf{I} \\ \gamma_v \mathbf{G}_r \\ \gamma_h \mathbf{G}_\theta \\ \gamma_h \mathbf{G}_\phi \end{bmatrix} \mathbf{b} = \begin{bmatrix} \mathbf{q} \\ \mathbf{0} \\ \mathbf{0} \\ \mathbf{0} \\ \mathbf{0} \end{bmatrix} \tag{1}$$

A is the matrix that describes the relationship between the vector with path integral data **q** and the vector with the model parameters **b**. The matrices **I**, $\mathbf{G}_r$, $\mathbf{G}_\theta$ and $\mathbf{G}_\phi$ are damping matrices that yield the norm and the first order derivatives of **b** in the r, θ and ϕ direction. The solution of this matrix equation yields a minimum for the sum of the quadratic norm of the data misfit, and of the quadratic norms of the model and the model gradient. The parameters α, γ_v and γ_h control the trade-off between the data fit, norm of the model and the norm of the gradient of the model. Equation (1) is solved with the LSQR algorithm (Paige and Saunders, 1982) using as many iterations as necessary to achieve convergence to the damped solution. To minimize the influence of differences in cell volume on the damping of the solution, the columns of the matrix in (1), which relate to a particular cell, are scaled with the square root of the volume of the corresponding cell (Spakman and Nolet, 1988). Paths that are partly outside the study region sample structures that are not parameterized by cells. The cells on the boundary of the cell model that are sampled by these paths are used to absorb the average structure outside the cell model.

We determined the values of the damping parameters in (1) in a subjective way. We wanted to obtain, by using gradient damping, a smooth 3-D model that predicts the observed waveforms. At the same time, damping should reduce the propagation of data errors. In order to assess the effects of error propagation we performed inversions with synthetic data that simulate the uncertainties in the real data. For each fitted seismogram the uncertainties in the data were determined by equation (15) in chapter 5 as the maximum deviations of the path integrals that still yield an acceptable fit of the predicted to the observed waveforms. Because these uncertainties have the character of hard rather than soft boundaries the synthetic data consisted of random noise with a uniform distribution on

the interval between the maximum admissible variations of the path integrals.

By inverting the linear constraints with different values of the damping parameters, monitoring the fits and the propagation of data errors in the model parameters by inverting random noise, we arrived at a model that satisfies the above mentioned criteria best.

To obtain the final model we applied norm and gradient damping. We applied stronger constraints on the smoothness in horizontal directions than in vertical direction by taking a larger value for γ_h than for γ_v. We used a larger value for γ_h for the depth range 200-400 km than for shallower depths. It was possible to make the model smoother at larger depths because the resolution decreases below 200 km. This is due to the fact that a number of records are at small epicentral distance: these records lack the S wave, and the fundamental mode Rayleigh wave at 100 s is not sensitive to structures below 200 km. An even larger value for γ_h was taken for depths below the 400 discontinuity. The inversion of random noise yielded anomalies below 35m/s, which is well below the amplitude of the prominent anomalies in the final model.

7.4 Fits for the 3-D model

We use the term "final fit" for the fit of the waveform predicted by the 3-D model to the observation. As in chapter 6, the terms "initial fit" and "individual fit" refer to the fit of the waveform predicted by the starting model in the first step of the PWI and to the fit obtained after the non-linear inversion for an average model of the wave path, respectively. In general we found good agreement between the observed waveforms and the predictions by the 3-D model. We grouped the records according to misfit. We measured the misfit of a wave by the difference between predicted and observed arrival time divided by the predicted arrival time. In case of a positive deflection this is the difference between predicted and observed upward swing and vice versa. As an example we discuss the upper record (13) in figure 7.2. The first, positive, deflection of the S wave shows a difference between predicted (dashed) and observed (solid) waveform of 0.8% of the predicted arrival time; the differences between the other positive and negative deflections of the S wave are smaller. The difference between the first positive deflection of the predicted and observed Rayleigh wave is 0.5%, but the difference between the second positive deflection of the predicted and observed Rayleigh wave is 0.7%. According to our definition, the misfit for the S wave and Rayleigh wave is 0.8% and 0.7%, respectively. The largest value for the misfit of the waves on the seismogram was taken as the misfit for the record. In the above described example the misfit of the record is 0.8%. In table 7.1 the records are grouped according to misfit.

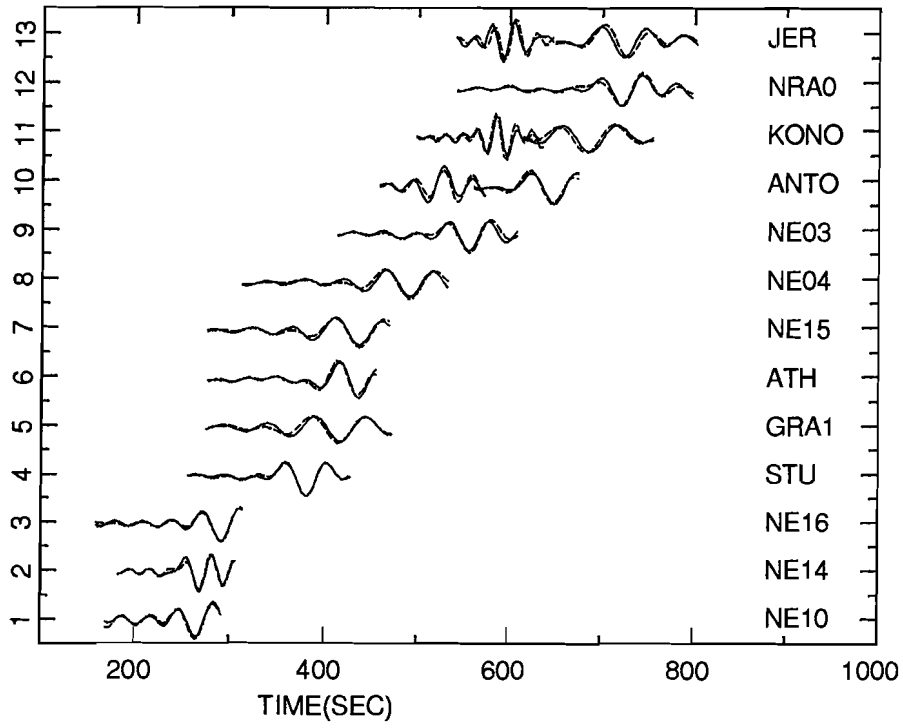

Figure 7.2. Observed waveforms (solid) of the Algeria event on October 27th, 1985, and predictions by the final 3-D model (dashed).

Table 7.1

perc. of total number of records	largest time misfit
62%	<0.3%
10%	0.3-0.5%
18%	0.5-1.0%
10%	>1.0%

For most of the records in the last group the predicted waveforms are similar to the observations but show a misfit in arrival time. This group also contains the records for which the predicted waveform differs from the observed waveform.

We show the final fits for the events of which the individual fits were shown in chapter 6. Figure 7.2 shows the final fits to the records of the event in Algeria (36.43N, 6.78E) on October 27, 1985. Most of the seismograms are modelled well by the 3-D model. The misfit for the record at station JER was discussed above. The misfit of the Rayleigh wave at KONO is between 0.5% and 0.3%. Figure 7.3 shows the final fits for the records of the

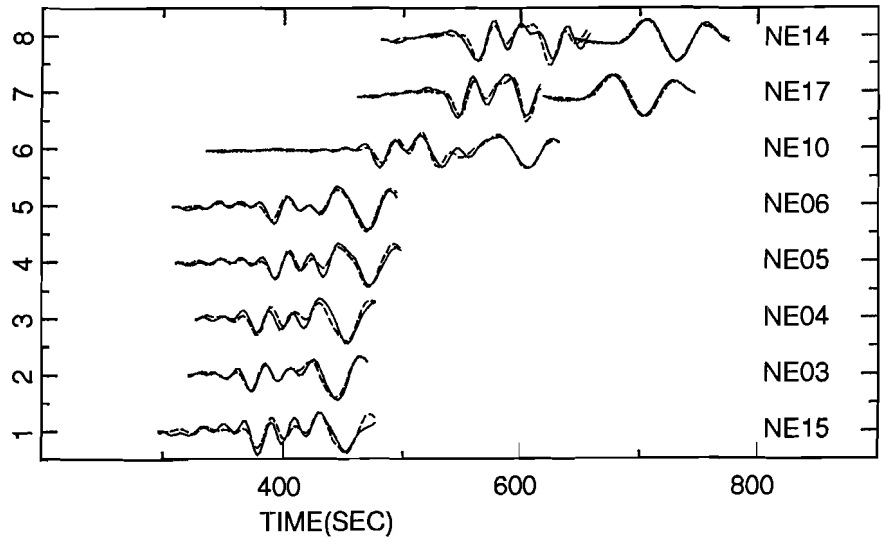

Figure 7.3. Observed waveforms (solid) of the Romania event on August 30th, 1986, and predictions by the final 3-D model (dashed).

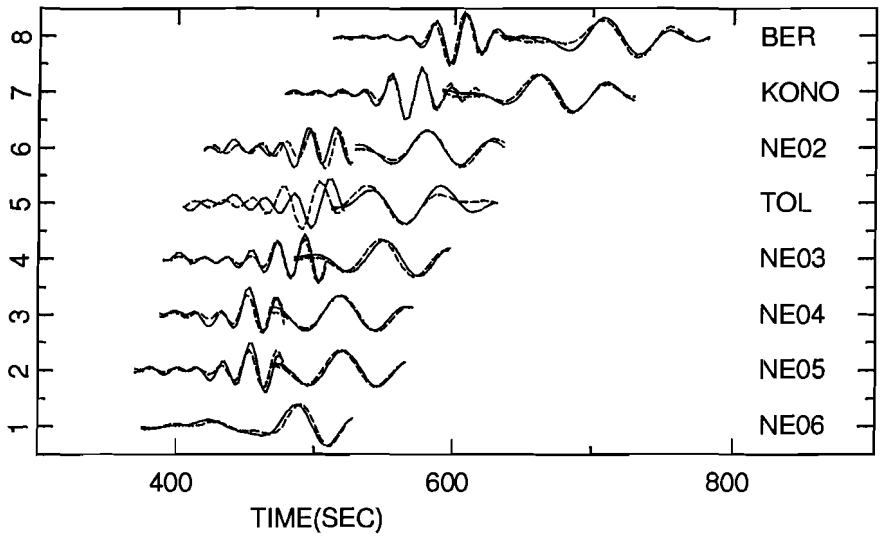

Figure 7.4. Observed waveforms (solid) of the Greek event on March 23, 1983, and predictions by the final 3-D model (dashed).

event in Romania (45.54N, 26.31E) on August 30, 1986. The misfits for the Rayleigh waves at the stations NE03 and NE04 are around 0.5%; the misfit for the Rayleigh wave at

NE05 and the S wave at NE17 is between 0.3 and 0.5%. In general the final fits of this event are good. Figure 7.4 shows the final fits for the earthquake in Greece (38.29N, 20.26E) on 23 March 1983. There are some small misfits in the records of this event; a large misfit of more than 1% is observed for the S wave at station TOL.

In order to investigate possible relationships between poor final fits and local Earth structure, we plotted the wave paths corresponding to seismograms for which the Rayleigh wave shows a misfit larger than 1.0% (solid line), and between 0.5%-1.0% (dotted line) in figure 7.5. Figure 7.6 shows a similar plot for the misfits of the S waves. Many wave paths from Greece to northwestern Europe show a misfit in the Rayleigh wave. However, this is also the region with the highest density of wave paths, and therefore we cannot conclude from figure 7.5 that Earth structure in the region between Greece and northwestern Europe is responsible for the high number of misfits of Rayleigh waves. Figure 7.6 shows that many paths from events in Greece and Turkey to stations on the Iberian Peninsula have large misfits for the S waves. In the following we discuss possible causes of bad final fits.

The path integral approximation. The basic assumption underlying the PWI as applied in this study is that waveforms are influenced only by Earth structure in the diametric plane. Lateral heterogeneity can cause out-of-plane propagation and scattering. If these phenomena affect the waveforms within the frequency band considered, they cause errors in the path integrals of the velocity between the source and receiver. As a consequence, we end up with inconsistent linear constraints on the 3-D velocity model, and a worse fit between the waveforms predicted by the 3-D model and the observations.

We believe that strong lateral heterogeneity is the cause of S wave misfits for paths in the Mediterranean. For a significant number of records of events in Greece and Turkey at stations on the Iberian Peninsula we could not fit the S wave in the first step of the PWI (see figure 6.9), neither with PREM nor with EUR as starting model. In the cases where we could fit S waves for paths in this region, we obtained widely differing 1-D average velocity models, especially in the depth range 200-670 km. For some paths we obtained velocity perturbations between 0 and -1.5% with respect to the starting model in this depth range, for other paths perturbations of -5%. The fact that the non-linear inversion resulted in widely differing 1-D velocity models and that the linear constraints are apparently inconsistent indicates that strong lateral heterogeneity causes the poor final fits for paths in the Mediterranean.

Focal parameters. Seismograms are inverted under the assumption that the hypocenter location and the focal mechanism are accurate. Errors in these parameters propagate into the values for the path integrals. We anticipate that errors in the epicenter coordinates are small because all events are of Mb $\geq$ 4.7 and the station distribution in Europe is good. As an indication of the magnitude of errors in the epicenter location we checked the difference between the PDE and ISC locations for a number of events with magnitude Mb $\approx$ 5. For most events, the difference was less than a few kilometers, which implies an error of less than 0.3% at an epicentral distance of 1200 km. For one event we observed a difference of 10 km, which would result in an error in the arrival time of 0.8% at 1200 km, of 0.4% at

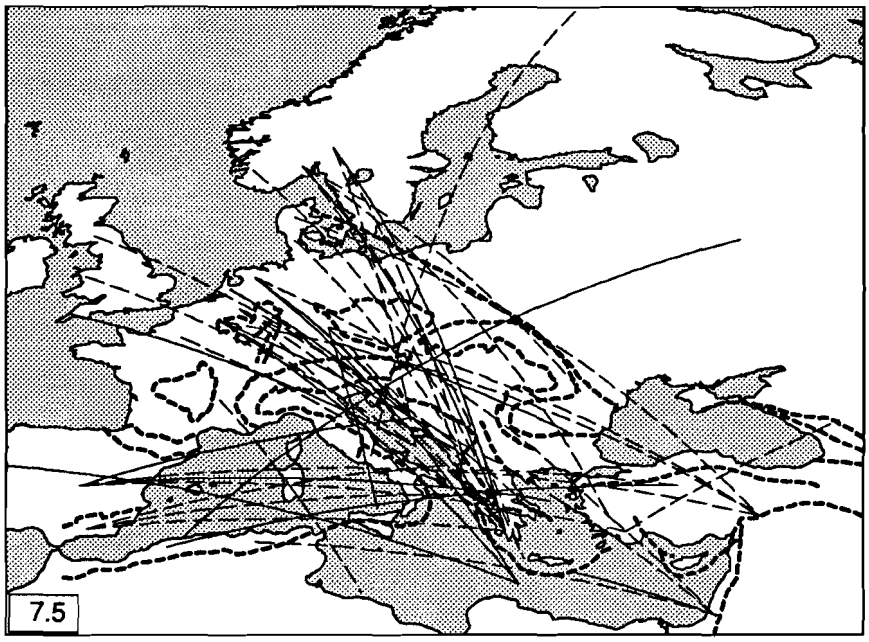

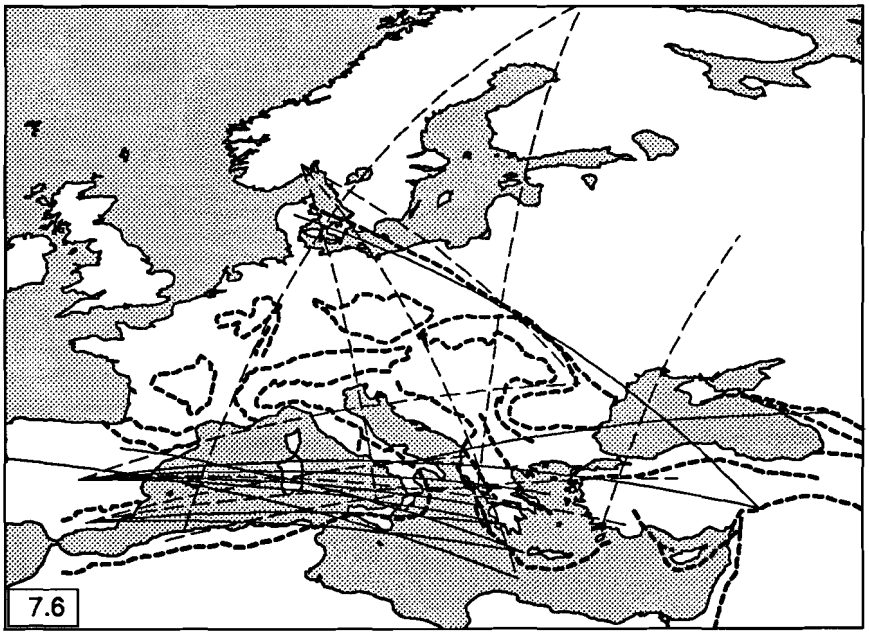

Figure 7.5. Wave paths for which the error in the predicted arrival time of the Rayleigh wave is larger than 1% (solid) and between 0.5% and 1% (dashed) of the predicted arrival time.

Figure 7.6. Wave paths for which the error in the predicted arrival time of the S wave is larger than 1% (solid) and between 0.5% and 1% (dashed) of the predicted arrival time.

2500 km. For nine events we used the location published in the PDE bulletins, because no ISC location had been reported yet. There can be large discrepancies in the hypocenter location published by the ISC and the PDE bulletins (Paulssen, 1987). During the inversions for a 3-D model we rejected the data of a Turkish event for which we had used the PDE location. The fits of the various 3-D models to the records of this event were consistently bad and we suspected the PDE location to be inaccurate. We assume to have excluded events with large errors in the reported focal depth from our data set by checking the initial fits. There is one event for which the poor final fits may be caused by an inaccurate focal mechanism. The individual fits for this event were discussed in chapter 6. Three different mechanisms were reported for this event (table 6.3); we used the HRVD mechanism because it resulted in the best individual fits (figure 6.7). The final fits to the 3-D model (shown in figure 7.7) are, however, quite disappointing. The predicted S waveform at stations NE14 and NE11 does not resemble the observation; the Rayleigh wave at stations BER and KONO show a misfit in the arrival time of more than 1% of the arrival time.

Crustal thickness. In the first step of the PWI, we used PREM, which has a 24.4 km thick crust, as starting model for some wave paths. For the inversion of the linear constraints, we used model EUR, which has a 29 km thick crust, as reference model. Consequently, all predictions by the 3-D model are calculated from a model with a 29 km thick crust. This might result in a worse final fit for paths in regions with a thinner crust. This effect mainly concerns the Rayleigh waves for wave paths in the western Mediterranean, since for most of these paths PREM was the starting model in the non-linear inversion. Note that this misfit is only an artifact of our procedure to check the final fits, and does not indicate a breakdown of the path integral assumption or of our linearization with respect to crustal thickness.

Estimates of the acceptable misfit level ε. The gradient damping puts constraints on the horizontal smoothness of the solution. Locally, this might yield a model that is too smooth compared with the degree of lateral heterogeneity required by the linear constraints. By lowering the (subjectively determined) value of the acceptable misfit level ε we obtain more linear constraints, with a smaller error, for the same path. Since the matrix rows are weighted with this error, the minimisation of the sum of data misfit and norm of model and model gradient (equation 27, chapter 5) then results in a smaller misfit for the data of the particular wave path. For some records, lowering ε indeed improved the fit. After inversion of the linear constraints, we compared for each datum η_i the value of the residual $A_{ij}b_j - \eta_i$ with the subjectively determined error $\Delta\eta_i$. One would expect a bad final fit if the residuals of the data corresponding to a certain seismogram are much larger than the respective $\Delta\eta_i$. In contrast, we found in a significant number of cases that data having residuals larger than $\Delta\eta_i$ correspond to predicted waveforms that match the observations well. Apparently, the value adopted for ε was too low for these records. Also, the opposite was found: small residuals corresponding to poor final fits, indicating that the value for ε was too high. This indicates that there are several records for which we have too many

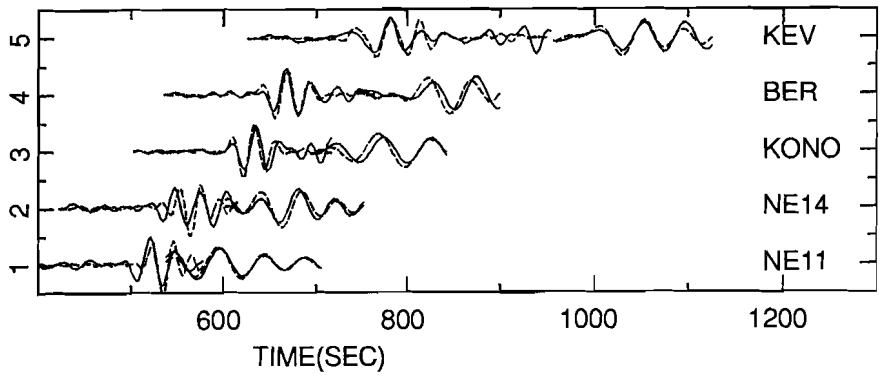

Figure 7.7. Observed waveforms (solid) of the Algeria event on October 27th, 1985, and predictions by the final 3-D model (dashed).

independent linear constraints, with too small errors. If this concerns very close wave paths this might result in inconsistent linear constraints for this part of the model and cause worse final fits. The apparent discrepancy between the subjectively determined misfit level ε and the fit of the predicted to the observed waveform needs further investigation.

7.5 3-D model of the shear wave velocity

7.5.1 Presentation of the 3-D model

In the remaining part of this chapter we present the final model. In order to investigate the resolution we performed sensitivity tests. First, we present horizontal cross sections through the 3-D model along with the results of resolution tests. The velocity variations in the model are plotted as perturbations relative to the velocity of the reference model. To make a comparison between velocity variations and tectonic elements we indicated the outlines of major tectonic features with dashed lines. We compare the results with the model obtained from the inversion of ISC S delays in chapter 3. Hereafter, we refer to this model as EURS89B. Second, we present the model after crustal corrections have been applied. Third, we discuss the results and present the conclusions from this study. In appendix 1, we present the results of a combined inversion of the waveform data and the phase velocity data set that was inverted in chapter 4.

7.5.2 Resolution analysis

To investigate the reliability of the results, we used the sensitivity tests that are commonly used in tomographic studies (Spakman and Nolet, 1988). Artificial data, calculated from a known input model using (1), are inverted. The uncertainties in the real data are simulated by adding random noise to the synthetic data. The uncertainties in the real data were determined by equation (15) in chapter 5 as the maximum deviations of the

path integrals that still yield an acceptable fit of the predicted to the observed waveforms. Because these uncertainties have the character of hard rather than soft boundaries, random noise with a uniform distribution on the interval between the maximum admissible variations of the path integrals was added to the synthetic data. By comparing the recovered model with the input model, we assess the resolution.

We did a sensitivity test with a model with harmonic velocity variations. We chose the synthetic model in such a way that it enables us to assess the resolution of structures that seem meaningful in the final result. Figure 7.8 shows the anomalies of this harmonic input model at 14.5 km and 29 km depth. Figure 7.9 shows the anomaly pattern at 80 km and 140 km depth, which is shifted towards the east with respect to the pattern at 29 km by half a wavelength of the pattern. At 200 km, 300 km, and 400- km the pattern is similar to the pattern in figure 7.8 but the wavelength of the pattern is 1.4 times larger. At 400+ km and 670 km this pattern is translated by half a wavelength to the east with respect to the pattern in the previous cross sections. The result of the harmonic sensitivity tests is discussed along with the discussion of the final model.

There are, however, interesting anomalies in the final model that extend over cross sections belonging to different combinations or that are smaller than the wavelength of the harmonic input model. In order to investigate if such anomalies are resolved, we performed sensitivity tests with an input model consisting of a broad "spike" extending over the same cells as the anomalies of interest. In all spike sensitivity tests the input anomaly has an amplitude of 340 m/s. We remark here that the effect of gradient damping on the recovered model depends on the shape of the input anomaly. The following experiment demonstrates this. We performed two sensitivity tests: in one, the input model consisted of a beam shaped anomaly, for the other one we used a spike as input model. In both synthetic models the anomaly extends from 80 km to 140 km depth. The recovered anomalies at 80 km depth are displayed in figures 7.10a and 7.10b, respectively. The recovered amplitude for the spike anomaly is less than 65% of the recovered amplitude of the beam shaped anomaly. This is due to the fact that for the beam shaped anomaly, only one of the horizontal components of the gradient, the one perpendicular to the beam, is effective, while both horizontal components are effective for the spike. Thus, due to the influence of gradient damping, spike tests yield a more pessimistic impression of the resolution for those structures that are really elongated.

Van der Hilst et al. (1992) argue that the diagnostic value of sensitivity tests to assess the reliability of the results of delay time tomography studies is limited (see also chapter 3). Similar arguments limit the validity for assessing the reliability of the results obtained with the PWI. The synthetic data are not contaminated by errors due to hypocenter mislocation, erroneous focal mechanism, scattering or out-of-plane propagation. Also, the non-linear relation between velocity perturbations and waveform data is ignored in these tests. In order to assess the resolving power of the data set, we should perform a non-linear 3-D inversion of the data. This is impossible because it would require too much computational effort. Therefore we use these sensitivity tests to assess the resolution.

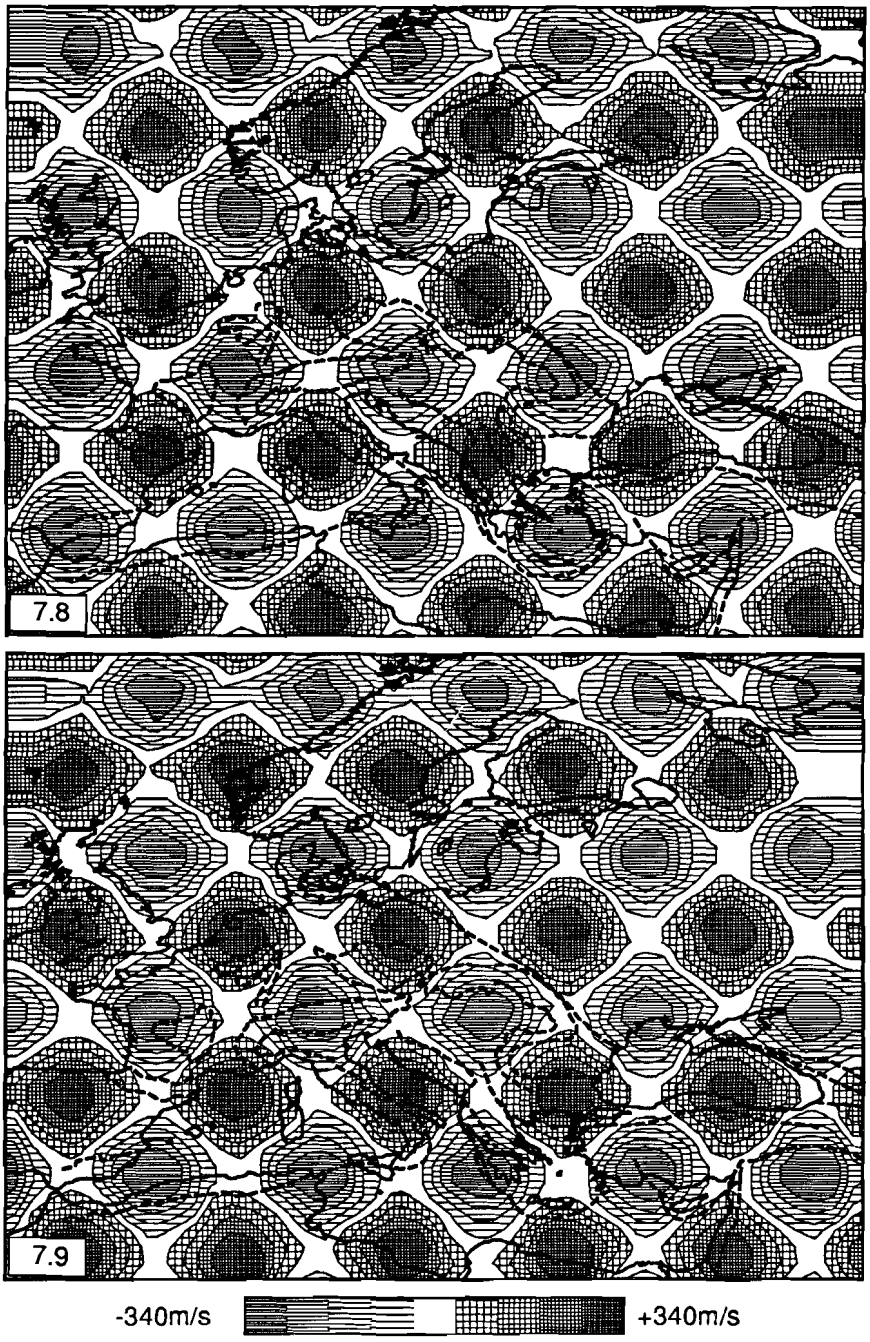

Figure 7.8. The harmonic input model for cross sections at 14.5 km and 29 km depth.
Figure 7.9. The harmonic input model for cross sections at 80 km and 140 km depth.

7.5.3 Horizontal cross sections at 14.5 km and 29 km depth

Figure 7.11a and 7.12a show the cross sections through the 3-D model at 14.5 km and 29 km depth respectively. Fig 7.11b and 7.12b show cross sections through the result of the harmonic sensitivity test at the same depths. We present the cross sections for the sake of completeness but we do not want to interpret them because variations in crustal thickness may affect the usefulness of the result at these depths.

7.5.4 Horizontal cross sections at 80 km and 140 km depth

Figures 7.13a and 7.14a show the horizontal cross sections at 80 km and 140 km depth respectively. The result of the harmonic sensitivity test (shown in figure 7.13b and 7.14b) indicate that the resolution in central and northwestern Europe is reasonable, but there is *leakage* (= smearing in vertical direction) from anomalies in neighbouring cross sections. Below the western Mediterranean smearing in east-to-west direction occurs. In northeastern Europe the sign of the recovered anomalies is equal to the sign of the input anomalies, but the recovered amplitudes are relatively small. Most wave paths in this region are in northwest-southeast or north-to-south direction, which causes smearing in these directions.

Figures 7.13a and 7.14a reveal the most prominent feature of the 3-D model: there is a sharp boundary between the Precambrian parts of Europe (the Baltic Shield, Russian Platform, and Ukraine Shield), which are characterized by high velocities, and the younger parts of Europe, which are characterized by lower velocities. The boundary coincides with the Tornquist-Teisseyre Zone (TTZ). The clear outline of the TTZ at these depths confirms Snieder's result (1988) which indicated the presence of a strong high velocity anomaly that coincides with the western boundary of the Russian Platform.

Low velocities are present below the Pannonian Basin. The harmonic sensitivity test indicates that this anomaly is resolved, although there is some smearing in northwest-southeast direction. Snieder's model (1988) supports the existence of this low velocity anomaly.

Below the western Mediterranean we find low velocities. The result of the harmonic test indicates that there is lack of resolving power in east-west direction, so the exact outline of this anomaly is not resolved. Also Berry and Knopoff (1967), Panza et al. (1980), Mariller and Mueller (1985), Calcagnile and Scarpa (1985), and Snieder (1988) report low velocities below the western Mediterranean.

The region south west of Massif Central is characterized by a low velocity anomaly. A spike test indicates that this anomaly is resolved (see figure 7.28a and 7.28b of appendix 2). Low velocities below this region are consistent with the S velocity models of Souriau (1981), Calcagnile and Scarpa (1985) and Snieder (1988).

At 80 km, a high velocity anomaly is present below the west coast of Greece, which extends further to the north at 140 km depth. This anomaly can be identified as the high velocity slab in the Hellenic subduction zone, which is imaged by Spakman (1988) and Spakman et al. (in preparation) using P delay-time tomography. Below Crete, the density

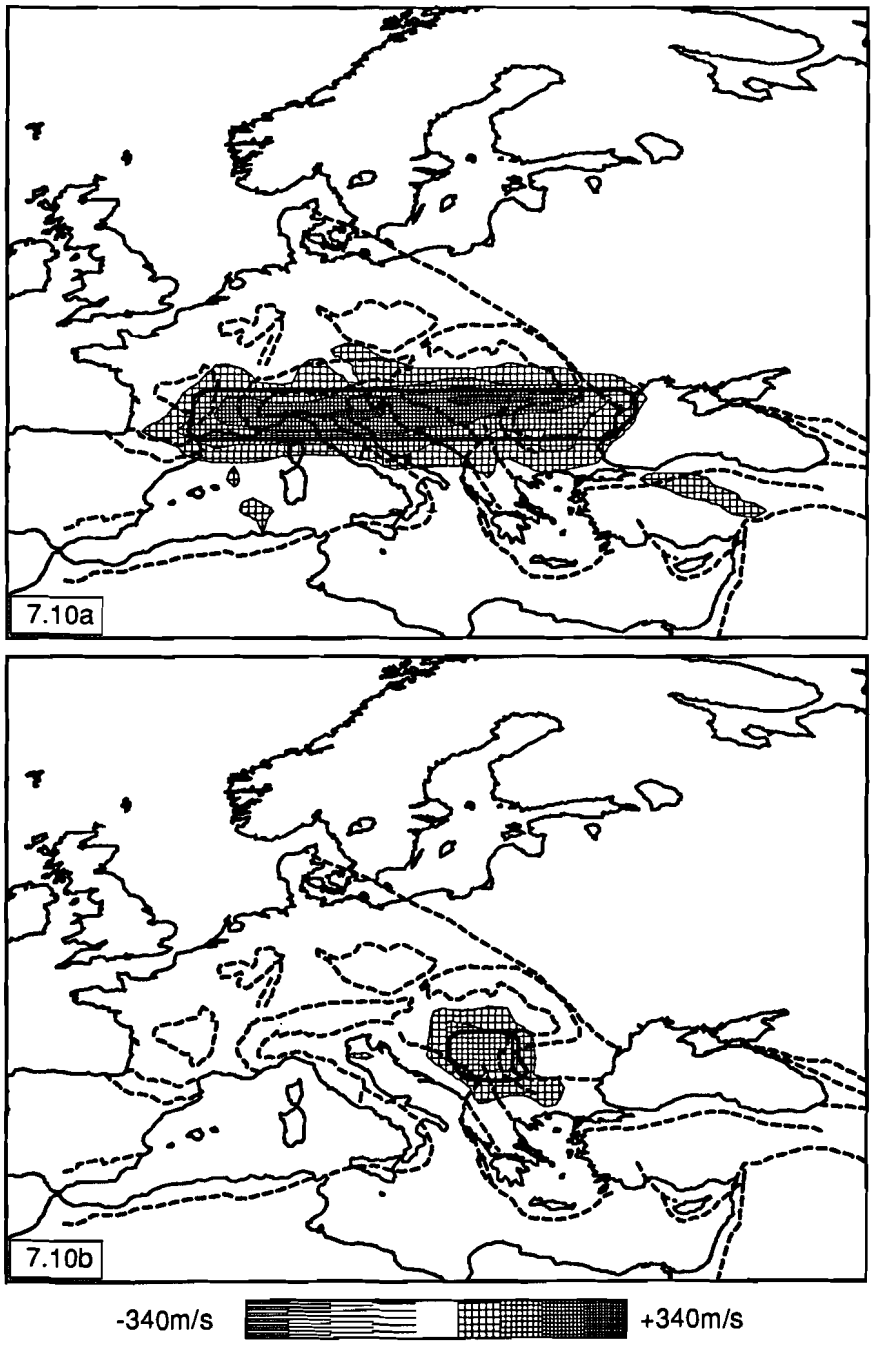

Figure 7.10. a) Recovered model from the sensitivity test with a beam shaped input model at 80 km depth. b) Recovered model from the sensitivity test with a spike input model. The contour of the input anomaly is indicated with a thick line.

of the wave paths is much lower than below the mainland of Greece, which results in poorer resolution for this region. This may explain why the high velocity slab does not extend below Crete in our results.

The region below Turkey and the northern Aegean Sea is characterized by low velocities. The result of the harmonic sensitivity test indicates that there is smearing in east west direction, but the northern boundary of this low velocity anomaly is resolved.

The Paris Basin shows up as a region with high velocities, which confirms a result from Souriau's study (1981).

Comparison with the model obtained from ISC S delays. Layer 3 (70-128 km) and 4 (128-242 km) of EURS89B cover the depth range discussed in this section. The two models differ remarkably with respect to the structure below the TTZ. Layer 3 of EURS89B shows low velocities on both sides of the TTZ, there are high velocity anomalies on a few locations below the Russian Platform and Baltic Shield in layer 4. According to the sensitivity tests (chapter 3), the resolution below the Russian Platform and Baltic Shield is good in layer 3 and reasonable in layer 4. The absence of high velocities might be caused by the fact that we excluded from the inversion data that have an absolute residual with respect to the travel time of the new reference model exceeding 6 s. A comparison between figure 2.9, which shows the S delays associated to rays located below the Baltic Shield, and figure 3.2, which shows the differential time curve of the reference model with respect to the J-B model, indicates that selection of a time window around the travel time of the new reference model leads to rejection of a number of large, negative, delays at epicentral distances smaller than 13°. Rays arriving at epicentral distances shorter than 13° bottom above 128 km depth (according to the new reference model) and therefore constrain the velocity at these depths. It is thus likely that below the Baltic Shield and the Russian Platform the solution is dominated by small, negative, or positive outliers for this region. Both models show low velocities below the Pannonian Basin. Below the western Mediterranean EURS89B indicates very weak low velocities in layer 3, in contrast with the strong low velocity anomaly in figure 7.13a-7.14a. Figure 7.13a-7.14a show low velocities *southeast* of Massif Central, whereas EURS89B indicates a low velocity anomaly *below* Massif Central. The waveform data do not sample the structure below Massif Central, so we cannot compare the models in this region. However, there is a clear discrepancy between the models with respect to the structure southeast of Massif Central. The high velocity slab below the Hellenic arc is visible in both models but the image differs with respect to details. EURS89B indicates high velocities below the Hellenic arc from the southern part of the mainland to Crete. Figures 7.13a and 7.14a show a high velocity anomaly extending from the southern part of the mainland to the north. We suspect that the absence of high velocities south of the mainland is caused by a decrease of resolution in this region. Both models indicate low velocities below the Aegean Sea and western Turkey.

7.5.5 Horizontal cross sections at 200 km, 300 km and 400- km

Figures 7.15a, 7.16a, and 7.17a show the cross sections through the 3-D model at 200 km, 300 km, and 400- km. Figures 7.15b, 7.16b and 7.17b show the corresponding cross sections through the result of the harmonic sensitivity test.

At 200 km, the model indicates that there is no velocity contrast below the central part of the TTZ, but the transition to higher velocities is located further to the east below the Russian Platform. The results of various sensitivity tests warn us that this result should be interpreted with caution. Figure 7.29a-7.29b (appendix 2) show the result of a sensitivity test with an input model consisting of a spike below the Black Sea extending from 200 km to 400+ km depth. This test indicates that there is a danger of smearing of the low velocity anomaly below Turkey which might cause the absence of high velocities below the western boundary of the Russian Platform at 200 km and 300 km depth.

At 400- km, a zone of low velocities extends east of the TTZ, below the western boundary of the Russian Platform. Since this anomaly continues at larger depth, it is discussed in the next section.

In contrast with the situation below the central part of the TTZ, the boundary between high velocities below the Baltic Shield and lower velocities below Denmark, Germany, and The Netherlands extends to 400 km depth below the northwestern end of the TTZ. We investigated the reliability of the high velocity anomaly at 300 km and 400- km depth below the Baltic Shield with a sensitivity test with an input model consisting of a spike of the width of the anomaly. The recovered model is displayed is figure 7.30a-7.30b. From this test we infer that the anomaly is resolved, although there is smearing in south east direction.

The high velocity anomaly below Greece, which is associated to the slab, continues at these depths.

Comparison with the model obtained from ISC S delays. Layers 4 (128-242 km), 5 (242-324 km) and 6 (324-405 km) of model EURS89B cover the depth range 200-400 km. With respect to the structure below the TTZ, we see only little agreement between the models. Below central and southern Europe there are similarities. Both models show high velocities below Italy. A high velocity anomaly below the Aegean Sea, which is the image of the subducting slab, is present in both results. The result of the waveform inversion indicates a low velocity anomaly below Yugoslavia, between 300-400 km depth (figure 7.16a-7.17a). EURS89B shows in layer 7 (405-490 km) a strong low velocity anomaly with the same lateral position. The difference in the depth of this anomaly is perhaps caused by a lack of depth resolution: modes cannot resolve the exact depth of the anomaly, and the linearization of the relationship between delay time data and anomalies might cause an error in the depth of the anomaly.

7.5.6 Horizontal cross sections at 400+ km and 670 km

The cross sections at 400+ km and 670 km depth are shown in figures 7.18a and 7.19a. The result of the harmonic sensitivity test, displayed in figures 7.18b and 7.19b, shows that

in northwestern Europe the sign of the recovered anomalies is consistent with the sign of the input anomalies, but the resolved amplitudes are very small. Below the western Mediterranean, smearing in east-to-west direction is strong.

Figures 7.18a and 7.19a show that the zone of low velocities, which becomes a prominent anomaly at 400- km depth, continues at 400+ km and 670 km. The result of the sensitivity test with a spike below the Black Sea (displayed in figures 7.29a-7.29d, appendix 2) indicates that at 400+ km depth there is some smearing of the low velocity anomaly below the Black Sea in the direction parallel to the TTZ and in northeastern direction. This test also indicates that smearing is not responsible for the low velocity anomaly below Poland and the Baltic Republics. A sensitivity test with a spike below this region shows that this low velocity anomaly is resolved (see figures 7.31a and 7.31b, appendix 2).

Below the northern Aegean Sea the high velocity slab extends to 670 km. From 400-km depth, high velocities appear below the Pannonian Basin.

The model shows that even at the depth of the 400 km discontinuity, velocity perturbations of a few percent are necessary to explain the observations.

Comparison with the model obtained from ISC S delays. Layers 7 (405-490 km), 8 (490-575 km) and 9 (575-660 km) cover the transition zone. In both models the resolution below the TTZ is not very good at these depths, yet there are some similarities. The result from the waveform inversion indicates a zone of low velocities east of the TTZ, and EURS89B shows weak low velocity anomalies below the western boundary of the Russian Platform, the Black Sea and the Baltic Sea in layer 8 and 9. EURS89B shows a strong high velocity anomaly below the Carpathians between 490-575 km. The result from the waveform inversion also has high velocities below the Carpathians below the 400 km discontinuity (figure 7.18a) but this anomaly extends to shallower depths of approximately 300 km. The image of the high velocity slab is present in both models. Both models show a high velocity anomaly below the northern Aegean Sea, which is the image of the subducting slab.

Figures 7.11 - 7.19 (next 9 pages). For each figure: a) S velocity model, b) model recovered from the harmonic sensitivity test. Depth of the section and reference velocity are indicated at the top of each figure.

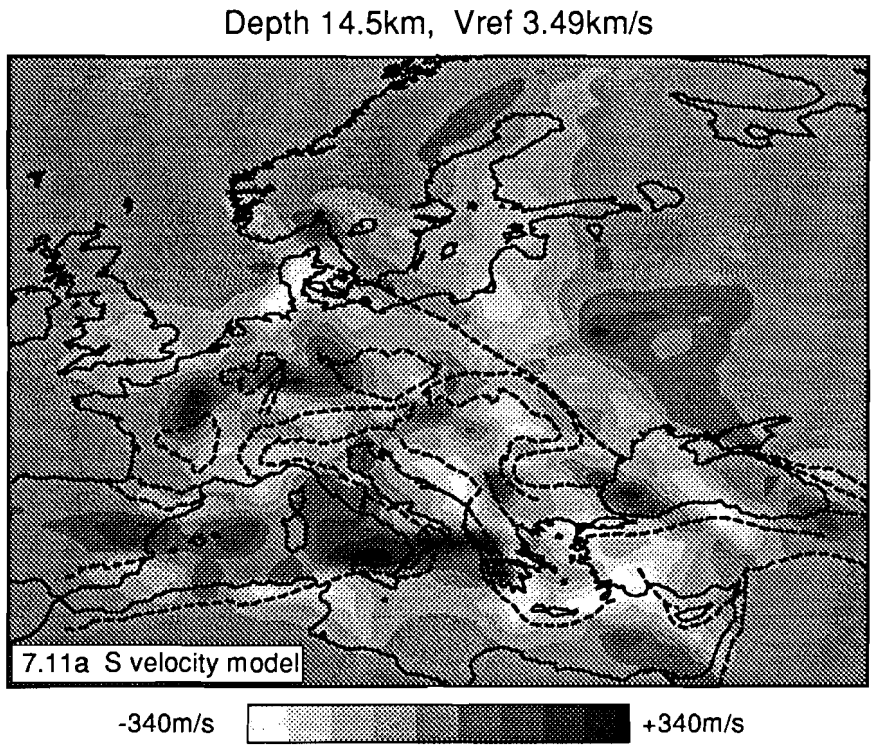
Depth 14.5km, Vref 3.49km/s
7.11a S velocity model
-340m/s
+340m/s

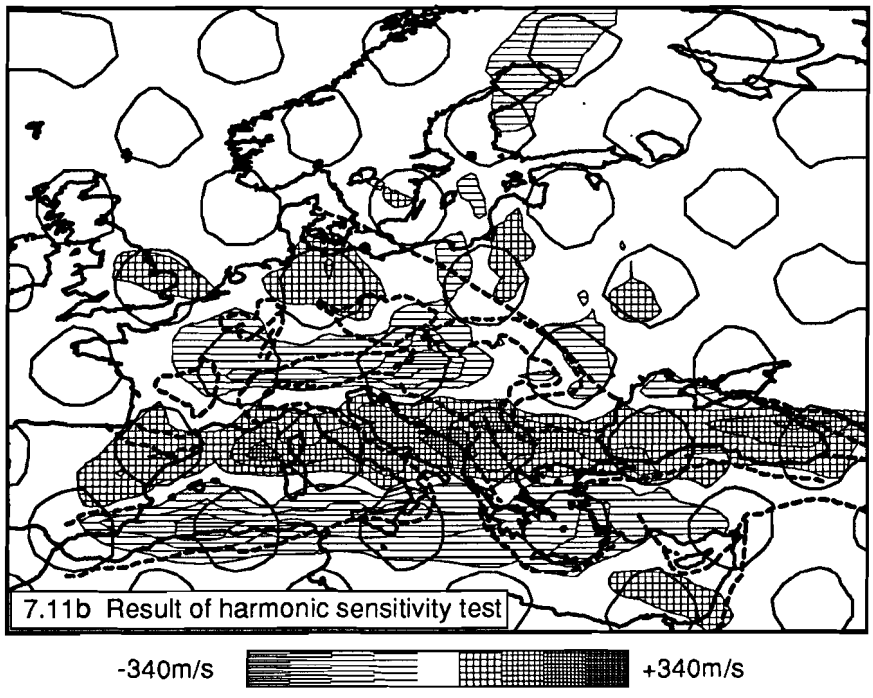
7.11b Result of harmonic sensitivity test
-340m/s
+340m/s

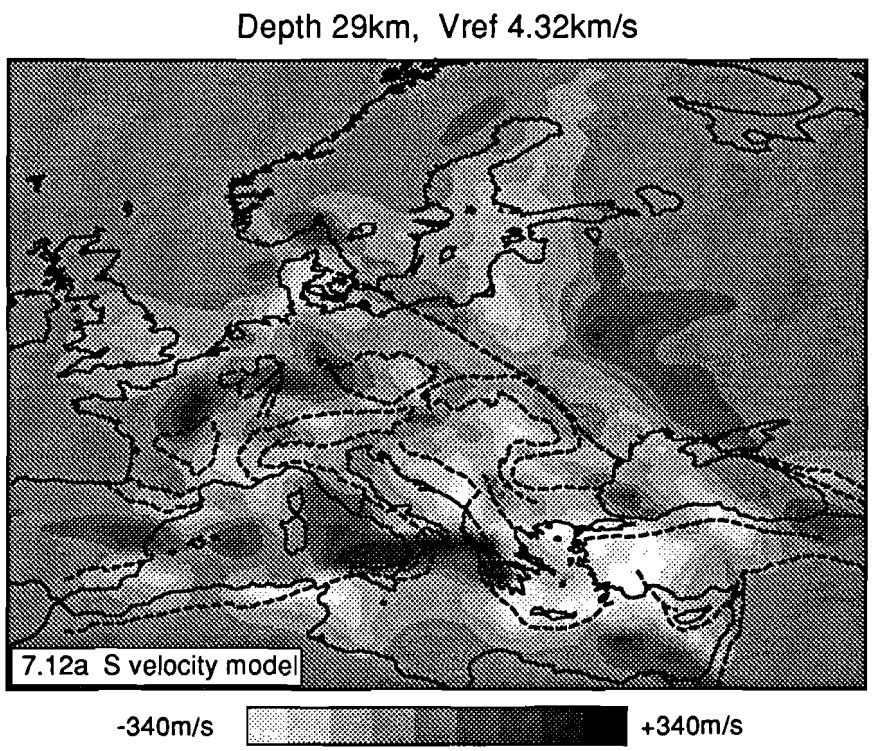
Depth 29km, Vref 4.32km/s
7.12a S velocity model
-340m/s
+340m/s

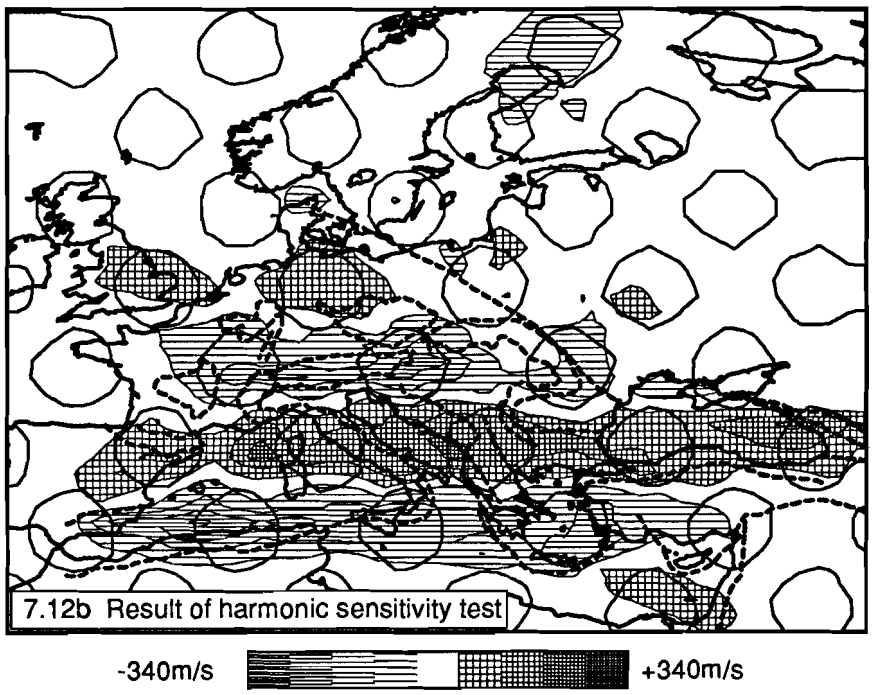
7.12b Result of harmonic sensitivity test
-340m/s
+340m/s

Depth 80km, Vref 4.5km/s

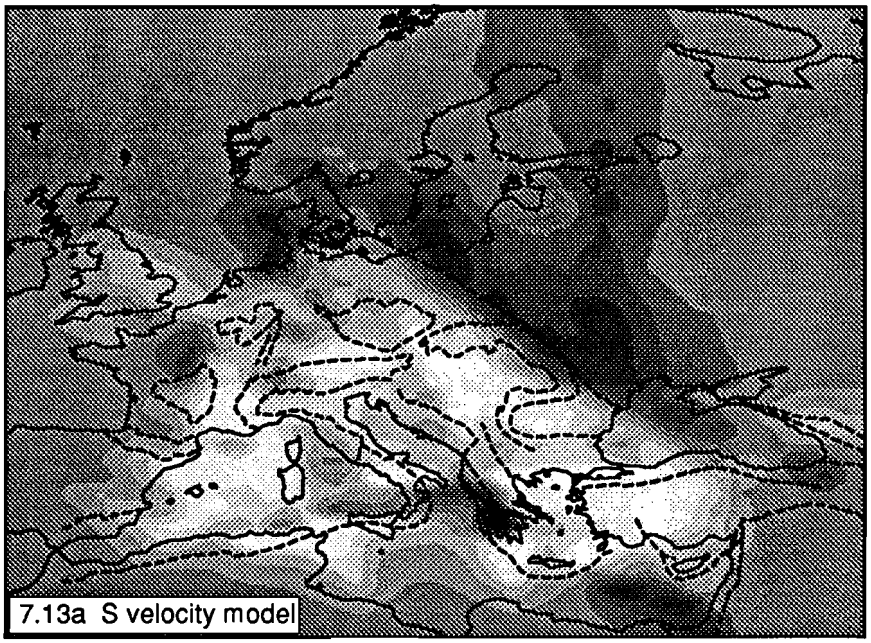

7.13a S velocity model

-340m/s +340m/s

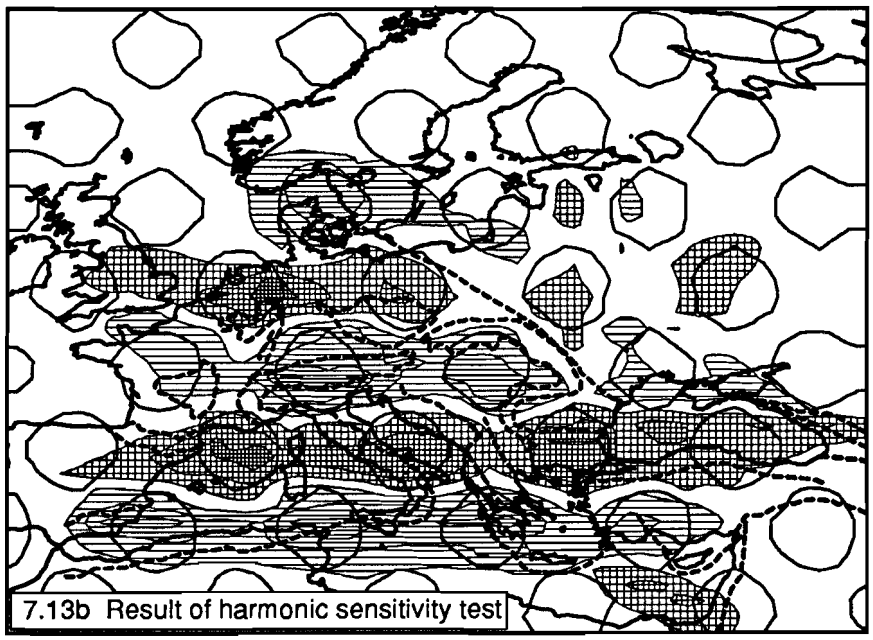

7.13b Result of harmonic sensitivity test

-340m/s +340m/s

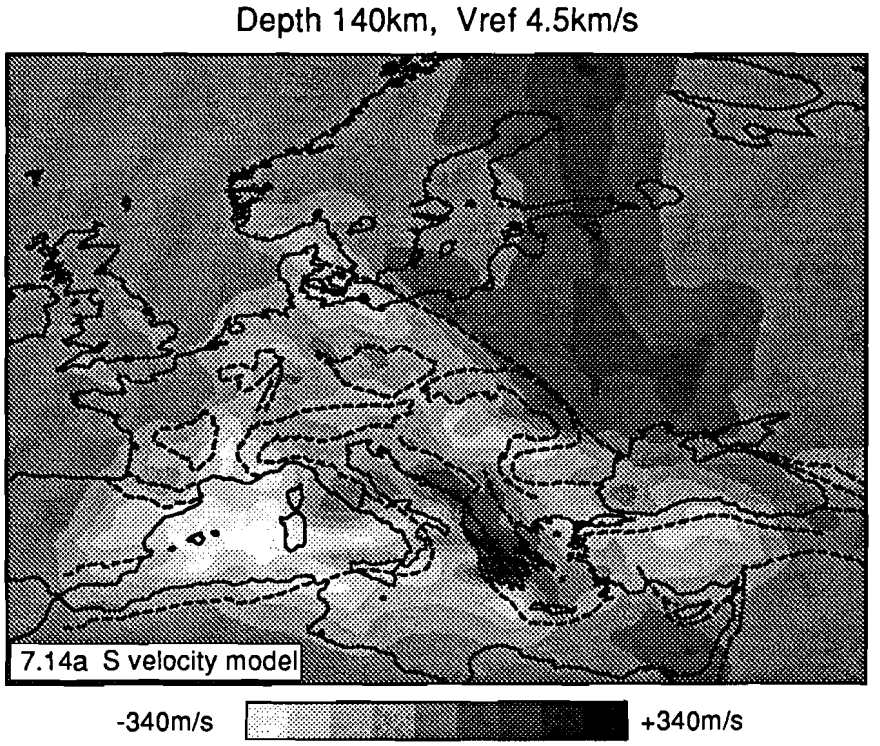
Depth 140km, Vref 4.5km/s
7.14a S velocity model
-340m/s
+340m/s

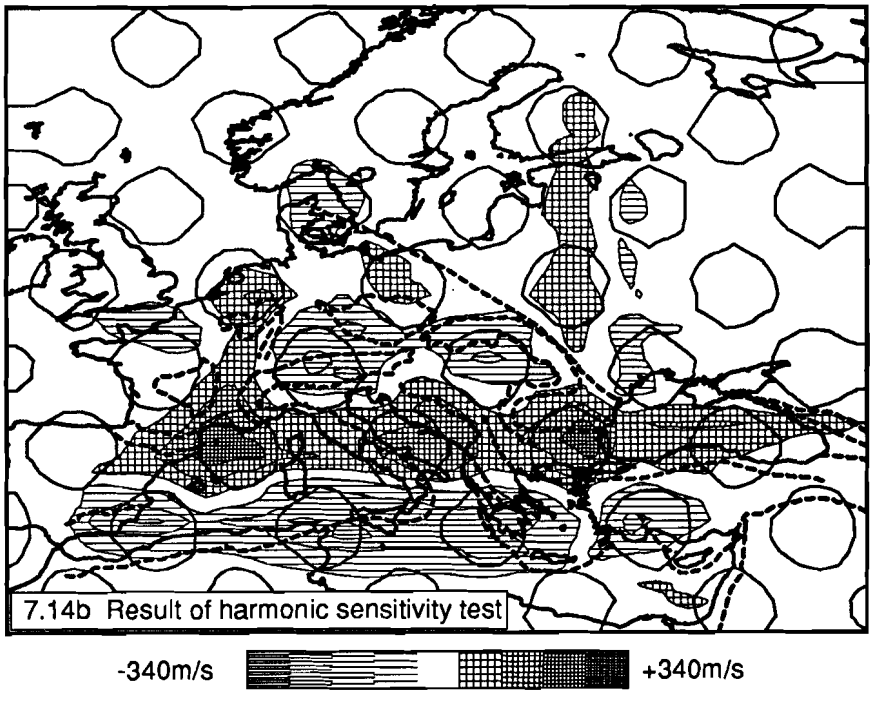
7.14b Result of harmonic sensitivity test
-340m/s
+340m/s

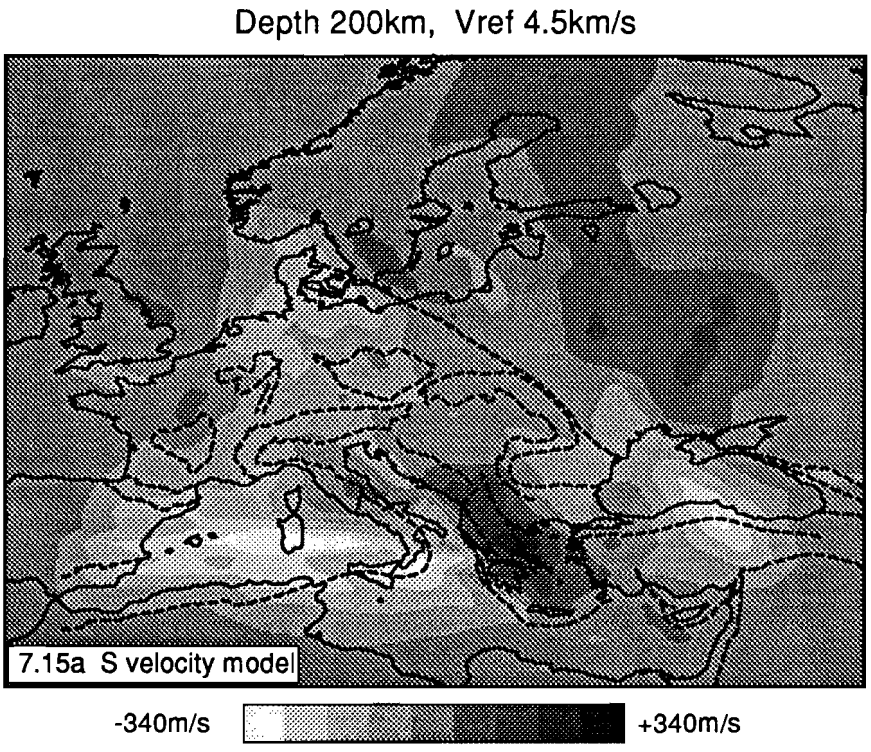
Depth 200km, Vref 4.5km/s
7.15a S velocity model
-340m/s
+340m/s

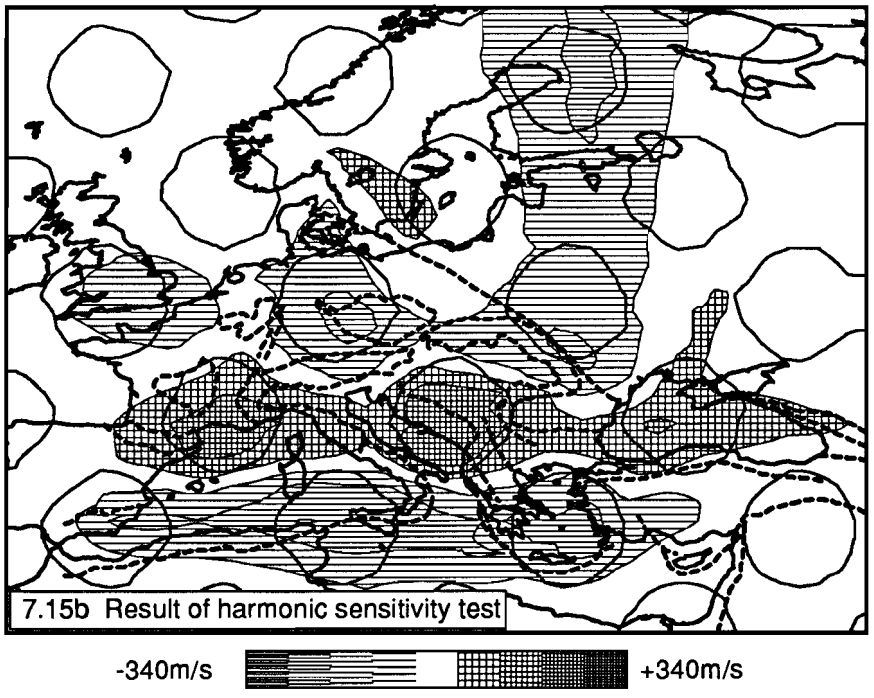
7.15b Result of harmonic sensitivity test
-340m/s
+340m/s

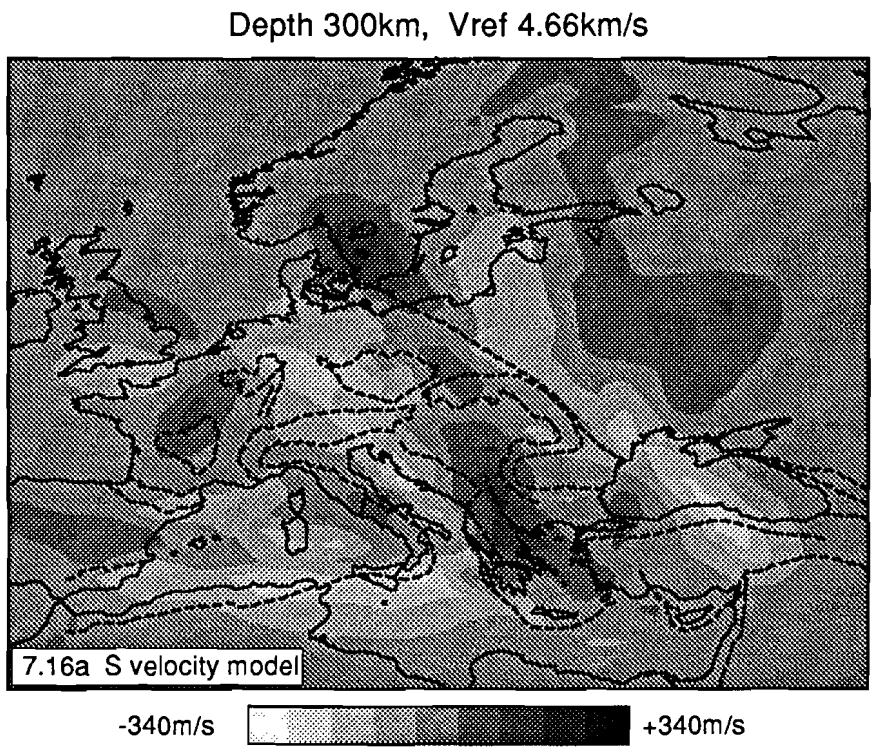
Depth 300km, Vref 4.66km/s
7.16a S velocity model
-340m/s
+340m/s

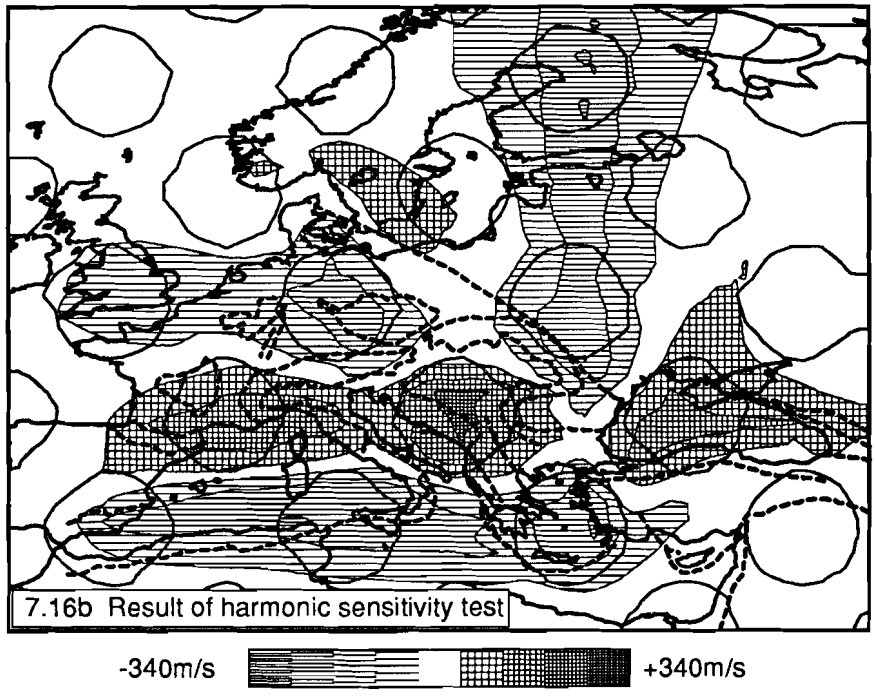
7.16b Result of harmonic sensitivity test
-340m/s
+340m/s

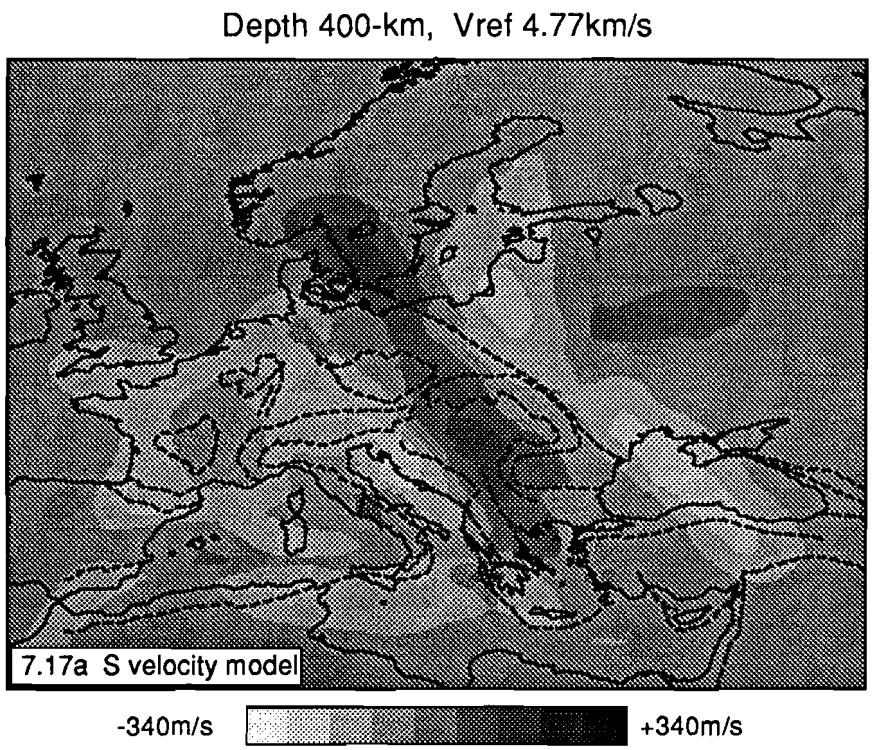
Depth 400-km, Vref 4.77km/s
7.17a S velocity model
-340m/s
+340m/s

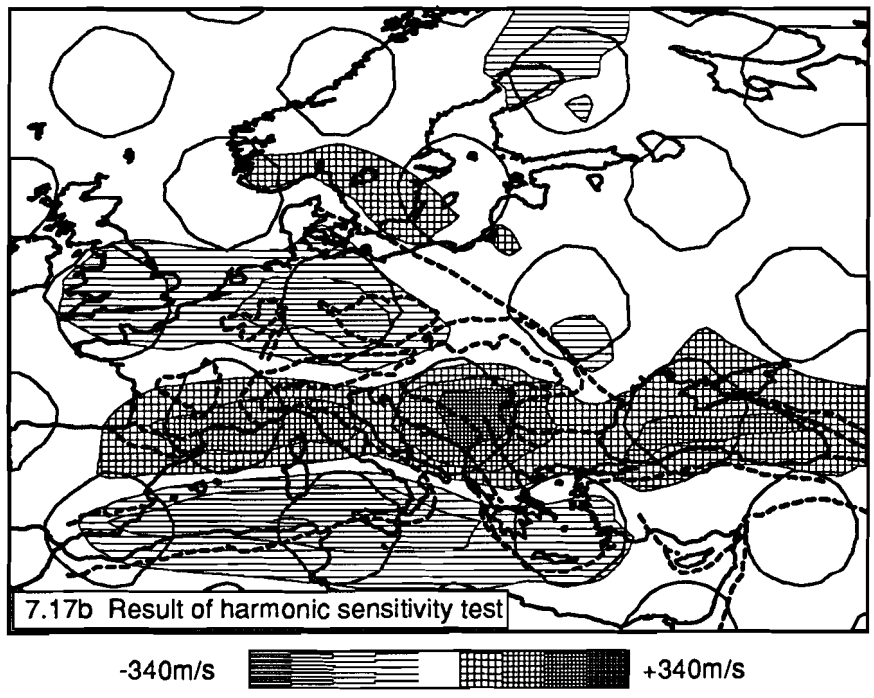
7.17b Result of harmonic sensitivity test
-340m/s
+340m/s

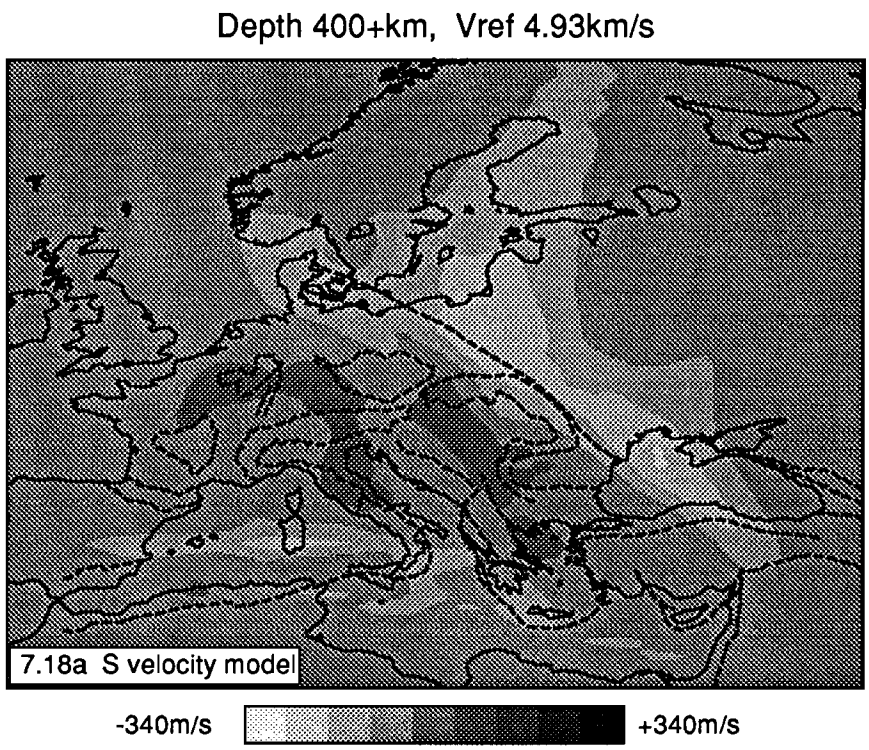
Depth 400+km, Vref 4.93km/s
7.18a S velocity model
-340m/s
+340m/s

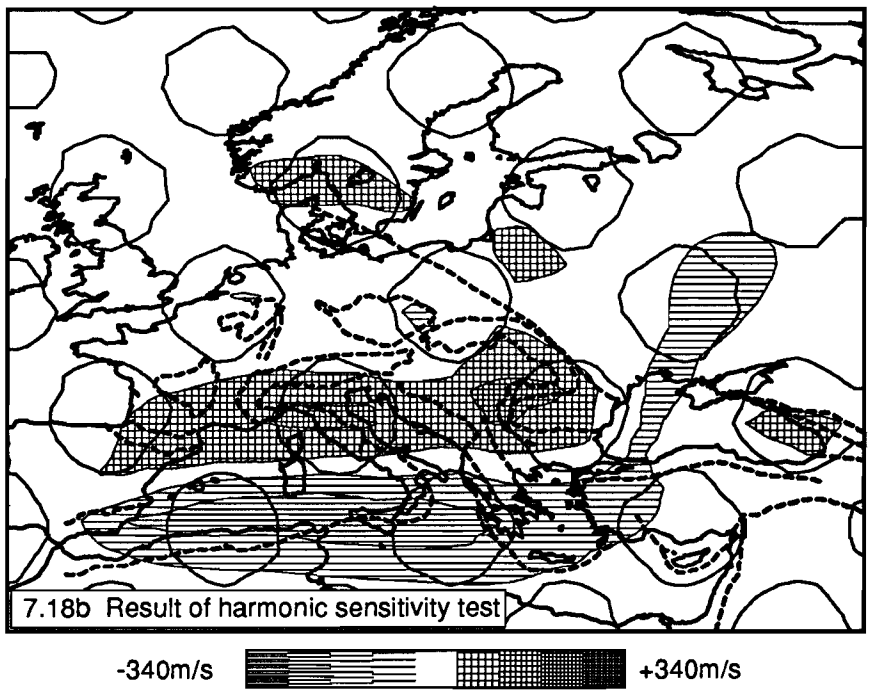
7.18b Result of harmonic sensitivity test
-340m/s
+340m/s

Depth 670km, Vref 5.57km/s

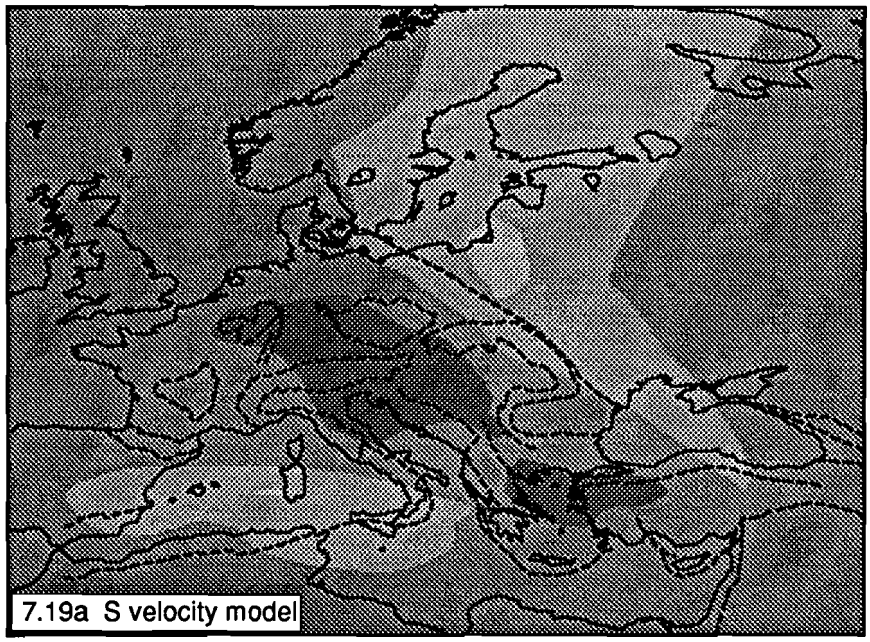

7.19a S velocity model

-340m/s +340m/s

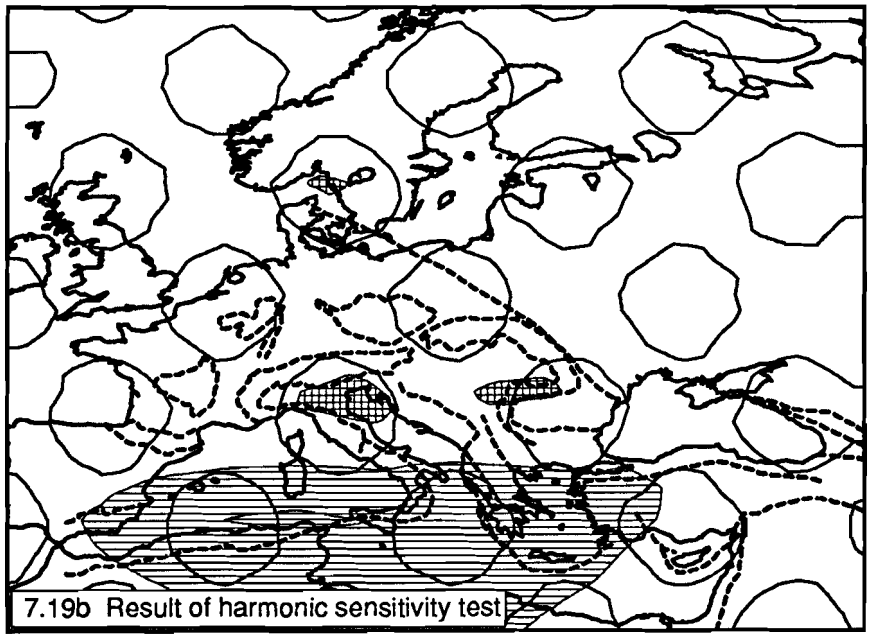

7.19b Result of harmonic sensitivity test

-340m/s +340m/s

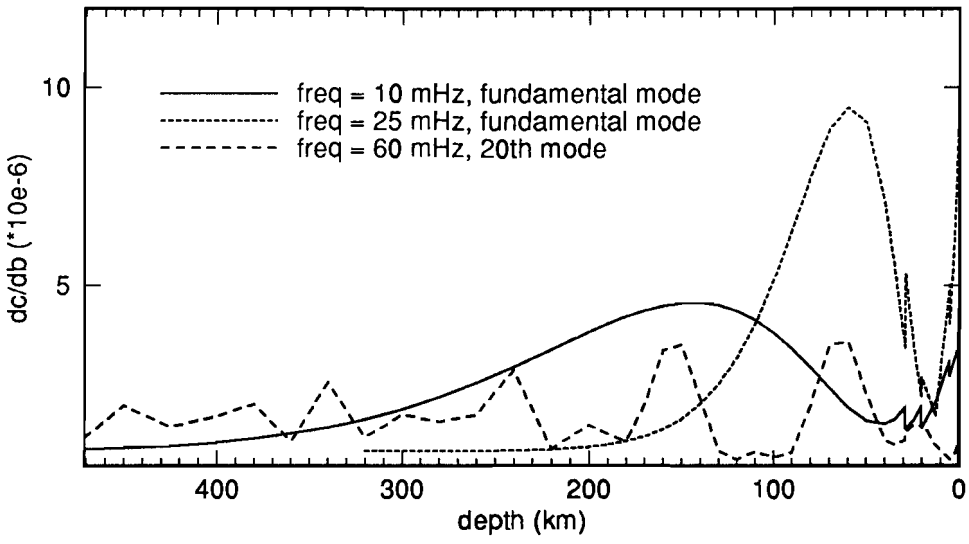

Figure 7.20. $\frac{\delta c}{\delta \beta}(r)$ for the fundamental mode of the Rayleigh wave for frequencies of 10 mHz and 25 mHz. These are the lowest and highest frequency that we used for the fundamental mode in this study and therefore the curves indicate the shallowest depth range for which the inversion is sensitive. Also, the curve for the 20th mode at 60 mHz is shown.

7.5.7 Crustal corrections

The phase velocity of the modes that we used in this study are mainly influenced by structures well below the Moho depth, but figure 7.20 shows that the phase velocity is, to a much lesser extent, also sensitive to structures at crustal depths. Thus, variations in crustal thickness affect the retrieved velocity perturbations at mantle depths. In an attempt to correct for this effect, we applied the same method as used in chapter 4 to correct the mantle velocity for the crustal thickness and velocity. From figure 7.20, we assumed that the retrieved mantle velocity below approximately 100 km depth is constrained by the fundamental mode at low frequencies and higher modes that are relatively insensitive to the Moho depth. Therefore, we decided to correct the mantle velocity at 29 km and 80 km depth. We assembled information about the crustal velocity and Moho depth from different sources (Henkel et al., 1990; Mostaanpour, 1984; the Moho map compiled by Giese and Mostaanpour (1989); and the following maps from the Geothermal Atlas of Europe: Depth of the Crust-Mantle Boundary, Average Velocities in the Consolidated Crust, Thickness of the Undeformed Sedimentary Cover). On the basis of this information, we corrected the mantle velocity perturbations such that, locally, the average velocity over the upper 140 km of the model remains the same. The corrections to the velocity perturbations increase

linearly from 0 at 140 km to maximum at the local Moho depth.

The resulting velocity perturbations are presented in figures 7.21 and 7.22. In general, the corrected anomalies are larger than the uncorrected. Most anomalies did not change in sign, but became larger in amplitude. However, the positive anomalies at 29 km depth in the western Mediterranean basin and the positive anomaly between Corsica and Italy at 29 and 80 km depth, became smaller in amplitude. The high velocity at 80 km depth below the Russian Platform has become even higher after the corrections.

Crustal corrections have the advantage that artifacts, introduced by variation in crustal thickness can be removed if sufficient information on Moho depth and crustal velocity is available, so that the final model is closer to reality in the upper layers. However, we realize that there are several shortcomings of this method to apply crustal corrections. (1) We are not confident that the information about the crustal thickness and velocity is everywhere correct because different sources give inconsistent information. Furthermore, there are gaps in our information, for instance about the crustal velocity in the western Mediterranean, parts of Baltic Shield and eastern Europe, so in many regions we had to interpolate over large distances. (2) Because the resolution in the crust is not very good, the anomalies in the 3-D model do not represent the true crustal velocity (or an average of the velocity in the upper 29 km of the Earth) in many regions. Applying corrections for crustal velocity and thickness may thus lead to an overcorrected model or wrongly corrected model. (3) We cannot check if the linear corrections are warranted. In chapter 4 we corrected a model obtained from fundamental mode phase velocities. It was easy to check if the corrected model resulted, locally, in the same phase velocity as the uncorrected model because it is easy to find the phase velocity of the fundamental mode. It would be an extremely laborious task to check this for 20 modes. Because of the shortcomings of the method to apply crustal corrections, we prefer to interpret the uncorrected model.

7.6 Discussion

Inversion of the linear constraints resulted in a 3-D model with realistic velocity variations that generally matches the observations well. There are a few aspects of the method that need further investigation.

The method applied to correct for crustal corrections has several shortcomings. It should be investigated if the effect of varying crustal thickness on the retrieved velocity variations should be incorporated in the non-linear inversion.

This study revealed that in the western Mediterranean lateral heterogeneity is so strong that the path integral approximation is probably not valid. To image the velocity in these regions, effects of scattering and out-of-plane propagation of the direct wave have to be modelled.

The 3-D model for the S velocity is in agreement with results of many surface wave studies. The model strongly confirms the conclusions of Paulssen (1987), who modelled S waveforms recorded at the NARS network by trial and error. She concluded that variations of the S wave velocity in the upper 400 km of Europe's mantle are at least 4% and that

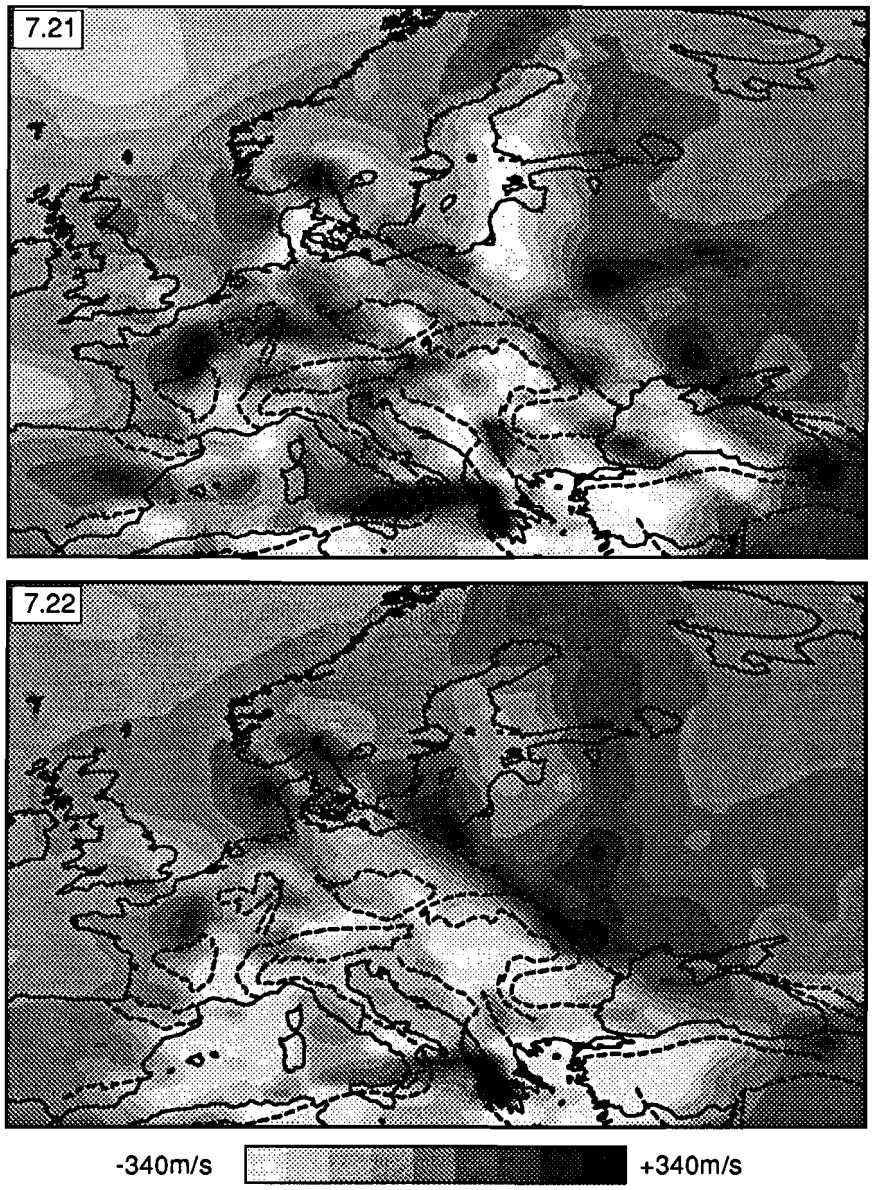

Figure 7.21. S velocity anomalies below the Moho discontinuity after linear corrections for crustal thickness. Reference velocity is 4.32 km/s.

Figure 7.22. S velocity anomalies at 80 km depth after linear corrections for crustal thickness. Reference velocity is 4.5 km/s.

even between 300 and 400 km depth variations of a few percent occur.

An important result is the image of the deeper structure below the TTZ. Above 200 km depth there is a sharp boundary between high velocities of the Russian Platform and Baltic Shield and lower velocities of Europe. We cannot constrain the depth to which the velocity contrast exists below the central part of the TTZ. Clearly we have to wait until more data are available for this region to confirm this. The results strongly indicate that around the 400 km discontinuity, low velocities appear below the western boundary of the Russian Platform, but we can not constrain whether there is a continuous zone, or discrete anomalies. In this respect it is interesting to mention the results of Rial et al. (1984) who studied the lateral variation of the S wave velocity across the Alpine front in Europe by examining long-period S and SS waveforms. They found that the S velocity structure of the western Russian Platform compares well with model SNA (Grand and Helmberger, 1984) for the shield of North America. This model has a 200 km thick high velocity lid, beneath which the velocity decreases. They also concluded that the boundary between the Russian Platform and the Alpine regions is sharp. They cannot constrain the depth to which the velocity contrast extends but found indications that the lateral differences disappear below 250 km depth.

There are many similarities between the model obtained from the waveform inversion and model EURS89B. However, there are also differences, even in regions where the sensitivity tests indicate a reasonable to good resolution. A striking difference is the absence of a velocity contrast below the TTZ at 80 and 140 km depth. We suspect that this is caused by large errors in the S delays which contaminate the solution. We also observed differences in the depth extent of particular velocity anomalies. These difference can be caused by a lack of depth resolution in both models: modes cannot resolve the exact depth of the anomaly, and the linearization of the relationship between delay time data and anomalies might cause an error in the depth of the anomaly.

7.7 Conclusions

Conclusions with respect to the method:

(1) The method works: by inversion of the linear constraints we obtained a 3-D model with realistic velocity variations that generally matches the observed waveforms well, even for frequencies as high as 60 mHz.
(2) In the region with the highest density of wave paths, the high velocity slab in the Hellenic subduction zone is detected. This indicates that the PWI has the potential to yield high resolution images, provided that enough data are available.
(3) In stable intraplate regions large velocity perturbations are resolved.
(4) It should be investigated if the effect of varying crustal thickness on the retrieved velocity perturbations should be incorporated in the non-linear inversion procedure.

Conclusions with respect to the 3-D model of shear wave velocity:

(1) A sharp boundary between high velocities which characterize the Precambrian parts of

Europe and lower velocities of the younger parts of Europe exists below the TTZ to a depth of at least 140 km.

(2) Below 200 km the structure below the central TTZ is not well resolved. Near the 400 km discontinuity low velocities appear below the western boundary of the Russian Platform, just east of the TTZ. Further investigation is necessary to constrain the model in this region.

(3) Below the northwestern part of the TTZ the sharp boundary between high velocities below the Baltic Shield and lower velocities below Denmark/Germany/The Netherlands extends to 400 km depth.

Conclusions with respect to the comparison between the model obtained from waveform inversion and the model obtained from inversion of ISC S delays (chapter 3):

(1) The models agree in many respects, but there are also large differences, even in regions where the sensitivity tests indicate that the resolution is reasonable to good.

(2) Some discrepancies can be explained by lack of vertical resolution in the models, or by the fact that the inversion of the ISC delays is linearized with respect to a 1-D reference model, which can result in mapping of anomalies at wrong depths. Other differences, like the absence of a velocity contrast in the result of the ISC S delays, are probably caused by contamination of the latter result by large data errors.

7.8 Appendix 1

In this appendix we present the result of the simultaneous inversion of the phase velocity data, which were inverted in chapter 4, and the linear constraints from the waveform data. In this inversion we weighted the phase velocity data with a standard deviation of 0.05 km/s, which we estimated to be a reasonable value in chapter 4. The combined inversion yielded a value of χ^2/n equal to 1.7, which is somewhat higher than the value of 1.3 that was obtained in the inversion of the waveform data only. We know, from our experiments with various damping parameters, that such a difference leads to an increase in the number of unacceptable final fits. Assumed that the phase velocity measurements and the linear constraints obtained from the waveform inversion are not inconsistent, we can obtain a better fit to the waveform data by relaxing the damping and allowing a higher level of heterogeneity. However, since we cannot determine what an acceptable misfit for the phase velocity data is because we do not know the magnitude of the errors in those data, we refrain from experimenting with damping parameters until χ^2 is equal to 1.3 and accept the somewhat higher value for the combined inversion.

The horizontal cross sections through the resulting model are presented in figures 7.23-7.27. We show only the cross sections at 14.5-200 km depth because they differ from the result of the inversion of the waveform data only. Comparing them with the cross sections displayed in figures 7.11a-7.15a, we observe the following differences:

- Below Tuscany, the low velocity anomaly, which was reported by Panza et al. (1982) and Snieder (1988), is present at 80 km.
- The outlines of the velocity anomalies in the western Mediterranean at 80 km depth are in better agreement with Snieder's model (1988).
- At 140 km depth a strong low velocity anomaly extends below the Rhine graben, Rhone Valley and the southeastern part of Massif Central.

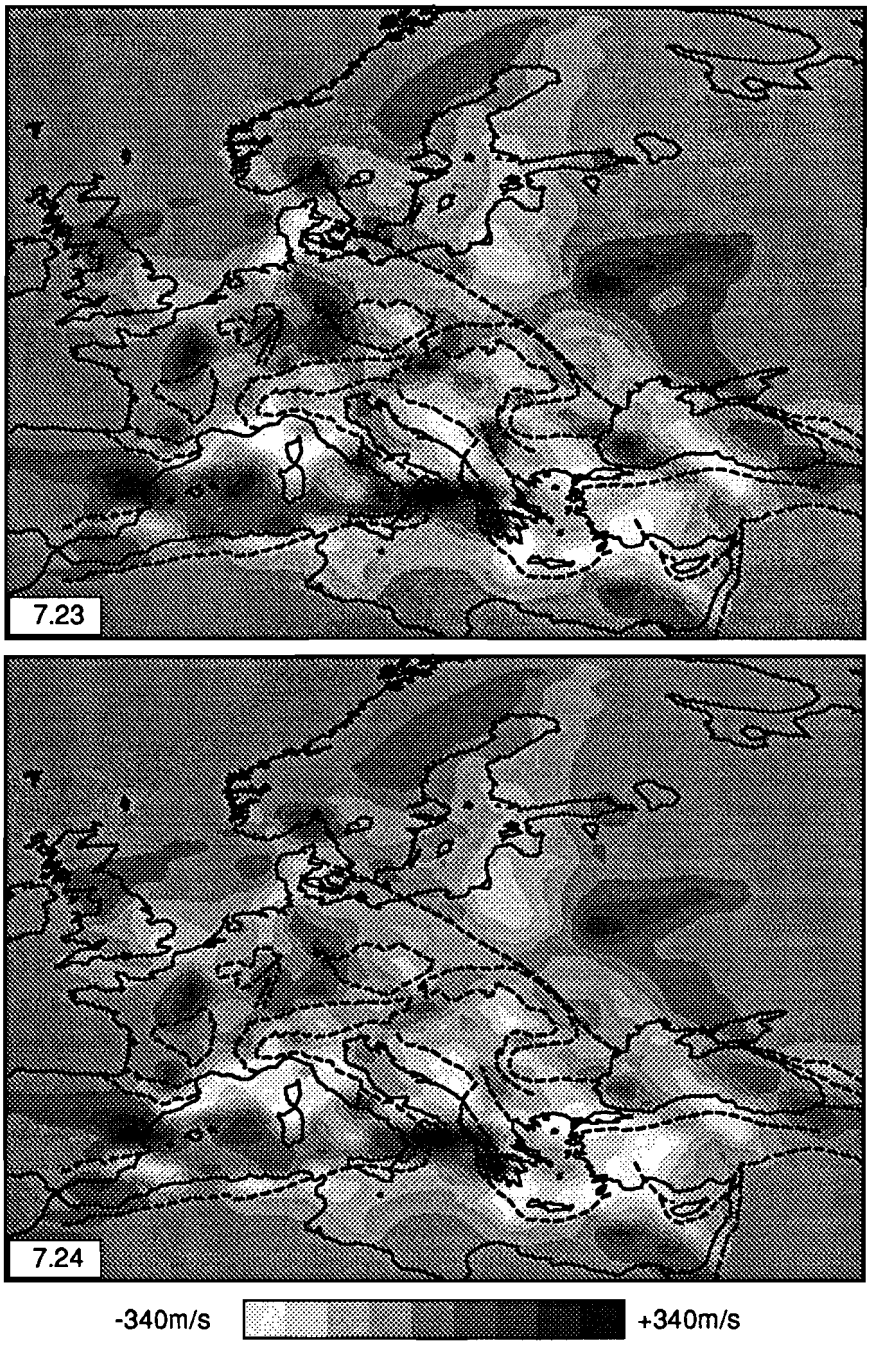

Figure 7.23. S velocity anomalies at 14.5 km depth obtained with the combined inversion of waveform and phase velocity data. Reference velocity is 3.49 km/s.
Figure 7.24. S velocity anomalies at 29 km depth obtained with the combined inversion of waveform and phase velocity data. Reference velocity is 4.32 km/s.

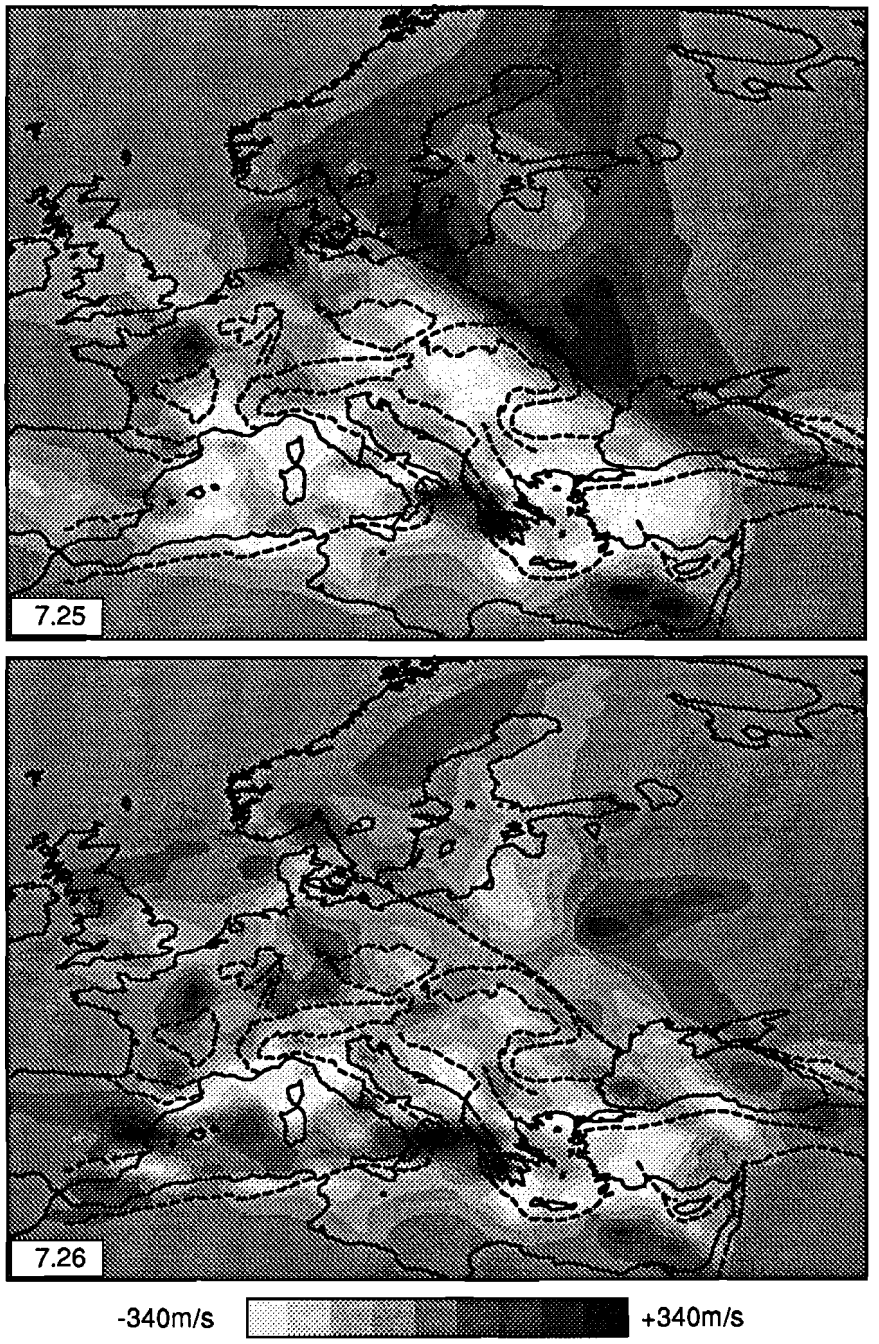

Figure 7.25. S velocity anomalies at 80 km depth obtained with the combined inversion of waveform and phase velocity data. Reference velocity is 4.5 km/s.
Figure 7.26. S velocity anomalies at 140 km depth obtained with the combined inversion of waveform and phase velocity data. Reference velocity is 4.5 km/s.

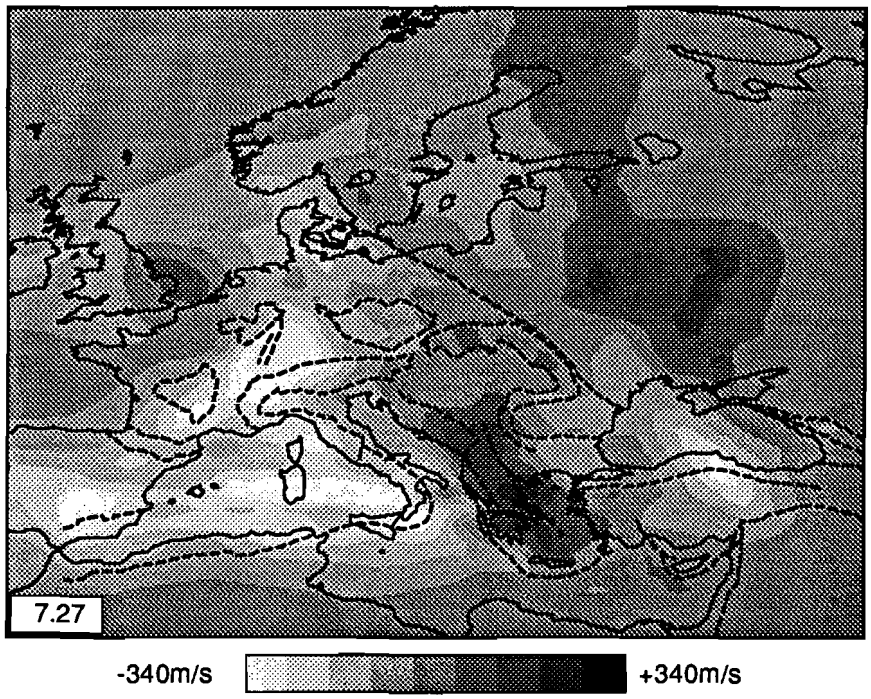

Figure 7.27. S velocity anomalies at 200 km depth obtained with the combined inversion of waveform and phase velocity data. Reference velocity is 4.5 km/s.

Figure 7.28. Recovered model from a sensitivity test with a spike below the region southwest of Massif Central: a) at 80 km depth, b) at 140 km depth. Input anomaly is contoured with a thick solid line.

7.9 Appendix 2

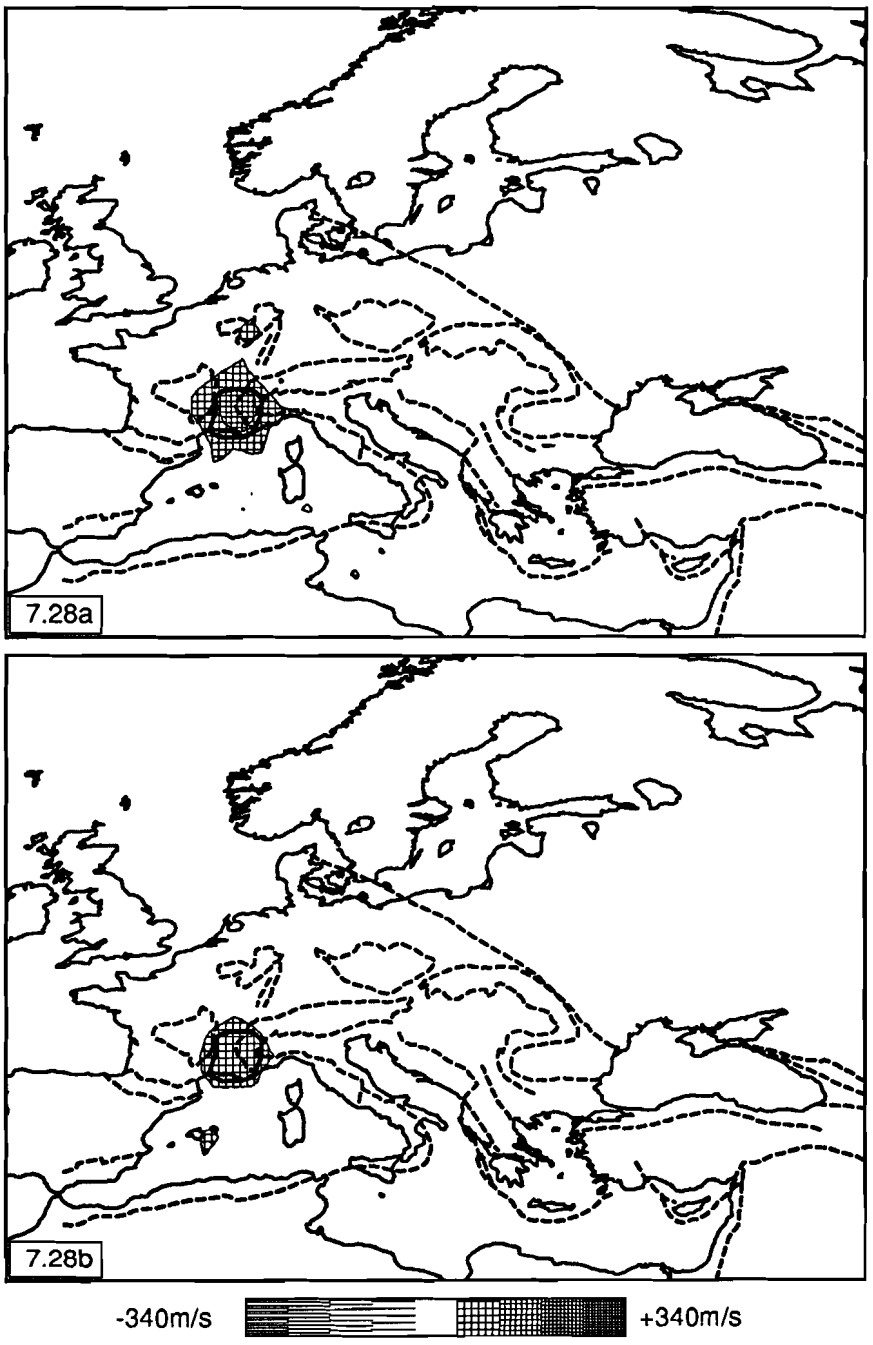

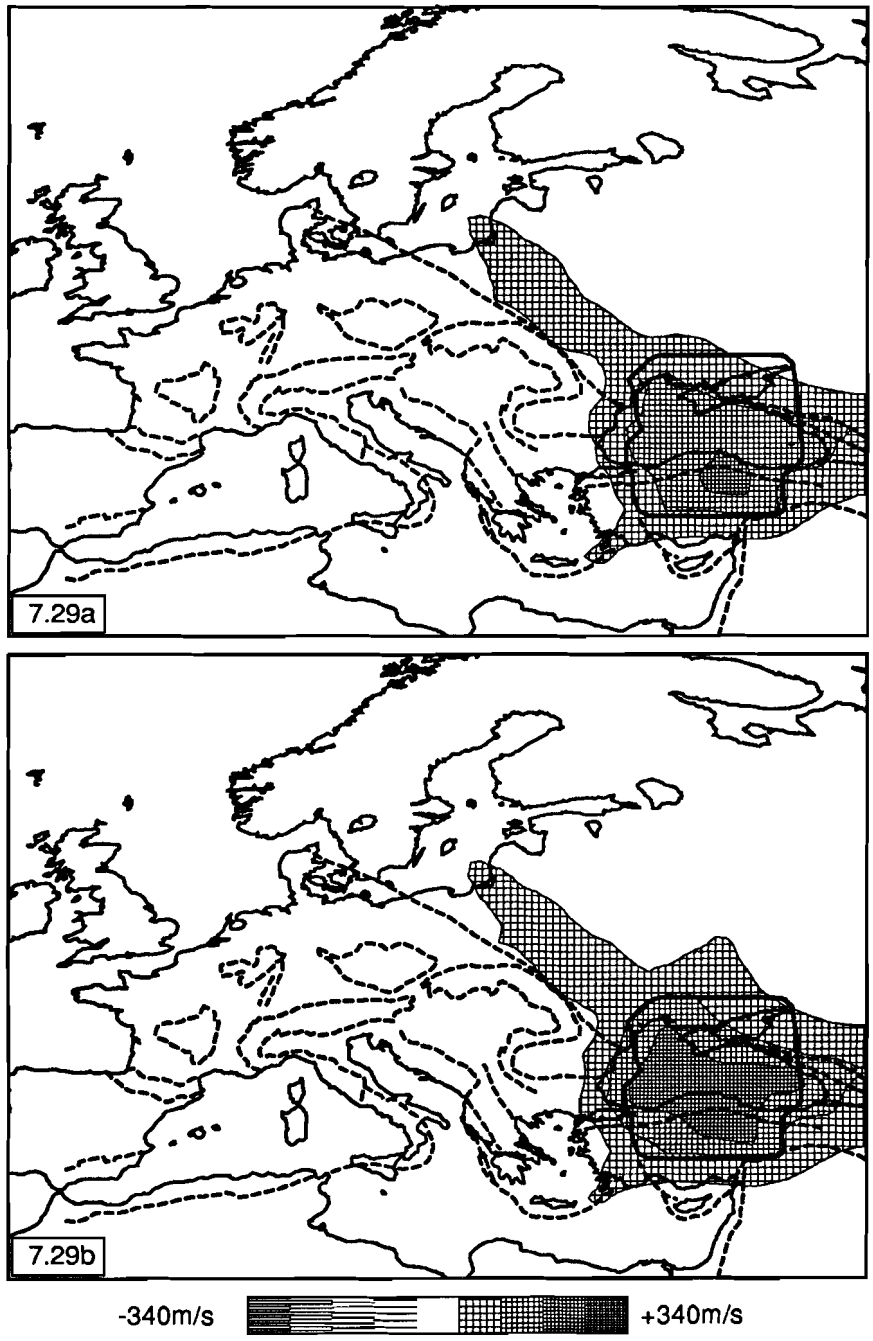

Figure 7.29. Recovered model from a sensitivity test with a spike below the Black Sea at 200-400+ km depth: a) at 200 km depth, b) at 300 km depth. Input anomaly is contoured with a thick solid line.

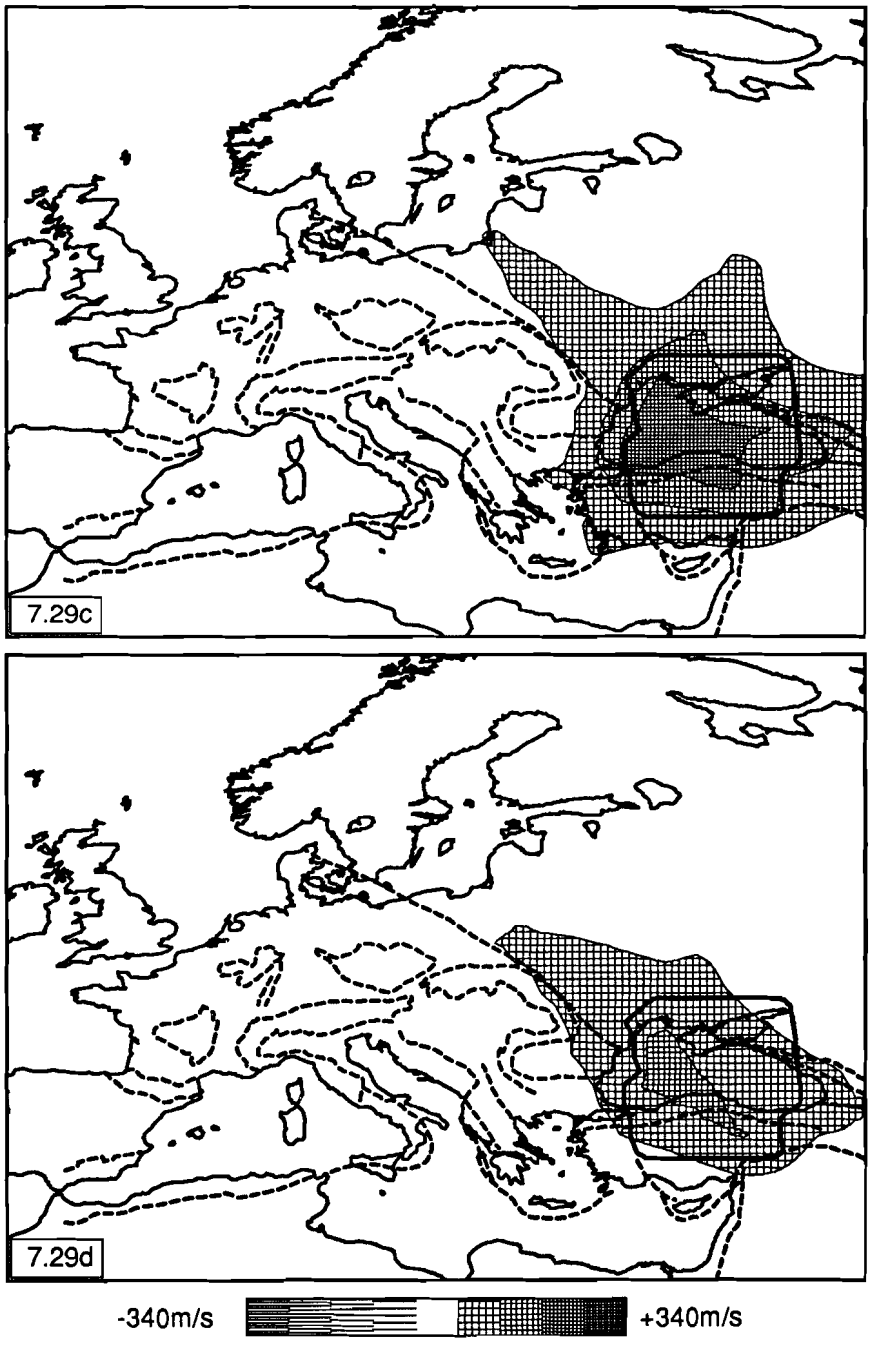

Figure 7.29. (continued) Recovered model from a sensitivity test with a spike below the Black Sea at 200-400+ km depth: c) at 400- km depth, d) at 400+ km depth. Input anomaly is contoured with a thick solid line.

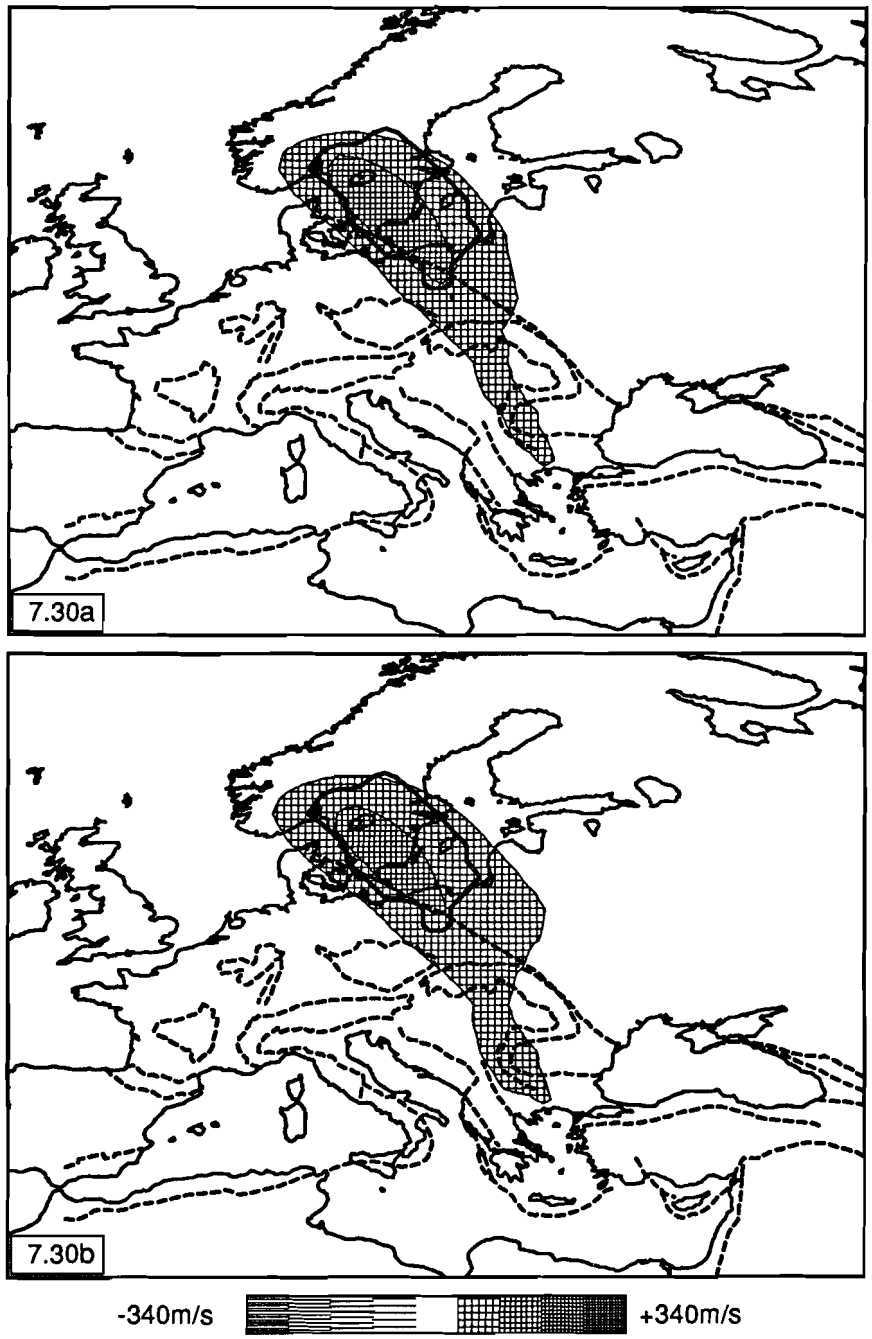

Figure 7.30. Recovered model from a sensitivity test with a spike below southwest Sweden at 300-400- km depth. a) at 300 km depth, b) at 400- km depth. Input anomaly is contoured with a thick solid line.

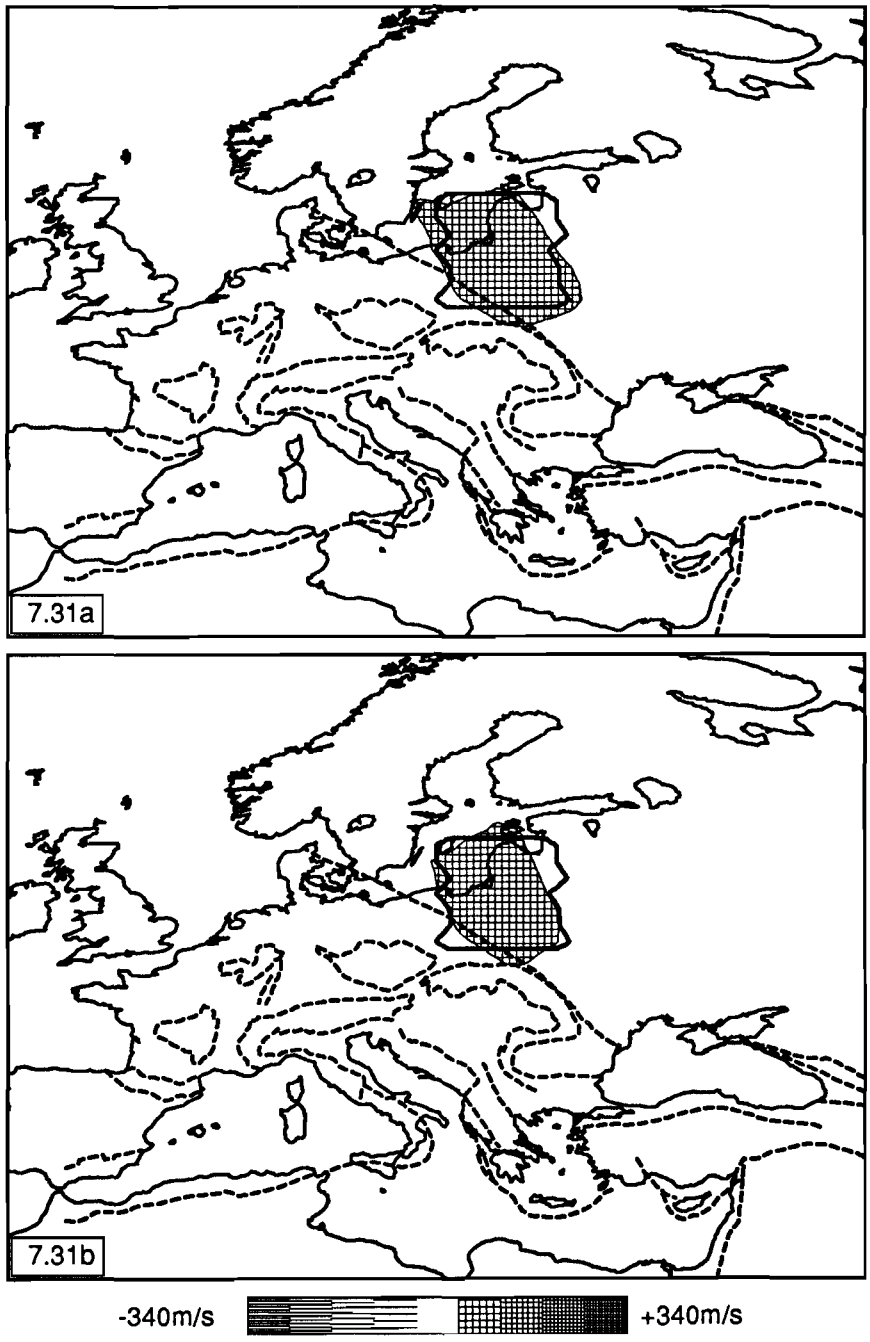

Figure 7.31. Recovered model from a sensitivity test with a spike below Poland and the Baltic Republics at 400- and 400+ km depth. a) at 400- km depth, b) at 400+ km depth. Input anomaly is contoured with a thick solid line.

Chapter 8

Discussion and comparison with results of other geophysical investigations

8.1 Introduction

The main objective of this thesis was to obtain a three-dimensional (3-D) model of the S wave velocity in the upper mantle below Europe. In chapter 7 we presented the complete solution of the Partitioned Waveform Inversion (PWI; Nolet, 1990) and the spatial resolution by means of horizontal cross sections through the 3-D S wave velocity model. In this final chapter we compare the model with results of other geophysical studies, and make a tentative interpretation of some results. However, this has been beyond the scope of the present research, and the relationships discussed will have to be investigated in more detail to obtain final conclusions.

We discuss in more detail the results of the PWI in two selected regions. We focus on the Tornquist-Teisseyre Zone (TTZ) because the PWI has provided new information on Earth structure in this stable intraplate region. Furthermore, we look in more detail to the structure in southeastern Europe because this is the best resolved part of the model, and illustrates the resolution that can be obtained with the PWI.

Despite its obvious importance for Palaeozoic tectonics, little is known about the tectonic history and the mantle structure below the TTZ. Deep Seismic Sounding (DSS) projects (e.g., Guterch et al., 1983) indicated that the TTZ separates the pre-Cambrian crust of the Baltic Shield/Russian Platform from the younger crust of western Europe. In chapter 7 we concluded that lateral variations in seismic velocity associated with the TTZ are

detectable by the PWI to a depth of about 400 km. Apart from the implications for the tectonic history of the TTZ, which are beyond the scope of our investigation, this indicates that the contrast between the Pre-Cambrian regions and younger regions in Europe is not restricted to crustal depth levels. Here we want to improve insight in the 3-D structure.

We discuss in more detail the results for southeastern Europe because the attained resolution allows us to make a direct comparison with the results of other studies of seismic velocity, notably the P wave velocity models obtained by delay time tomography. This is encouraging for future Vp/Vs ratio studies.

Where appropriate, we qualitatively compare our solution with results of other geophysical studies: P wave velocity models and heat flow measurements. As a reference for our comparison with heat flow we present in figure 8.1 a schematic map of the heat flow in Europe. The solid lines depict the lines of cross section of the mantle sections discussed below.

A direct interpretation of the velocities in terms of composition of the upper mantle is complicated by a number of factors: there is an abundance of laboratory measurements of seismic velocities in rock forming minerals, and some of their derivatives at room temperature and pressure, but they often show a large variability with minor changes in composition (Sumino and Anderson, 1984); there is a shortage of such measurements and particularly of the derivatives with respect to pressure and temperature at ambient upper mantle conditions; there is considerable uncertainty in the values of local S velocities that result from our study, since the images produced represent broad averages; and the local P velocities are not accurately known. We shall nevertheless attempt to make some order-of-magnitude calculations and draw tentative conclusions.

8.2 The Tornquist-Teisseyre Zone (TTZ)

8.2.1 Tectonic framework of the TTZ

It has generally been acknowledged that the TTZ separates the pre-Cambrian crust of the Russian Platform/Baltic Shield from the younger crust of western Europe. The crustal structure of the TTZ has been investigated in many DSS projects. These studies reveal that in Poland the TTZ is up to 90 km wide and separates the thick crust of the Russian Platform from the thinner crust towards the southwest (Guterch et al., 1983).

Figure 8.1. Heat flow map of Europe, constructed by Suhadolc and Panza (1989) after the heat flow map by Cermak and Hurtig (1979). The curved lines represent the contour lines for 50 mW/m^2. The straight lines depict the positions of the vertical sections discussed in this chapter.

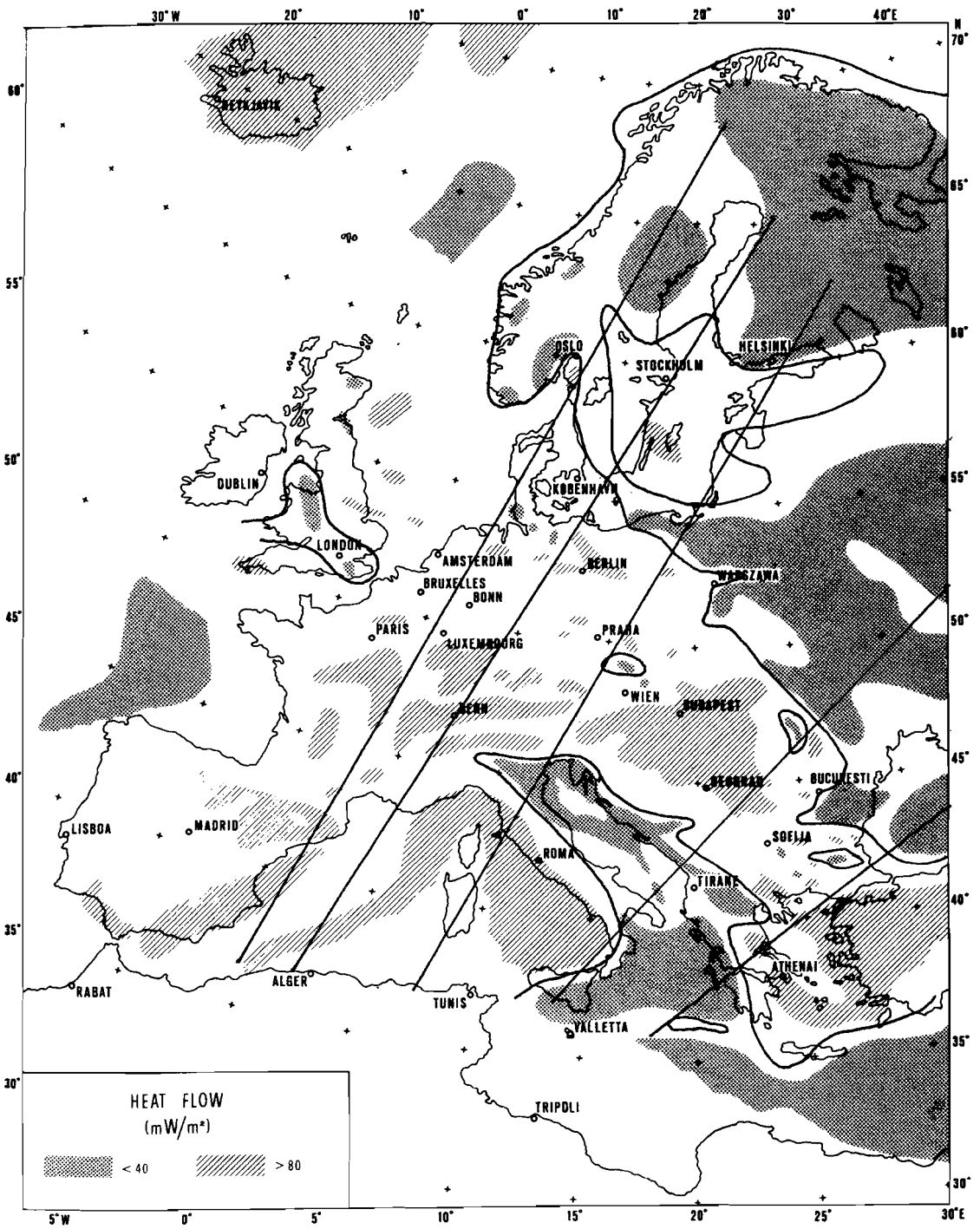
30° W
20°
10°
0°
10°
20°
30°
40° E
N
70°
65°
60°
55°
50°
45°
40°
35°
30°
REYKJAVIK
OSLO
STOCKHOLM
HELSINKI
DUBLIN
KOBENHAVN
LONDON
AMSTERDAM
BERLIN
WARSZAWA
BRUXELLES
BONN
PARIS
LUXEMBOURG
PRAHA
WIEN
BUDAPEST
BERN
BEOGRAD
BUCURESTI
LISBOA
MADRID
SOFIJA
ROMA
TIRANE
ATHENAI
RABAT
ALGER
TUNIS
VALLETTA
TRIPOLI
HEAT FLOW
(mW/m²)
< 40
> 80
5° W
0°
5°
10°
15°
20°
25°
30° E

Below the zone itself the Moho depth is larger than in adjacent regions. In southern Scandinavia, drilling (Noe-Nygaard, 1963; Sorgenfrei and Buch, 1964) and DSS studies (EUGENO-S working group, 1988) indicated the presence of pre-Cambrian basement south of the TTZ. The southwestern boundary of the Baltic Shield is not yet located with certainty but it coincides perhaps with the Trans European Fault shown in figure 8.2 (Europrobe working group, 1991).

Investigators concur that the TTZ has influenced the geological development of Europe since Hercynian times (EUGENO-S working group, 1988). However, the tectonic history of the line itself is subject to debate. Palaeomagnetic studies have indicated that in late pre-Cambrian and early Palaeozoic times (~570Ma) the Baltic Shield and Russian platform formed a continent, Baltica, that was separated by an ocean from the terrains that now compose western Europe (e.g., Torsvik et al., 1990). It is uncertain when the southwestern boundary of this platform became first tectonically active. During the successive orogenic cycles, Caledonian (Silurian), Hercynian (Carboniferous) and Alpine (early Tertiary), more and more terrains were accreted to the southwestern boundary of Baltica. Figure 8.2 shows the current tectonic setting of the TTZ.

8.2.2 Lateral heterogeneity below the TTZ

In figures 8.3-8.8 we present cross sections which are approximately perpendicular to the TTZ (see also figure 8.1). Above each section we show the location of the section in a map. Sensitivity tests have shown that not all features visible in the sections are reliably imaged. Wherever appropriate we indicate which features are poorly resolved. At some locations the model has a sharp velocity contrast at 400 km depth. The waveform data that we used can not resolve such sharp velocity contrasts. The contrast in the model is an artifact caused by the combination of smoothness constraints imposed on the model and lack of vertical resolution, and should therefore not be considered a reliable feature. The sections show that Earth's structure below the TTZ changes from the northwestern to the southeastern part. Sections 1 and 2 (figures 8.4 and 8.5) reveal that the northwestern part coincides with a lateral transition from high velocities below the Baltic Shield to relatively low velocities below western and central Europe down to a depth of at least 400 km. The high velocity layer that extends from the Baltic Shield southward below Denmark at 80 km depth coincides with the high velocity/high density feature observed by Dost (1990) beneath the NARS array, but this feature is not very reliable in our model. The northern boundary of the high velocity anomaly below southern Sweden is not well constrained. Sections 4 and 5 (figures 8.6 and 8.7) show that below the central part of the TTZ, the boundary between high velocities below the Russian Platform and lower velocities below central Europe exists to a depth at least of 140 km. However, at a larger depth, near the 400 km discontinuity, lower velocities appear below the southwestern boundary of the Russian Platform. There is an indication that high velocities extend to larger depths further to the east, but this result has to be interpreted with care since the location of the transition is not well resolved. The transition from high velocities extending to a depth of the 400 km to

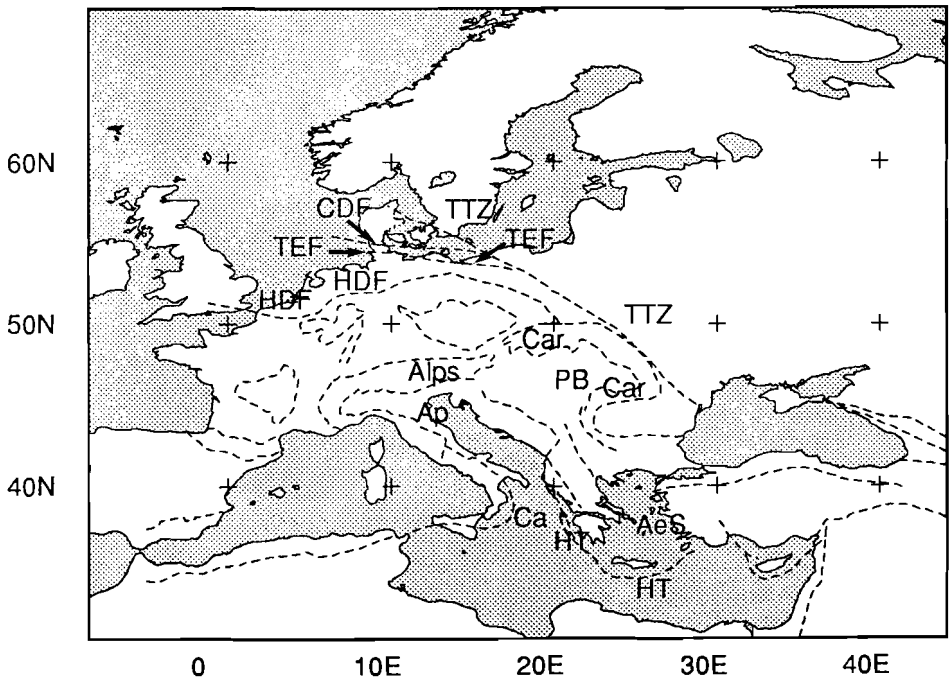

Figure 8.2. Tectonic map of Europe. *CDF* = Caledonian Deformation Front of the north German-Polish Caledonides, *TTZ* = Tornquist-Teisseyre Zone, *TEF* = Trans European Fault. *AeS* = Aegean Sea, *Alps* = Alps, *Ap* = Apennines, *Ca* = Calabrian Arc, *Car* = Carpathians, *HT* = Hellenic Trench, *PB* = Pannonian Basin.

lower velocities near the 400 km discontinuity, just north of the TTZ, is located beneath the Baltic Sea or northern Poland (figure 8.5). Lateral heterogeneity is still present in the transition zone though the contrast in seismic velocity is small.

To assess the percentage of the velocity contrast across the TTZ that is resolved, we performed a sensitivity test with an input model consisting of a constant positive anomaly for the region east of the TTZ and a constant negative anomaly west of the TTZ at depths of 80 and 140 km. This test revealed that at 80 km depth almost 100% of the velocity contrast is resolved whereas at 140 km depth between 65% and 90% of the contrast is resolved. However, figures 7.13a and 7.14a show that the velocity pattern along the TTZ is more complicated than two blocks with constant velocity. As we showed in chapter 7, the percentage of resolved anomaly is influenced by the shape of the anomaly due to the effect of the gradient damping. Therefore, this test only gives an approximation of the resolved velocity contrast. In results of this test we observe the following. At 80 km depth the velocity contrast across the Pannonian Basin and Russian Platform is about 12%. At 140 km the model indicates a contrast of 6.5%, which could mean, considering the above described sensitivity test, a value of about 9% for the 'true' contrast.

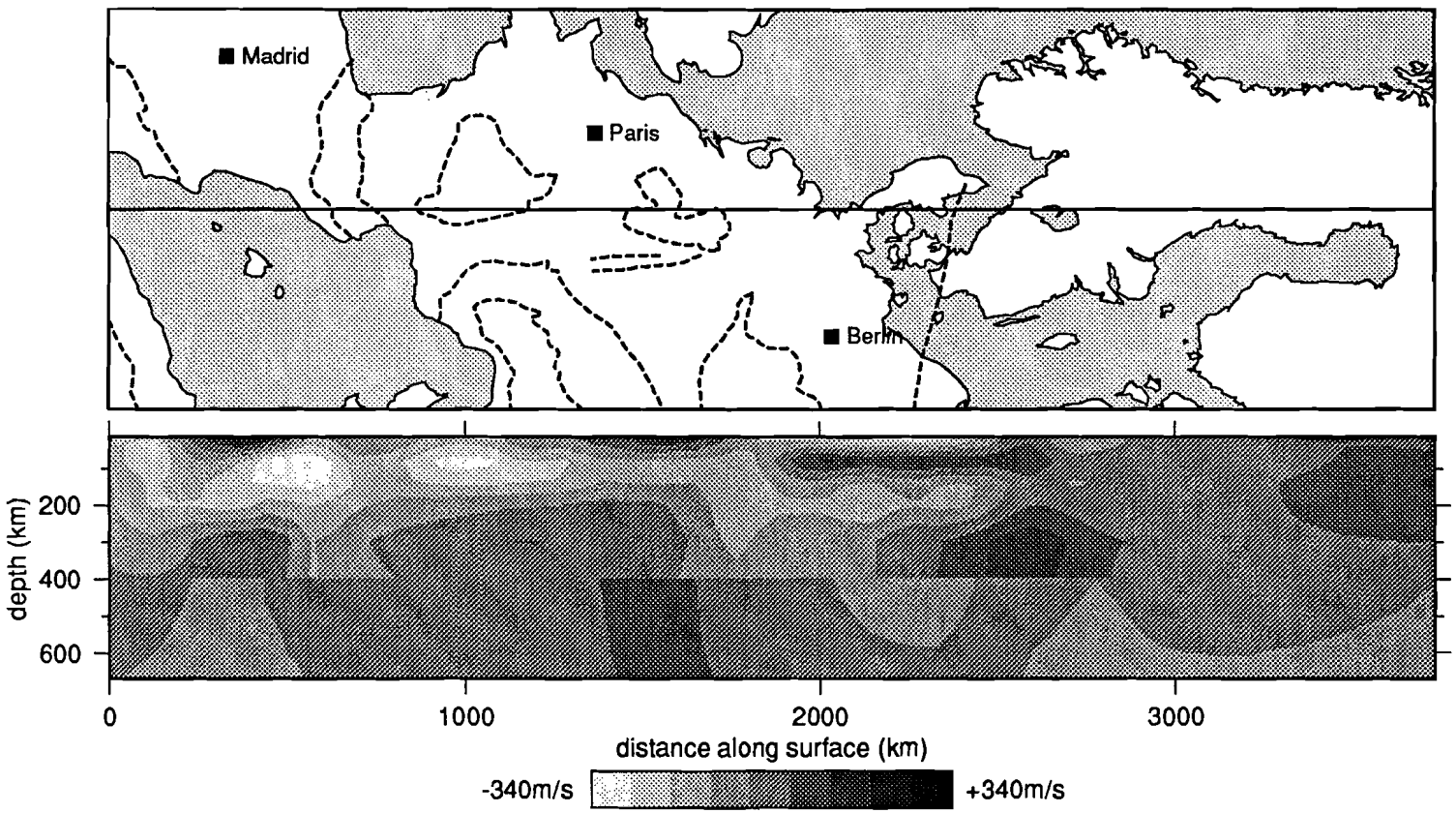

Figure8.3 Vertical section 1, from (36.5N,0E) to (67.2N,23.56E). Velocity perturbations with respect to the reference model are contoured from -340 m/s to +340 m/s.

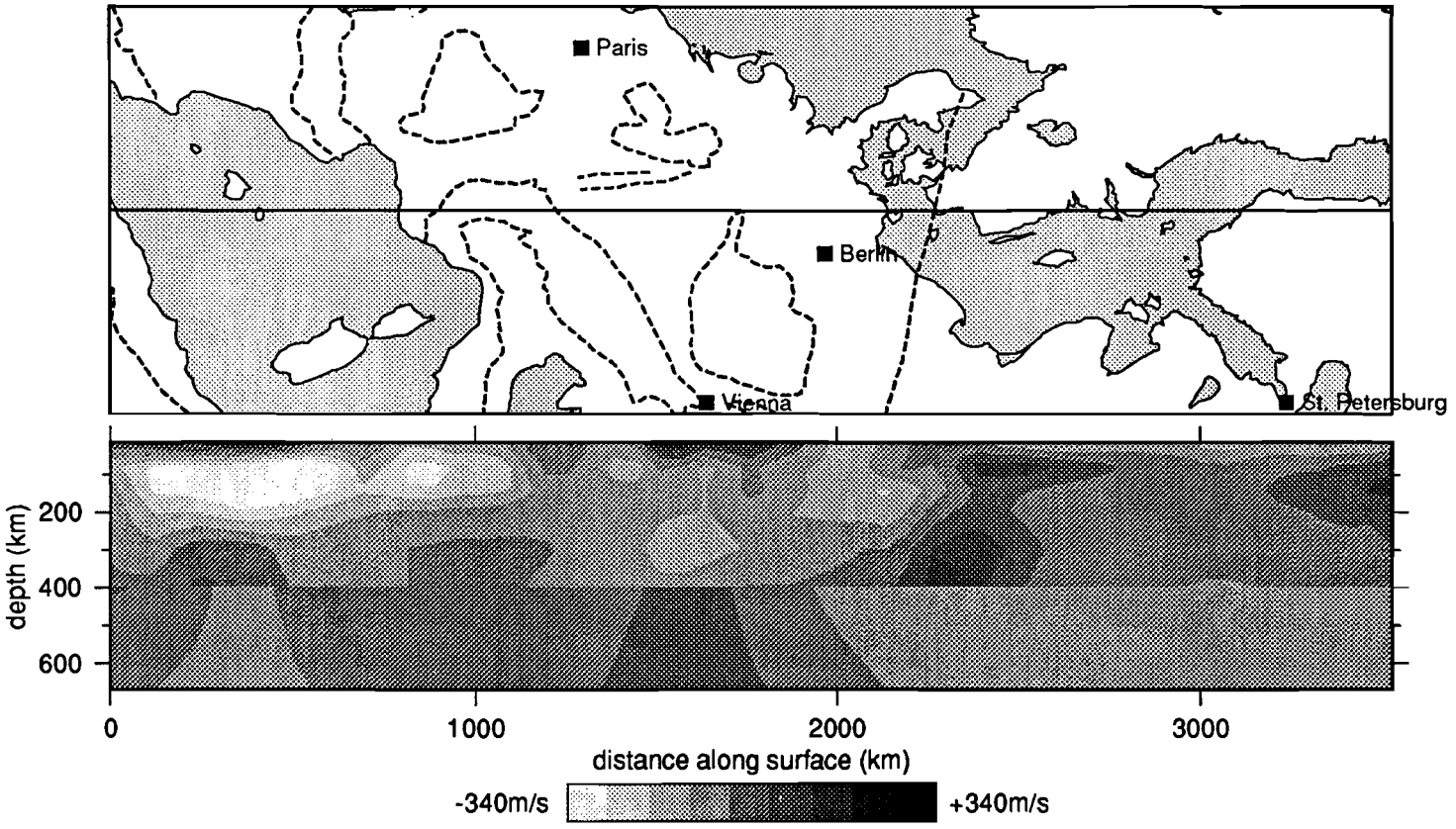

Figure 8.4 Vertical section 2, from (36.5N,2.5E) to (65N,26E). Velocity perturbations with respect to the reference model are contoured from -340 m/s to +340 m/s.

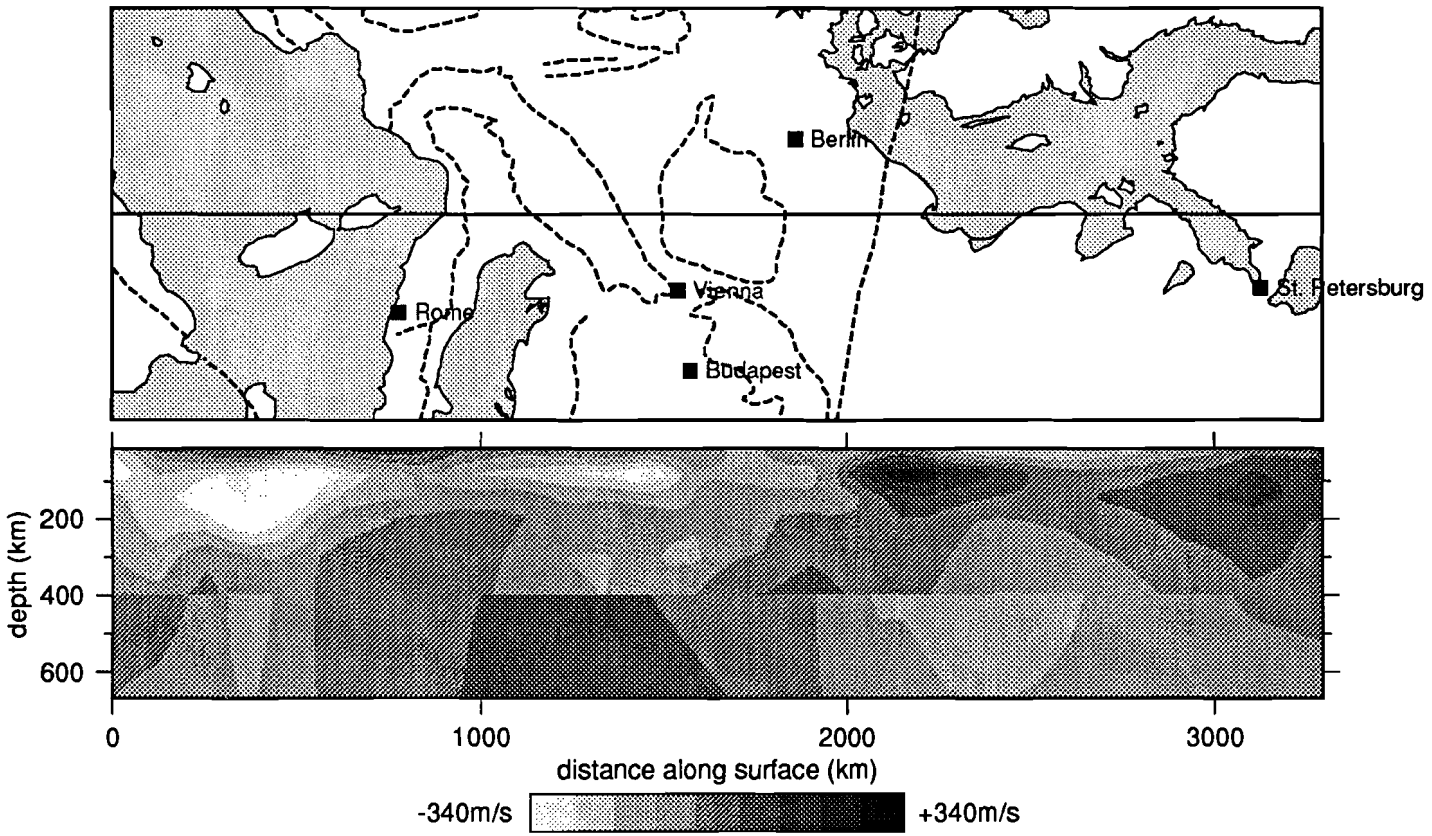

Figure 8.5 Vertical section 3, from (36.5N,6E) to (62.3N,29.5E). Velocity perturbations with respect to the reference model are contoured from -340 m/s to +340 m/s.

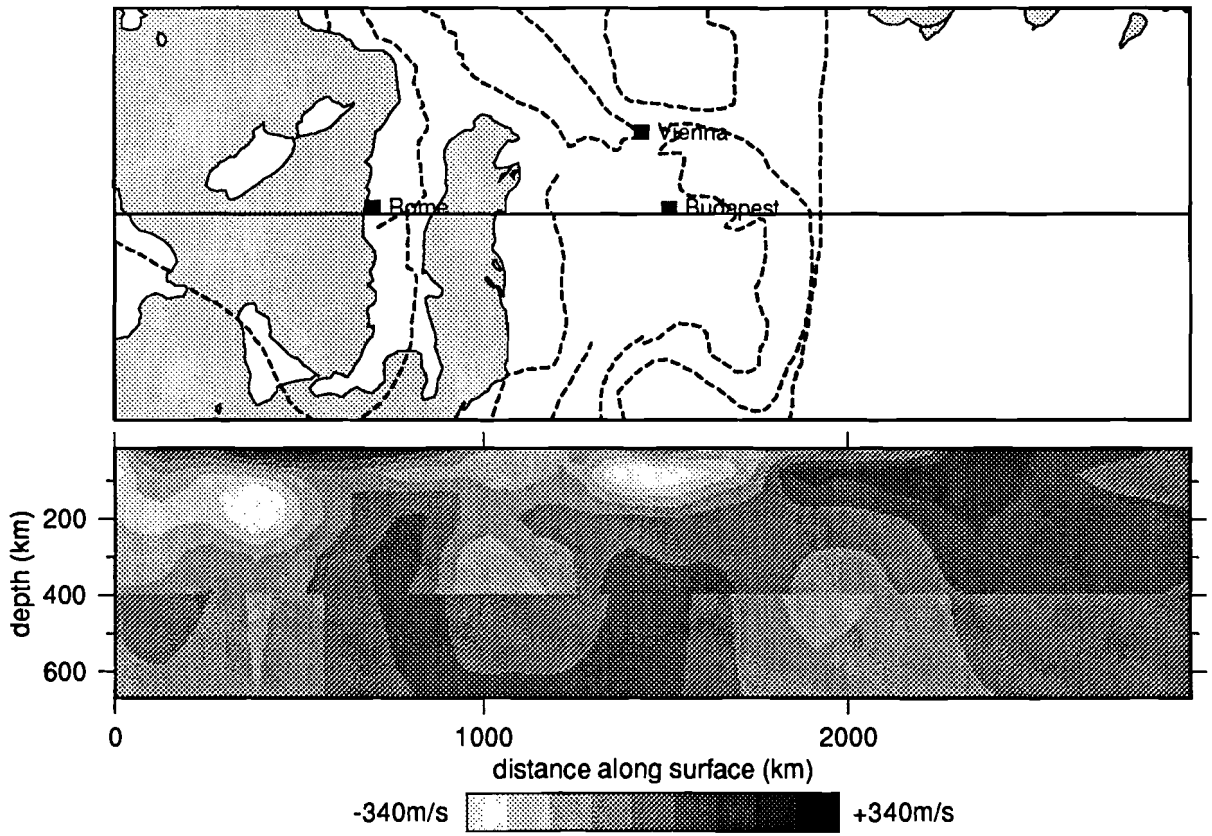

Figure 8.6 Vertical section 4, from (36.7N,7.9E) to (56N,34.6E). Velocity perturbations with respect to the reference model are contoured from -340 m/s to +340 m/s.

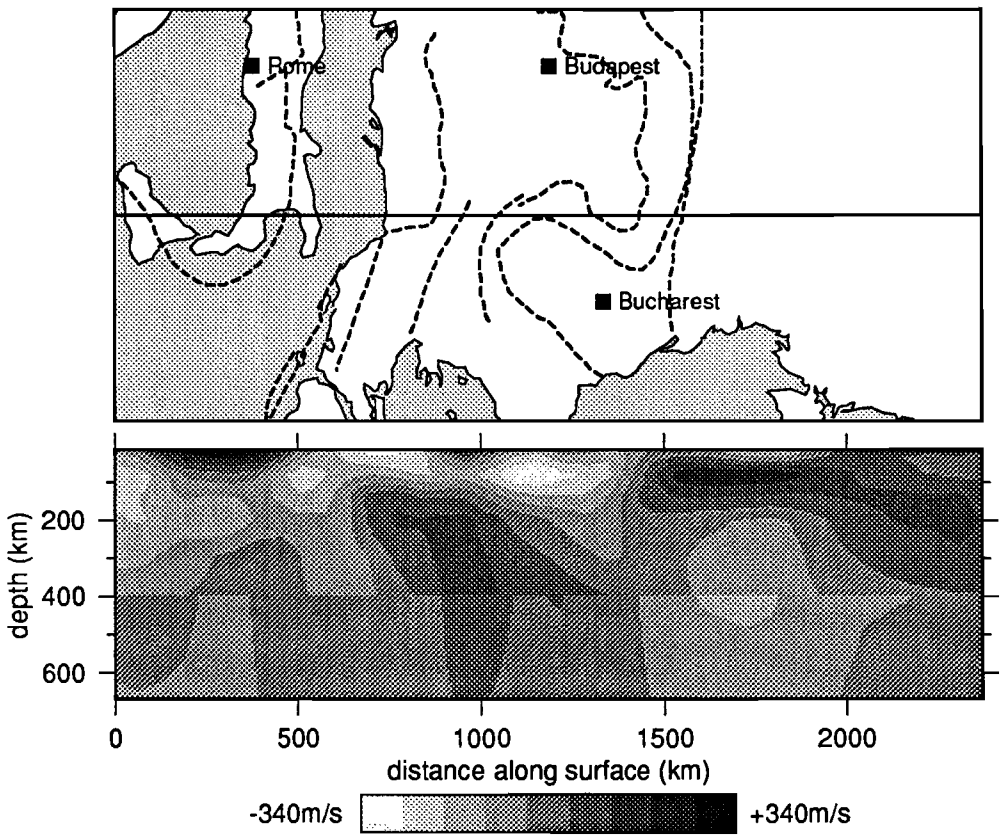

Figure 8.7 Vertical section 5, from (37N,13.5E) to (52N,35E). Velocity perturbations with respect to the reference model are contoured from -340 m/s to +340 m/s.

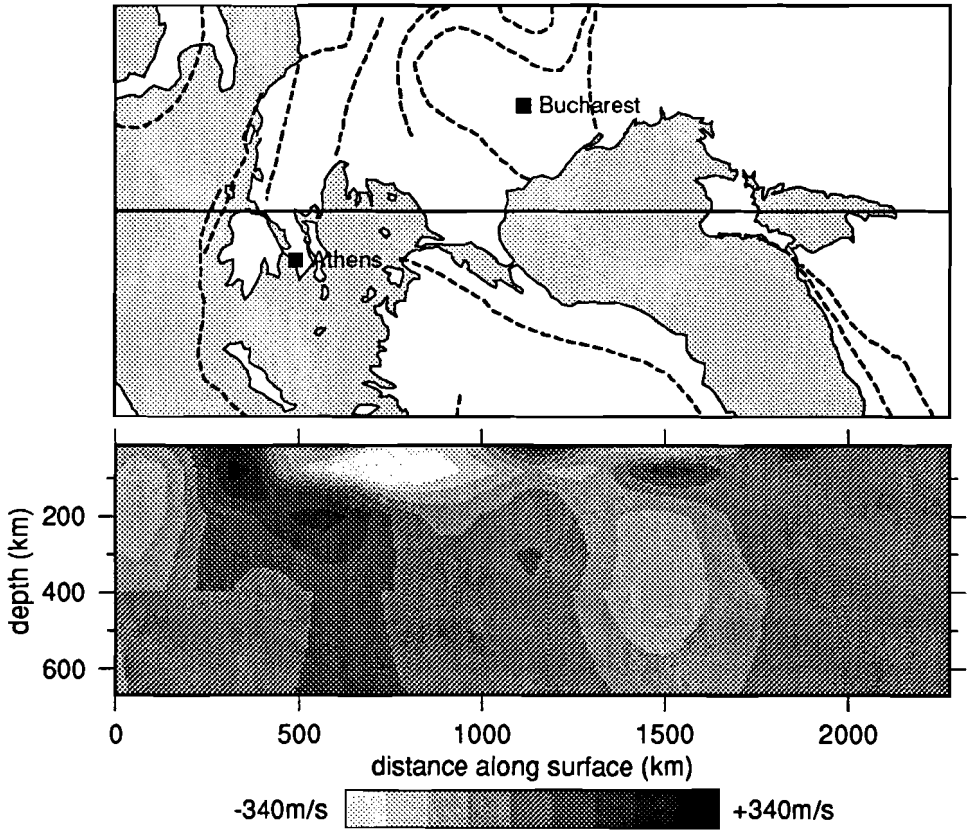

Figure 8.8 Vertical section 6, from (36N,18.4E) to (47.9N,41E). Velocity perturbations with respect to the reference model are contoured from -340 m/s to +340 m/s.

In Poland the velocity contrast across the TTZ is approximately 8.5% at 80 km and 3.5% at 140 km possibly indicating a true contrast of nearly 4.5% at this depth. The velocity contrast between southern Sweden and Denmark/northern Germany is about 5% at 80 km, 3.5% at 140 km which might be consistent with an 'undamped' contrast of about 4.5%. These values show that the highest velocity contrast across the TTZ in the upper 140 km of the mantle is observed between the Pannonian Basin and the Russian Platform, the lowest contrast is observed between southern Sweden and Denmark/northern Germany.

8.2.3 Comparison with P wave velocity and heat flow

The result of the linearized inversion of ISC P-wave travel-time residuals of Spakman et al. (in preparation), hereafter referred to as model EUR89B, shows a weak contrast (<1.5%) between positive anomalies below the Baltic Shield and negative velocity anomalies below Denmark to a depth of 460 km. Furthermore, model EUR89B indicates positive P wave anomalies (<1.5%) below the Russian Platform between 70 and 170 km depth. Below 460 km, low velocities appear below the Russian Platform. The trend in P wave velocity below the TTZ as indicated by EUR89B seems to be in agreement with our result, but we do not want to draw any conclusions from this because the resolution below the Baltic Shield and the Russian Platform in EUR89B is poor.

The heat flow map (figure 8.1) shows that the TTZ coincides with a transition from generally low heat flow values on the Russian Platform and Baltic Shield to higher heat flow in western and central Europe. This pattern correlates with the transition from low S wave velocities below western and central Europe and high velocities below the Russian Platform/Baltic Shield at 80 and 140 km depth (see figures 7.13a and 7.14a for a map view of the S wave velocity). The largest gradient of average S wave velocity above 140 km depth across the TTZ is observed below the Pannonian Basin and Russian Platform (section 4, figure 8.6). This region also shows the largest contrast in heat flow across the TTZ. The heat flow values for the southern part of the Baltic Sea and Sweden are higher than for the rest of the Baltic Shield, and the contrast with heat flow values for Denmark and northern Germany and Poland is smaller. We also observe a smaller contrast in the average upper mantle velocity above 140 km depth across the northwestern part of the TTZ. The comparison shows that the main trends in the heat flow pattern across the TTZ correlate with the average value of the S wave velocity in the upper mantle above 140 km depth in the sense that high heat flow is measured above regions with low average velocities whereas regions with high average velocities are characterized by low heat flow values.

8.3 Southeastern Europe

8.3.1 Tectonic framework

The southeastern part of Europe was formed during much more recent plate movements than the regions of northern Europe described above. The Alpine evolution resulted in the closure of the Neo-Tethys and the collision of the African, Eurasian, and Arabian plate. The Alps and Carpathians were formed as a result of this collision and mark the northern

deformation front of the Alpine orogenic cycle in Europe. Subduction took place below many fold belts in this region, for instance below the northern and eastern Carpathians, the central and eastern Alps, and southern Carpathians (e.g., Ziegler, 1988). Crustal shortening still persists in the western Alps, the Apennine-Calabrian and Hellenic arc (Ziegler, 1988). The Pannonian Basin and northern Aegean sea are back-arc basins which were formed during Neogene times, and are characterized by Neogene volcanism (Ziegler, 1988). For a detailed tectonic history of southeastern Europe we refer to Dercourt et al. (1986) and Ziegler (1988). The major tectonic elements in this region are indicated in figure 8.2.

8.3.2 Lateral heterogeneity in S wave velocity below southeastern Europe

Sections 4-6 (figure 8.6-8.8) illustrate S-wave velocity variations in southeastern Europe. Section 4 (figure 8.6) shows that below central Italy a high velocity anomaly extends from 140 km to larger depths. The Pannonian Basin has low velocities above 140 km depth and high velocities below 300 km depth. The right hand side of section 4 (figure 8.5) shows the sharp transition to the higher velocities of the Russian Platform above 140 km depth and low velocities near the 400 km discontinuity below the western boundary of the Russian Platform. The dipping high velocity anomaly in the central part of section 5 (figure 8.7) is the image of the subducting slab in the Hellenic collision zone. Section 6 (figure 8.8) shows a sharper image of this subduction zone. This is the part of the model with the highest resolution because the density of wave paths in this region is the highest. It indicates the level of resolution that can potentially be obtained with the PWI. A strong low velocity anomaly is present below the northern part of the Aegean Sea to a depth of 140 km. Below the Black Sea low velocities extend from 200 km depth to below the 400 km discontinuity.

8.3.3 Comparison with P wave velocity and heat flow

The P-wave velocity model EUR89B shows largely the same trend in velocity for the Pannonian basin: low velocities are present above 170 km depth, higher velocities appear below 330 km depth although a significant increase in velocity is observed at 530 km. The high velocity anomaly below Italy correlates well with the zone of high P wave velocities below Italy. Other, more regional, tomographic studies of the P wave velocity reveal similar features. Hovland and Husebye (1981) and Gobarenko et al. (1987) also report low P wave velocities below the Pannonian basin to 300 km depth. Calcagnile and Scarpa (1985) report a high velocity anomaly below 100 km depth beneath central and southern Italy. The image of the subducting slab correlates well with the image of the high velocity slab in model EUR89B. The low velocity anomaly below the northern Aegean Sea (section 6, figure 8.8) is also present in model EUR89B. However, the low velocity anomaly below the Black Sea, visible in section 6, is much less pronounced in model EUR89B. In general, the lateral variations in S wave velocity below southeastern Europe compare well with the variations in P wave velocity.

The heat flow map shows that the Pannonian Basin and the northern Aegean Sea are characterized by high heat flow values. They both show low velocities at 80 and 140 km depth (section 4 and 6 (figures 8.6 and 8.8), figures 7.13a and 7.14a). These features can be explained by the fact that these regions are back-arc basins with Neogene volcanic activity. Low heat flow is measured on the Russian Platform and the Black Sea, where the average upper mantle velocity above 140 km is high. Similar to our observations for the TTZ, the main features of the heat flow pattern in this region correlate with the average mantle velocity in the upper 140 km.

8.4 Possible interpretations of the velocity contrasts

In order to make a more quantitative comparison of the S wave velocity and heat flow data, we suggest the following, tentative, interpretation of the velocity contrasts. A contrast of the order of 10% in S velocity between the Russian Platform and lowest velocities in Central and Southeastern Europe is unlikely to be caused by a simple temperature effect. For olivine, with $\partial V_s/\partial T \approx -0.35 m/s/°K$ (Sumino and Anderson, 1984), such a velocity contrast would imply a temperature contrast of almost 1300°; for pyroxenes or garnet this contrast would be even larger, because they have lower temperature derivatives (e.g., Nolet et al., 1986b). Pollack and Chapman (1977) derived geotherm models from surface heat flow data assuming steady state conduction, with heat flowing into the base of the lithosphere and internal heat generation by radioactive decay. From their geotherms we infer a temperature of 1200 °C and 650 °C at 80 km depth for regions with a heat flow of 40 and 80 mW/m^2, respectively. This would imply a temperature difference of 550 °, which is much smaller than the difference required by the S wave velocity variation. Partial melting can lead to much more drastic effects on the S velocity and may be a probable cause for the low velocities beneath the Carpathians, the northern Aegean Sea/Western Turkey, and other regions in Central Europe that are characterized by high heat flow values and low S wave velocity. The higher velocities under the Russian Platform (≈3%) and the Ukrainean shield (≈5%) could imply a temperature difference of several hundred degrees, an enrichment in clino-pyroxenes and garnets (which have high V_s compared to ortho-pyroxene), or a combination of both.

Yan et al. (1989) interpreted the S velocity variations from the model of Woodhouse and Dziewonski (1984) at 150 km depth in terms of temperature variations (assuming a mantle composition of olivine) or changes in iron content of olivine. Their values for the derivatives of V_s with respect to temperature and iron content are -0.397 m/s/°C and -2110 m/s/ per fractional change in $Fe/(Fe+Mg)$ respectively; their reference velocity and temperature are 4.506km/s and 1300 °C, respectively. Using these values, the high velocity below the Russian Platform of ≈ 2.5% (interpolated at 150 km depth) requires a temperature of ≈ 1020°C, which is in agreement with a value of 1050°C at 150 km depth as inferred from the geotherm of Pollack and Chapman (1977) for a surface heat flow of 40 mW/m^2. A decrease in iron fraction of 0.05 would result in the same velocity contrast. The low velocity below the Carpathians (≈ -6%) would require a temperature of 1900°C, or

a decrease in iron content of 0.125, assuming that the linearization of the relationship is still valid for such large perturbations. We cannot compare this temperature with the geotherm of Pollack and Chapman (1977) at 150 km depth for a surface heat flow of 80 mW/m^2 because they terminated this geotherm at approximately 100 km depth, where it intersects their mantle solidus. However, the required temperature contrast at 80 km depth is much larger than what seems realistic on the basis of the geotherms, so it is likely that partial melting causes the low velocities below the Carpathians.

8.5 Concluding remarks

- The average mantle velocity in the upper 140 km correlates with the main trend of the heat flow pattern in the region of the TTZ and southeastern Europe in the sense that high heat flow is measured over regions with low velocities, low heat flow is measured over regions with high velocities.
- The observed velocity contrast across the TTZ is largest between the Pannonian Basin and the Russian Platform and may be about 12% and 9% at 80 km and 140 km depth, respectively. The lowest contrast is observed between southern Sweden and Denmark/northern Germany where the velocity contrast is approximately 5% and 4.5% at 80 and 140 km depth, respectively.
- Assuming the reference values of Yan et al. (1989) for V_s and T at 150 km depth (4.506 km/s and 1300 °, respectively) the high velocity below the Russian Platform can be interpreted in terms of a thermal anomaly of a few hundred degrees. This would be consistent with the temperature to be expected on the basis of the geotherm for a region with surface heat flow of 40 mW/m^2 at 150 km depth, which is a typical value for the Russian Platform. However, a compositional difference, or a combination of both, is also possible. Partial melting is a probable cause for the low velocities below the Carpathians and the northern Aegean Sea/Western Turkey.
- In southeastern Europe, the S-wave velocity variations of our model correlate well with the P-wave velocity model of Spakman et al. (in preparation) with respect to the sign of the anomalies, but in general the amplitudes of the S wave anomalies are larger.
- Below Greece the density of wave paths is highest and the model shows velocity variations of comparable wavelength as are resolved in the P wave velocity model. This indicates that the PWI has the potential to yield high resolution images, provided that enough data are available.

References

Adams, R. D., A. A. Hughes and D. M. McGregor, Analysis procedures at the International Seismological Centre, *Phys. Earth Planet. Inter.*, **30**, 85-93, 1982.

Aki, K., A. Christoffersson, and E.S. Husebye, Determination of three-dimensional seismic structure of the lithosphere, *J. Geophys. Res.*, **82**, 277-296, 1977.

Arnold, E.P., Willmore, P.L., Keilis-Borok, V.I., Levshin, A.L., and I.I. Pyatetskii-Sapiro, Automatic identification of seismic wave arrivals (in Russian) *Vychisl. Seismol.*, No. 4., 170, 1968. (pp. 25 of the English translation, *Computational seismology*, V.I. Keilis-Borok (ed.), *Consultants Bureau*, New York, 1972)

Berry, M. J., and L. Knopoff, Structure of the upper mantle under the western Mediterranean Basin, *J. Geophys. Res.*, **72**, 361-3626, 1967.

Calcagnile, C., and G. F. Panza, Crust and upper mantle structure under the Baltic Shield and Barents Sea from the dispersion of Rayleigh waves, *Tectonophysics*, **47**, 59-71, 1978.

Calcagnile, C., U. Mascia, V. del Gaudio and G. F. Panza, Deep structure of southeastern Europe from Rayleigh waves, *Tectonophysics*, **110**, 189-200, 1984.

Calcagnile, G. and R. and Scarpa, Deep structure of the European-Mediterranean from seismological data, *Tectonophysics*, **118**, 93-111, 1985.

Cermak, V. and E. Hurtig, Heat flow map of Europe, enclosure for *Terrestrial heat flow in Europe*, (eds.) V. Cermak and L. Rybach, Berlin, 1979.

Clark, R. A. and G. W. Stuart, Upper Mantle structure of the British Isles, *Geophys. J. R. astr. Soc.*, **67**, 59-75, 1981.

Dercourt et al, Evolution of the Tethys belt from the Atlantic to the Pamirs since the Lias, *Tectonophysics*, **123**, 241-315, 1986.

Dost, B. The Nars array. A seismic experiment in Western Europe., *PhD thesis, University of Utrecht*, 117pp., 1987.

Dost, B., Upper mantle structure under western Europe from fundamental and higher mode surface waves using the NARS Array, *Geophys. J. Int.*, **100**, 131-152, 1990.

Dziewonski, A. M., Mapping the lower mantle: determination of lateral heterogeneity in P velocity up to degree and order 6, *J. Geophys. Res.*, **89**, 5929-5952, 1984.

Dziewonski, A. M. and D. L. Anderson, Preliminary Reference Earth Model, *Phys. Earth Planet. Inter.*, **25**, 297-356, 1981.

Dziewonski, A.M., T.A. Chou, and J.H. Woodhouse, Determination of earthquake source parameters from waveform data for studies of global and regional seismicity, *J. Geophys. Res.*, **86**, 2825-2852, 1981.

EUGENO-S working group, Crustal structure and tectonic evolution of the transition between the Baltic Shield and the North German Caledonides (the EUGENO-S Project), *Tectonophysics*, **150**, 253-348, 1988.

Europrobe working group, The tectonic evolution of Europe from the Ural mountains to the Atlantic Ocean, *A Proposal to the European Science Foundation to launch a new*

additional activity, 1991.

Furlong, K. P., Spakman, W., and M. J. R. Wortel, Thermal structure of the lithosphere: constraints from seismic tomography, *Tectonophysics* (in press), 1992.

Gobarenko, V.S., Nikolova, S.B., and T.B. Yanovskaya, 2-D and 3-D velocity patterns in southeastern Europe, Asia Minor and the eastern Mediterranean from seismological data, *Geophys. J. R. astr. Soc.*, **90**, 473-484, 1987.

Grand, S. P., Tomographic inversion for shear velocity beneath the North American Plate, *J. Geophys. Res.*, **92**, 14065-14090, 1987.

Grand, S. P., A possible station bias in travel time measurements reported to ISC, *Geophys. Res. Lett.*, **17**, 17-20, 1990

Grand, S. P., and D. V. Helmberger, Upper mantle shear structure of North America, *Geophys. J. R. astron. Soc.*, **76**, 399-438, 1984.

Guterch, A., Grad, M., Materzok, R., Pajchel, J. and E. Perchuk, Crustal structure of the southwest margin zone of the East European Platform in Poland, in: *First EGT Workshop, The Northern Segment*, D.A. Galson and St. Mueller (eds.), ESF, Strassbourg, 143-147, 1983.

Henkel, H., Lee, M.K., Lund, C-E., and T. Rasmussen, An integrated geophysical interpretation of the 200 km fennolora section on the Baltic Shield, in: *Fifth EGT Workshop, The European Geotraverse: integrative studies*, R. Freeman, P. Giese and St. Mueller (eds.), ESF, Strassbourg, 1-48, 1990.

Hovland, J. and E.S. Husebye, Three dimensional seismic velocity of the Upper Mantle beneath southeastern Europe, in: *Identification of seismic sources - Earthquake or underground explosion*, E.S. Husebye and S. Mykkeltveit (eds.), Reidel, Dordrecht, 589-605, 1981.

Hovland, J., D. Gubbins, and E.S. Husebye, Upper mantle heterogeneities beneath central Europe, *Geophys. J. R. astron. Soc.*, **66**, 261-284, 1981.

Illies, J. H., Intra-plate rifting and the Alpine system, in: *Afar depression of Ethiopia*, A. Pilger and A. Rossler (eds.), Schweitzerbart'sche Verlagsbuchhandlung, Stuttgart, 1-9, 1974.

Inoue, H., Y. Fukao, K. Tanabe, and Y. Ogata, Whole mantle P-wave travel-time tomography, *Phys. Earth Planet. Inter.*, **59**, 294-328, 1990.

Kennett, B.L.N., and G. Nolet, The interaction of the S-wavefield with the upper mantle heterogeneity, *Geophys. J. Int.*, **101**, 751-762, 1990.

Laubscher, H. P., Grundsatzliches zur tektonik des Rheingrabens, in: *Graben problems*, J. H. Illies and St. Mueller (eds.), UMP Scient. Rep. 27., Schweitzerbart, Stuttgart, 79-87, 1970.

Marillier, F. and St. Mueller, The western Mediterranean region as an upper mantle transition zone between two lithospheric plates, *Tectonophysics*, **118**, 113-130, 1985.

Monfret, T., Deschamps, A. and B. Romanowicz, The Romanian earthquake of August 30, 1986: a study based on Geoscope very long-period and broadband data, *Pageoph.*, 133, No 2, 1990.

Montagner, J.-P., Regional three-dimensional structures using long-period surface waves, *Ann. Geophys.*, **B4**, 283-294, 1986.

Morelli, C., Geophysical contribution to Knowledge of the Mediterranean Crust, in: *Geological evolution of the Mediterranean Basin*, D.J. Stanley and F-C Wesel (eds.), Springer, 65-82, 1985.

Mostaanpour, M.M., Einheitliche Auswertung Krustenseismischer Daten in Westeuropa: Darstellung von Krustparametern und laufzeitanomalien, *Berliner Geowiss. Abh.*, **B10**, Berlin, 1984.

Nataf, H. C., I. Nakanishi, and D.L. Anderson, Measurements of mantle wave velocities and inversion for lateral heterogeneities and anisotropy 3. Inversion., *J. Geophys. Res.*, **91**, 7261-7308, 1986.

Neunhofer, H., F. Marillier and G. F. Panza, Crust and upper mantle structure in the Bohemian Massif from the dispersion of Rayleigh waves, *Gerlands Beitr. Geophysik*, **90**, 514-520, 1981.

Neunhofer, H., A. Plesinger and D. Kracke, Crust and upper mantle structure between Moxa and Kasperske Hory from Rayleigh waves, *Gerlands Beitr. Geophysik*, **92**, 284-290, 1983.

Noe-Nygaard, A., The Precambrian of Denmark, in: *The Precambrian*, K. Rankama (ed.), Interscience-Wiley, New York, N.Y., 1963

Nolet, G., Solving or resolving inadequate and noisy tomographic systems, *J. Comp. Phys.*, **61**, 463-482, 1985.

Nolet, G., Seismic wave propagation and seismic tomography, in: *Seismic Tomography*, G. Nolet (ed.), Reidel Publishing Company, Dordrecht, 1-23, 1987a.

Nolet, G., Waveform tomography, in: *Seismic Tomography*, G. Nolet (ed.), Reidel Publishing Company, Dordrecht, 301-322, 1987b.

Nolet, G., Partitioned waveform inversion and two-dimensional structure under the Network of Autonomously Recording Seismographs, *J. Geophys. Res.*, **95**, 8499-8512, 1990.

Nolet, G., Imaging the upper mantle with partitioned nonlinear waveform inversion, in: *Seismic Tomography*, H.M. Iyer (ed.), Chapman and Hall Publ, (in press) 1992.

Nolet, G., J. van Trier, and R. Huisman, A formalism for nonlinear inversion of seismic surface waves, *Geophys. Res. Lett.*, **13**, 26-29, 1986a.

Nolet, G., B. Dost and H. Paulssen, The upper mantle under Europe: an interpretation of some preliminary results from the NARS project, *Geol. Mijnbouw.*, **65**, 155-166, 1986b.

Noponen, I., Surface wave velocities in Finland, *Bull. Seismol. Soc. Am.*, **56**, 1093-1104, 1966.

Paige, C. C. and M. A. Saunders, LSQR: an algorithm for sparse linear equations and sparse least squares, *ACM Trans. Math. Soft.*, **8**, 43-71 and 195-209, 1982.

Panza, G. F.,St. Mueller and G. Calcagnile, The gross features of the lithosphere-asthenosphere system from seismic surface waves and body waves, *Pageoph*, **118**, 1209-1213, 1980.

Panza, G. F., St. Mueller, G. Calcagnile and L. Knopoff, Delineation of the North Central

Italian upper mantle anomaly, *Nature*, **296**, 1982.

Papazachos, B., Phase velocities of Rayleigh waves in southeastern Europe and eastern Mediterranean Sea, *Pageoph*, **75**, no 4, 47-55, 1969.

Paulssen, H., Lateral heterogeneity of Europe's upper mantle as inferred from modelling of broad-band body waves, *Geophys. J. R. astr. Soc.*, **91**, 171-199, 1987.

Pollack, H.N., and D.S. Chapman, On the regional variations of heat flow, geotherms, and lithospheric thickness, *Tectonophysics*, **38**, 279-296, 1977.

Rial, J. A., S. Grand, and D. V. Helmberger, A note on lateral variation in upper-mantle shear velocity across the Alpine front, *Geophys. J. R. astr. Soc.*, **77**, 639-654, 1984.

Romanowicz, B., A study of the large-scale lateral variations of P velocity in the upper mantle beneath western Europe, *Geophys. J. R. astr. Soc.*, **63**, 217-232, 1980.

Snieder, R., Large scale waveform inversions of surface waves for lateral heterogeneity 2; Application to surface waves in Europe and the Mediterranean, *J. Geophys. Res.*, **93**, 12067-12080, 1988.

Sorgenfrei, T. and A. Buch, Deep tests in Denmark 1935-1959, *Danmarks Geol. Unders. (3. R. Kobenhavn)*, **36**, 160-196, 1964.

Souriau, A., Le manteau superieur sous la France, *Bull. Soc. Geol. France*, **23**, 65-81, 1981.

Souriau, A. and M. Vadell, the crust and upper mantle beneath the Pyrenees, from surface waves. Tectonic Implications., *Ann. Geophys.*, **36**, 159-166, 1980.

Spakman,W., Subduction beneath Eurasia in connection with the mesozoic Tethys. *Geol. Mijnbouw*, **65**, 145-153, 1986.

Spakman, W., Upper mantle delay time tomography with an application to the collision zone of the Eurasian, African and Arabian Plates, *PhD thesis, University of Utrecht*, 200pp., 1988.

Spakman, W., Delay-time tomography of the upper mantle below Europe, the Mediterranean, and Asia Minor, *Geophys. J. Int.*, **107**, 309-332, 1991.

Spakman, W. and G. Nolet, Imaging algorithms, accuracy and resolution in delay time tomography, in: *Mathematical Geophysics: a survey of recent developments in seismology and geodynamics*, Vlaar et al. (eds.), Reidel Publishing Company , Dordrecht, 155-188, 1988.

Stuart, G. W., The upper mantle structure of the North Sea region from Rayleigh wave dispersion, *Geophys. J. R. astr. Soc.*, **52**, 367-382, 1978.

Suhadolc, P., and G. F. Panza, Physical properties of the lithosphere-asthenosphere system in Europe from geophysical data, in: *The lithosphere in Italy advances in Earth science research*, Boriani et al. (eds.), Accademia Nazionale dei Lincei, Roma, 15-40, 1989.

Sumino, Y. and O.L. Anderson, 1984, Elastic constants of minerals, in: *CRC Handbook of Physical Properties of Rocks*, **3**, R.S. Carmichael (ed.), 39-138.

Takeuchi, H., and M. Saito, Seismic surface waves, *Methods Comp. Phys.*, **11**, 217-295, 1972.

Taymaz, T. J. Jackson, and R. Westaway, Earthquake mechanisms in the Hellenic Trench near Crete, *Geophys. J. Int.* , **102**, 695-731, 1990.

Torsvik, T.H., Olesen, O., Ryan, P.D., and A. Trench, On the palaeogeography of Baltica during the Palaeozoic: palaeomagnetic data from the Scandinavian Caledonides, *Geophys. J. Int.*, **103**, 261-279, 1990.

Van der Hilst, R. D., Tomography with *P*, *PP* and *pP* delay-time data, and the three-dimensional mantle structure below the Caribbean region, *PhD thesis, University of Utrecht*, 250pp., 1990.

Van der Hilst, R. D., and W. Spakman, Importance of the reference model in linearized tomography and images of subduction below the Caribbean plate, *Geophys. Res. Lett.*, **16**, 1093-1096, 1989.

Van der Hilst, R. D., E. R. Engdahl, W. Spakman, and G. Nolet, Tomographic imaging of subducted lithosphere below northwest Pacific island arcs, *Nature*, **353**, 37-43, 1991.

Van der Hilst, R. D., E. R. Engdahl, and W. Spakman, Tomographic inversion of P and pP data for aspherical mantle structure below the northwest Pacific region, *Geophys. J. Int.* (submitted), 1992.

Wiggins, R. A., The general linear inverse problem: Implication of surface waves and the free oscillations for Earth structure. *Rev. Geophys. Space Phys.*, **10**, 251-285, 1972.

Woodhouse, J.H. and Dziewonski, A.M., Mapping the upper mantle: Three dimensional modeling of the Earth structure by inversion of seismic waveforms, *J. Geophys. Res.*, **89**,5953-5986, 1984.

Yan, B., E. K. Graham, and K. P. Furlong, 1989, Lateral variations in upper mantle thermal structure inferred from three-dimensional seismic inversion models, *Geophys. Res. Lett.*, **16**, 449-452.

Yanovskaya, T. B., G. F. Panza, P. D. Ditmar, P. Suhadolc and S. Mueller, Structural heterogeneity and anisotropy based on 2-D phase velocity patterns of Rayleigh waves in Western Europe, *Rend. Fis. Acc. Lincei*, 9, **1**, 127-135, 1990.

Zhang, Y.-S, and T. Tanimoto, Ridges, hotspots and their interpretation as observed in seismic velocity maps, *Nature*, **355**, 45-49, 1992.

Ziegler, A., Evolution of the Arctic-North Atlantic and the Western Tethys, *Am. As. Petrol. Geol. Memoir*, **43**, 1988

Zielhuis, A., A shear velocity model for Europe from ISC delay times, Proceedings of the 4th workshop on the European Geotraverse project, European Science Foundation, Strassbourg, 57-62, 1988.

Zielhuis, A., Spakman, W. and G. Nolet, A reference model for tomographic imaging of the shear velocity structure beneath Europe, in: *Digital seismology and fine modelling of the lithosphere*, Cassinis, R. Panza, G. and G. Nolet (eds.), Plenum Press, London, 333-340, 1989.

Samenvatting (Summary in dutch)

De onderzoeken van Spakman (1988) en Spakman, Van der Lee en Van der Hilst (in voorbereiding) hebben gedetailleerde, drie-dimensionale (3D), beelden van variaties in de voortplantingssnelheid van longitudinale golven (P-golven) in de de aarde onder Europa opgeleverd. Deze beelden weerspiegelen structuren in de aarde, maar geven beperkte informatie over de oorzaak van de variaties in de P-golf snelheid. De variaties in voortplantingssnelheid kunnen het gevolg zijn van verschillen in temperatuur, verschillen in samenstelling van het gesteente, of beide. Deze oorzaken beinvloeden de voortplantingssnelheid van longitudinale golven anders dan die van transversale (S-) golven. Door zowel de variaties in de P-golf snelheid en de variaties in de voortplantingssnelheid van S-golven te onderzoeken kan onderscheid gemaakt worden tussen de oorzaken. Daarom was de doelstelling van dit onderzoek een 3D beeld af te leiden van de variaties in de S-golf snelheid onder Europa.

Eerst pasten we de methode toe die door bovengenoemde auteurs werd gebruikt: de methode van reistijd-tomografie (hoofdstuk 2-3). Deze methode maakt gebruik van het verschil van de aankomsttijd van een seismische golf en de tijd voorspeld met behulp van een referentie snelheidsmodel. We pasten deze methode toe op reistijden van S-golven, gerapporteerd door het *International Seismological Centre* (ISC). Een geschikt een-dimensionaal (1D) referentie model voor de inversie van de reistijden werd bepaald uit de gemiddelde variatie in de reistijden als functie van epicentrale afstand voor Europa. De fouten in de reistijdgegevens zijn groot: de standaard deviatie van fouten als gevolg van onnauwkeurige bepaling van de aankomsttijd, verkeerde identificaties en tot op zekere hoogte onnauwkeurigheden in de locaties van de hypocentra, is ongeveer 5 seconden voor epicentrale afstanden kleiner dan 28° en ongeveer 3 seconden voor grotere epicentrale afstanden. Vergelijking van de reistijdgegevens voor gebieden met een verschillende tektonische geschiedenis in Europa toont echter aan dat deze gegevens wel degelijk informatie over de structuur bevatten. Het 3D snelheidsmodel werd bepaald door inversie van reistijden met een maximum absolute afwijking tov de looptijd voorspeld door het 1D startmodel van 6 seconden. We kozen dit strenge selectie criterium omdat 3D modellen, verkregen door inversie van reistijden met een grotere afwijking in bepaalde diepte intervallen voornamelijk positieve of voornamelijk negatieve anomalien vertoonden. Het zou nader onderzocht moeten worden of dit betekent dat een gelinearizeerde inversie van die looptijd gegevens met het gebruikte startmodel niet nauwkeurig genoeg is.

Vanwege het risico dat grote fouten in de reistijdgegevens een belangrijke invloed op het eindresultaat hebben, en vanwege mogelijke onnauwkeurigheden door linearizatie rond een 1D startmodel, zochten we naar een onafhankelijke bevestiging van het resultaat. Daarom pasten we vervolgens de methode van "gesplitste golfvorm aanpassing" (Nolet, 1990) toe om een 3D model van de S-golf snelheid af te leiden. In tegenstelling tot de methode van reistijd-tomografie, wordt bij deze methode gebruikt van de informatie van de gehele

golfvorm van ruimtegolven en oppervlakte golven. Deze methode heeft voordelen boven de methode van reistijd-tomografie. Met laatstgenoemde methode kunnen gedetailleerde beelden gemaakt worden van structuren onder gebieden met een hoge seismiciteit en een hoge dichtheid van seismische stations, maar de methode werkt minder goed voor structuren onder gebieden met weinig stations en/of aardbevingen. Doordat bij de methode van "gesplitste golfvorm aanpassing" informatie van ruimtegolven en oppervlakte golven gecombineerd wordt, kunnen structuren in dergelijke gebieden beter onderzocht worden. De essentiele aanname bij deze methode is dat golfvormen alleen beinvloed worden door de structuur van de aarde op het verticale vlak door de grootcirkel tussen bron en ontvanger. Effecten van golfvoortplanting buiten dit vlak worden dus verwaarloosd. Onder deze aanname worden golfvormen in twee stappen geinverteerd. In de eerste stap wordt het gedeelte van het seismogram vanaf de S-golf tot en met de grondtoon van de Rayleigh golf geinverteerd voor een gemiddeld, 1D, snelheidsmodel voor het pad tussen bron en ontvanger. Dit is een niet-lineaire inversie, maar het resultaat is een aantal lineaire vergelijkingen voor het gemiddelde snelheidsmodel voor het pad tussen bron en ontvanger. In de tweede stap worden de lineaire vergelijkingen, die zijn verkregen door inversie van seismogrammen van vele kruisende golfpaden, geinverteerd voor een 2D of 3D snelheidsmodel. Nolet (1990) paste de methode toe om een 2D model van de S-golf snelheid onder het NARS netwerk af te leiden. In dit proefschrift wordt de methode voor het eerst toegepast om een 3D snelheidsmodel af te leiden. Belangrijke aspecten met betrekking tot de methode zijn de resolutie die behaald kan worden met deze methode en voor welke frequenties golfvormen voorspeld kunnen worden door het 3D model. We gebruikten digitale seismogrammen van het NARS netwerk, het GDSN-, UKNET-, and IRIS netwerk. In het algemeen konden we de S-(ruimte)golven inverteren voor frequenties tot 60 mHz. Voor inversie werden frequenties boven 25 mHz uit de grondtoon van de Rayleigh golf gefilterd omdat de kans groot is dat voor die frequenties effecten van verstrooiing van seismische golven niet meer te verwaarlozen zijn. In totaal inverteerden we 217 seismogrammen. De resulterende 917 vergelijkingen voor de S-golf snelheid werden geinverteerd voor een 3D snelheidsmodel. In het algemeen is er een goede overeenkomst tussen de golfvormen zoals voorspeld door het 3D S-snelheidsmodel en de waargenomen golfvormen.

Het meest spectaculaire resultaat is nieuwe informatie over de structuur van de aarde onder de Tornquist-Teisseyre Zone (TTZ). De TTZ wordt algemeen beschouwd als een scheidingslijn tussen de precambrische korst - dit is de buitenste 30-50km van de aarde - en de jongere korst van west en centraal Europa, maar de tektonische geschiedenis van deze zone is onzeker. Veel onderzoek is verricht naar de structuur van de korst, maar tot nu toe was er niets bekend over de diepere structuur. Onze resultaten geven aan dat er onder de TTZ een scherpe overgang van lage S-golf snelheid onder centraal en west Europa en hoge S-snelheid onder het Baltische Schild en het Russische Platform is. Deze grens is detecteerbaar tot tenminste 140km diepte. In het model is het snelheidscontrast over de TTZ het grootst tussen het Pannonisch Bassin en het Russisch Platform, waar het ongeveer 12% en 9% is op respectievelijk 80 en 140 km diepte. Het snelheidscontrast over de TTZ is het laagst

tussen zuid-Zweden en Denemarken en noord Duitsland, waar het ongeveer 5% en 4.5% bedraagt op respectievelijk 80 en 140 km diepte. Uitgaand van de referentie waarden, zoals gebruikt door Yan et al. (1989), voor snelheid en temperatuur op 150 diepte (respectievelijk 4.506 km/s en 1300 °C) kan de hoge snelheid onder het Baltisch Schild en Russisch Platform geinterpreteerd worden in termen van een temperatuur anomalie van een paar honderd graden. Dit is in overeenstemming met de temperatuur die verwacht kan worden op 150 km diepte voor een regio met een oppervlakte warmtestroom van 40 mW/m^2, wat een respresentatieve waarde is voor het Russisch Platform. Een verschil in compositie of een combinatie van beide factoren als oorzaak van het snelheidscontrast kan echter niet worden uitgesloten. Waarschijnlijk wordt de lage snelheid onder de Karpaten en de noordelijke Aegeische Zee en west-Turkije veroorzaakt door partiele smelt. Vergelijking met het model van de P-golf snelheid van Spakman, Van der Lee en Van der Hilst (in voorbereiding) in het gebied waar de resolutie het hoogst is, in zuid-oost Europa, toont aan dat de variaties in de S-golf snelheid overeenkomen met de variaties in de P-golf snelheid qua teken van de snelheidsanomalien, maar de amplitudes van de S-golf variaties zijn in het algemeen groter.

De resultaten geven aan dat met de methode van "gesplitste golfvorm aanpassing" grote snelheidscontrasten goed kunnen worden bepaald in intraplaat gebieden. Het feit dat zelfs de Helleense subductie zone, die duidelijk te zien is in de beelden van de P-golf snelheid van Spakman (1988) en Spakman, Van der Lee en Van der Hilst (in voorbereiding), gedetecteerd is in het gebied met de hoogste resolutie toont aan dat met deze methode een gedetailleerde beelden gemaakt kunnen worden, mits er voldoende seismogrammen beschikbaar zijn. Voor toekomstige toepassingen van de methode moet onderzocht worden of het effect van varierende korstdikte op de verkregen snelheidsvariaties in de inversie moet worden meegenomen.

Acknowledgements

Dit proefschrift is tot stand gekomen door samenwerking met een aantal mensen, die ik hier speciaal voor wil bedanken.

Als eerste mijn promotor Prof. Guust Nolet die mij de afgelopen jaren met veel enthousiasme begeleid heeft. De vele gesprekken met hem waren leerzaam en motiverend. Ik heb veel bewondering voor de manier waarop hij de afdeling seismologie geleid heeft, belangstelling had voor ieder's onderzoek en met zijn studenten en medewerkers veel wist te bereiken, maar aan een ieder de vrijheid en eigen stijl liet. Ik ben blij dat ik de afgelopen vier jaar met hem heb kunnen samenwerken. Ik ben hem ook dankbaar voor het lezen van de eerste versie van dit proefschrift en alle zeer nuttige kritiek en suggesties.

Wim Spakman dank ik voor de vele discussies en hulp, tijdens de eerste twee jaar van mijn onderzoek, en voor het beschikbaar stellen van programma's waarmee het resultaat van hoofdstuk 3 verkregen is. Hij maakte altijd tijd vrij om mij te helpen, ook als hij het zelf erg druk had. Bijna alle figuren in dit proefschrift zijn gemaakt met behulp van Wim's geweldige plotprogramma "P". Roel Snieder heeft mij begeleid tijdens Guust's afwezigheid in het eerste jaar van mijn onderzoek. De gesprekken met hem gedurende mijn promotieonderzoek brachten mij nieuwe gezichtspunten bij. De samenwerking met Hanneke Paulssen was altijd plezierig. Ik heb vaak geprofiteerd van haar grote kennis en ervaring op het gebied van de observationele seismologie.

Bernard Dost en Reinoud Sleeman waren zeer behulpzaam bij het verzamelen en verwerken van de vele seismogrammen die ik gedurende de laatste twee jaar voor mijn onderzoek gebruikt heb. I benefitted from the proximity of the Orfeus Data Centre, from which I collected the digital seismograms. I thank Jim Taggert for making hard copies of the analog WWSSN seismograms used in this research available to me.

Dee Pattynama heeft mij geweldig geholpen tijdens mijn verblijf in Engeland, doordat zij in Utrecht de nodige zaken regelde voor mijn promotie en belangrijke formulieren naar mij doorstuurde. Joop Hoofd dank ik voor zijn hulp bij allerlei problemen met het gebruik van de computer. Maarten Remkes, Rob Govers, Filip Neele, Marc de Jonge, en Paul Meijer waren altijd bereid te helpen met problemen met mijn onderzoek, het maken van kleuren plaatjes op de "SUN", of problemen met tekstverwerkingsprogramma's. Prof. Rinus Wortel, Roel Snieder en Filip Neele dank ik voor het kritisch lezen van mijn proefschrift en suggesties ter verbetering. Alle collega's van de afdeling geofysica dank ik voor de leuke tijd in Utrecht.

During the last year of my PhD research I tried to be with Rob van der Hilst in Leeds as much as possible. I am very grateful that Prof. David Gubbins of the department of Earth Sciences of the University of Leeds allowed me to work at his department so that I was able to prepare my thesis in Leeds. I thank Roger Clark for his advice and his software to process digitized WWSSN seismograms. Derek Fairhead allowed me to use the facilities to digitize analog seismograms. I am grateful to Steve Neil who was very patient in explaining and helping with the digitizing software.

Rob van der Hilst heeft mij op verschillende manieren bij mijn mijn onderzoek geholpen. We hebben veel gediscussieerd, hij heeft vaak advies gegeven en programma's beschikbaar gesteld waarmee het resultaat van hoofdstuk 3 verkregen is. Zijn hulp tijdens de eindfase van dit onderzoek, zoals het kritisch lezen van mijn proefschrift en het camera-ready maken, was fantastisch.

This research was funded by the Dutch Organisation for the Advancement of Pure Research (NWO).

Curriculum Vitae

27-07-60	Born in Heerde, The Netherlands.
1972-1978	Gymnasium β, Christelijk Lyceum-Havo in Gouda, The Netherlands.
24-01-1983	Kandidaatsexamen G4 (BSc. Geology with physics and mathematics).
26-10-1987	Doctoraal examen (MSc.) Geophysics.
1988-1991	Research assistant at the Department of Theoretical Geophysics, University of Utrecht, The Netherlands.